

Novel Transport Properties in Spatially Confined $\text{La}_{0.3}\text{Pr}_{0.4}\text{Ca}_{0.3}\text{MnO}_3$ Thin Films

by

Jaechun Jeon

A thesis submitted in partial fulfillment of the requirements for the degree of

Doctor of Philosophy

Department of Physics

University of Alberta

© Jaechun Jeon, 2016

Abstract

Novel magneto-transport properties in spatially confined $\text{La}_{0.3}\text{Pr}_{0.4}\text{Ca}_{0.3}\text{MnO}_3$ (LPCMO) thin films have been intensively studied in this thesis. Due to the existence of micrometer-scale electronic phase separation in the LPCMO system, it exhibits extraordinary electronic transport behaviour when the lateral dimension of the system is reduced to the size of inherent phase domains.

First, we studied the spatial confinement effect on the magnetoresistance in microbridges fabricated from LPCMO thin films. The spatially confined LPCMO micro-bridge was found to produce two maxima in the temperature dependence of the magneto-resistance (MR) as well as in the temperature dependence of the area of the hysteresis loops that exist in an isothermal magnetic field scan of the resistance. One of the peaks is close to the metal-to-insulator transition temperature, as expected for a standard manganite film, while the additional peak occurs at lower temperatures where co-existing metallic and insulating domains have sizes comparable to the spatially confined region. The dependence of the MR of these two peaks on magnetic field is also substantially different, i.e., the MR of the latter peak is considerably less sensitive to magnetic field than the former one.

Next, time-dependent measurements of the resistance were carried out on thin films of LPCMO which contain microbridges with lateral dimensions $2\ \mu\text{m} \times 2\ \mu\text{m}$ and $25\ \mu\text{m} \times 25\ \mu\text{m}$. The $2\ \mu\text{m} \times 2\ \mu\text{m}$ microbridge is spatially confined such that at certain temperatures, its lateral dimension is comparable to the sizes of the metallic and insulating domains within the sample. At a fixed temperature, as time increases, sharp jumps in the resistance are observed superimposed upon a long-time evolution of the resistance. The magnitude and sign of these jumps can be controlled by the strength of the magnetic field. By contrast, such resistance jumps are virtually non-existent in the $25\ \mu\text{m} \times 25\ \mu\text{m}$ microbridge. The results are described within a model of percolation or de-percolation of metallic domains within the confined region of the thin film.

We also report the creation of colossal in-plane anisotropic magnetoresistance (C-AMR) of $> 16,000\ \%$ via the engineering of spatial confinement in LPCMO films. Recalling

that typical AMR values in films are only a few percent, these results mark an astonishing increase which could shed new light on the nature of the AMR in electronically phase separated confined systems and might potentially lead to fabrication of novel manganite-based switching and sensor devices. The unique colossal behaviour is attributed to the anisotropic percolation of elongated metallic domains whose orientation depends on the direction of the magnetic field as well as the geometry of the micro-system.

The effect of the bias current on the in-plane C-AMR was then investigated in spatially confined LPCMO microbridges. Dramatic increases of the C-AMR are found when the bias current is reduced. For example, in one of the samples, the C-AMR changed from $\sim 900\%$ to over $\sim 24,000\%$ as the current is decreased from $1\ \mu\text{A}$ to $10\ \text{nA}$. The results indicate that the bias current can be a useful method to artificially manipulate the C-AMR, via changes in the percolation, in spatially confined manganite thin films.

Finally, electron beam induced tunneling magnetoresistance (TMR) behaviour in spatially confined manganite thin films is investigated. Tunneling magnetoresistance (TMR) of $\sim 300\%$ has been produced in spatially confined LPCMO films on LaAlO_3 substrates by using electron beam scanning. This new e-beam scanning method to artificially engineer local phase domains can be a powerful tool for fabricating novel manganite-based sensor devices.

We believe that the experimental results presented in this thesis will improve the scientific understanding of the electrical properties of these unique systems, i.e. spatially confined electronic phase separated systems, and can also provide important clues on engineering next generation EPS-based applications such as low field magnetoresistance sensor (LF-MR sensors), C-AMR hard disk read head, and magnetoresistive random access memory (M-RAM) devices.

Preface

The research presented in this dissertation was carried out in the Department of Physics at the University of Alberta under the supervision of Professor Kim H. Chow, from September 2012 to August 2016. Unless otherwise stated, the original work presented in this thesis is based on my own work.

Chapter 4 of this thesis has been published as **J. Jeon**, H. S. Alagoz, R. Boos, J. Jung and K. H. Chow, “*Reentrant low-field magneto-resistance in $La_{0.3}Pr_{0.4}Ca_{0.3}MnO_3$ film due to spatial confinement,*” Appl. Phys. Lett. **104**, 122405 (2014).

Chapter 5 of this thesis has been published as **J. Jeon**, H. S. Alagoz, J. Jung and K. H. Chow, “*Field Dependence of the Resistance Steps in Spatially Confined $La_{0.3}Pr_{0.4}Ca_{0.3}MnO_3$ Thin Films,*” J. Phys. Soc. Jpn. **85**, 044706 (2016).

Chapter 6 of this thesis has been published as **J. Jeon**, H. S. Alagoz, J. Jung and K. H. Chow, “*Low field colossal anisotropic magnetoresistance in spatially confined electronically phase separated $La_{0.3}Pr_{0.4}Ca_{0.3}MnO_3$ microbridges,*” Appl. Phys. Lett. **107**, 052402 (2015).

Acknowledgements

First of all, I would like to thank Dr. Kim H. Chow and Dr. Jan Jung for all valuable discussions, advice and supervision (an expression 'thank you' is not enough to express my gratitude to their supervision). They gave me a wonderful opportunity to work in a great group. Without them, I could not achieve the goals that I have done so far in this group. It was always my favourite to discuss with them about the projects and works.

I also would like to thank Dr. Alagoz (Serhat), Don Mullin, Greg Popwich, Paul Zimmerman, Antonio Vinagreiro, Dr. Anqiang, and Dr. Shihong for inspiring discussions and technical help.

Special thanks to my wife, Seonmi Song.

Abbreviations

1. EPS: **E**lectronic **P**hase **S**eparation
2. CMR: **C**olossal **M**agneto-**R**esistance
3. LF-CMR: **L**ow **F**ield **C**olossal **M**agneto-**R**esistance
4. AMR: **A**nisotropic **M**agneto-**R**esistance
5. FMM: **F**erromagnetic **M**etallic
6. COI: **C**harge-**O**rded **I**nsulating
7. AFI: **A**nti-ferro **M**agnetic **I**nsulating
8. PMI: **P**aramagnetic **I**nsulating
9. MIT: **M**etal-to-**I**nsulator phase **T**ransition
10. DE: **D**ouble **E**xchange
11. SE: **S**uper **E**xchange
12. C-AMR: **C**olossal **A**nisotropic **M**agneto-**R**esistance
13. TMR: **T**unneling **M**agneto-**R**esistance
14. MTJ: **M**agnetic **T**unnel **J**unction

Contents

1	Introduction	1
1.1	Motivation	1
1.2	Thesis Organization	5
1.3	List of Publications	6
2	Basic Features of Manganites	7
2.1	Structure of manganese oxides	9
2.2	Crystal field effect and Jahn-Teller effect	11
2.2.1	Perturbation due to the crystal: crystal field effect	11
2.2.2	Jahn-Teller effect	13
2.3	Double exchange model	16
2.4	Phase separation and percolation model	17
2.5	Spatial confinement phenomenon in manganite system	20
3	Experimental Techniques	25
3.1	Polycrystalline LPCMO bulk sputtering target	25
3.2	Thin film growth	26
3.3	Device fabrication: photo-lithography and chemical wet-etching	28
3.4	Transport measurements	29
4	Re-entrant Low-field Magneto-resistance in LPCMO Film due to Spatial Confinement	33
4.1	Introduction	33
4.2	Experimental details	34
4.3	Results and discussion	34
4.4	Conclusions	41
5	Field Dependent Resistive Evolution in Spatially Confined LPCMO Thin Films	43
5.1	Introduction	43
5.2	Experimental details	44
5.3	Results and discussion	44

5.4	Conclusions	53
6	Low Field Colossal Anisotropic Magnetoresistance in Spatially Confined Electronically Phase Separated LPCMO Microbridges	54
6.1	Introduction	54
6.2	Experimental details	55
6.3	Results and discussion	56
6.4	Conclusion	62
7	Current Dependence of Colossal Anisotropic Magnetoresistance in LPCMO Microbridges	64
7.1	Introduction	64
7.2	Results and discussion	65
7.3	Conclusion	70
8	Electron Beam Induced TMR-like Behaviour in Spatially Confined LPCMO-LAO Thin Films	71
8.1	Introduction	71
8.2	Experimental details	73
8.3	Results and discussion	74
8.4	Conclusion	81
9	Summary, Conclusions and Directions for Future Works	83
9.1	Re-entrant low-field magneto-resistance in LPCMO film due to spatial confinement	83
9.2	Field dependent resistive evolution in spatially confined LPCMO thin films	83
9.3	Low field colossal anisotropic magnetoresistance in spatially confined electronically phase separated LPCMO microbridges	84
9.4	Current dependence of colossal anisotropic magnetoresistance in LPCMO microbridges	85
9.5	Electron beam induced TMR-like behaviour in spatially confined LPCMO-LAO thin films	85
9.6	Directions for future works	86
9.6.1	Reproducibility of spatial confinement induced transport properties	86
9.6.2	Geometrical engineering of spatial confinement for AMR manipulation (anisotropic strain induced effects)	88
9.6.3	Further understanding of electron beam scanning effect on electronic phase separated manganites	89

List of Figures

2.1	Examples of the CMR and the AMR in a wide manganite ($\text{La}_{0.3}\text{Pr}_{0.4}\text{Ca}_{0.3}\text{MnO}_3$) thin film: (a) Resistance vs. Temperature, $R(T)$ at $H = 0$ T (zero field) and at $H = 1$ T. (b) $R(T)$ at field (1 T) orientation parallel (at 0 degree) and perpendicular (90 degree) to the current direction, respectively.	8
2.2	Cubic-perovskite structure of manganites. A-site contains large ions of rare earth trivalent lanthanide cation (e.g. La^{3+} , Sm^{3+}) or alkaline earth divalent (e.g. Ca^{2+} , Sr^{2+} , Ba^{2+}) elements. B-site contains Mn^{3+} or Mn^{4+} ions (relative smaller). The oxygen atoms surround the B-sites(Mn) with octahedral configuration.	9
2.3	Structures of distorted perovskites of manganite due to the connection pattern of MnO_6 octahedra in the lattice structure: (a) orthorhombic and (b) rhombohedral. The figure is produced from Ref. [20].	10
2.4	(a) The shapes of the five different orbitals of d-shell. (b) Crystal field effect between $3d_{xy}$ and $2p_{x,y}$. (c) Crystal field effect between $3d_{x^2-y^2}$ and $2p_{x,y}$	12
2.5	A schematic diagram of the Crystal-field splitting and Jahn-Teller effect: In the crystal field effect, the five degenerate orbitals split into the t_{2g} triplet levels and an e_g doublet. Due to the orbital-lattice interaction in $\text{Mn}^{3+}(d^4)$ parent manganese oxide, further splitting of the degeneracy occurs called the Jahn-Teller effect.	13
2.6	The energy of an octahedral structure as a function of distortion, Q according to eqn (2-3) and (2-4), respectively.	15
2.7	Four different types of antiferromagnetic order: (a) A-type, (b) C-type, (c) E-type, and (d) G-type, respectively.	16
2.8	(a) A schematic diagram of double exchange interaction. (b) Antiferromagnetic order of undoped manganite. (c) Ferromagnetic order of divalent doped manganite at low temperature. (d) The spin orientations near the metal-to-insulator phase transition temperature where the spins orient in random direction due to thermal-dynamic vibrations. (e) The effect of external magnetic field near the metal-to-insulator phase transition temperature. [29]	18

2.9	(Left) Random occupation of spaces with $p = 0.2$ where white, grey and black are unoccupied state, occupied state and cluster of the occupied states, respectively. (Right) Random occupation of spaces with $p = 0.5$ where the system percolates.	20
2.10	A schematic illustration of spatial confinement in manganite: in manganite system, ferromagnetic metallic (FMM) phase domains (dark blue) grow within the background of charge ordered insulating (COI) phase domains (check pattern background) and one can imagine the current easily flows through FMM domains. However, when the system's width is reduced to the size of the phase domains (red rectangle, spatial confinement), the conduction path can be annihilated or created by the percolation of FMM domains within the spatially confined region (the arrows indicate disconnection of FMM domains; when the FMM domains join a sharp resistance jump is expected). Figure is reproduced from Ref. [12].	21
2.11	(a) Resistivity vs. temperature profiles for $(\text{La}_{(5/8-0.3)}\text{Pr}_{0.3})\text{Ca}_{3/8}\text{MnO}_3$ wires on LAO substrate under a 3.75 T external magnetic field. Sharp jumps of resistivity can be seen near the metal-to-insulator phase transition temperature for both cooling and warming process. [12] (b) Resistance vs. magnetic field curves and magnetization vs. magnetic field (with different field steps: 2000 Oe/step and 500 Oe/step, respectively) for $\text{Pr}_{0.65}(\text{Ca}_{0.75}\text{Sr}_{0.25})_{0.35}\text{MnO}_3$ structure at 75 K. [13]	22
2.12	The temperature-dependent MFM image (a)for cooling process (scanned area: 6 by 6 micrometer) and (c)for warming process (scanned area: 7.5 by 7.5 micrometer). The corresponding resistance vs. temperature is shown for cooling (blue) and warming (red) processes, respectively. [10]	23
3.1	(a) A picture of the inside of the sputtering chamber: For LPCMO thin film deposition, a 1 inch magnetron sputtering gun is used where the shutter is installed to control (on/off) the sputtering. (b) A picture of the sputtering system: the system consists of a vacuum chamber, vacuum pump unit, water supply, and control station. (c) An illustration of off axis D. C. magnetron sputtering process: As Ar ions accelerate toward the sputtering target, the collisions of these Ar ions onto the target eject target atoms (LPCMO). Then the ejected atoms sit layer by layer on the heated substrate.	27
3.2	Procedure of photo-lithography and chemical wet-etching: (a) Sample preparation and surface cleaning. (b) Photoresist (HPR 504) spreading. (c) Mask aligning and UV exposure. (d) Development of the pattern (DEV 354). (e) Chemical wet-etching process. (f) Cleaning the photoresist.	28

3.3	A picture of anisotropic magneto-resistance (AMR) system that is consisted of vacuum unit, cryogenics, measurement unit and magnet unit, respectively. The inset of the picture shows inside of the AMR system where the samples are placed.	30
3.4	A schematic and block diagram of transport measurement system.	31
3.5	The 4 point probe method for (a) AC/DC current source and nanovoltmeter combination and (b) sourcemeter unit.	32
4.1	Temperature and field dependence of the resistance in the (a) 2 micrometer and the (b) 25 micrometer width micro-bridges during warming. The shaded regions are shown expanded in Fig. 4-2. The insets show pictures of the 2 by 2 and 25 by 25 micro-bridges with the directions of the current (I) and magnetic field (H) indicated.)	35
4.2	Temperature and field dependence of the resistance in the (a) 2 micrometer and the (b) 25 micrometer micro-bridges during warming process. These plots are an expansion of Fig. 4-1 (the shaded regions) from 100 K to 130 K.	36
4.3	Temperature and field dependence of the magnetoresistance in the (a) 2 micrometer and the (b) 25 micrometer micro-bridges during warming. The shaded regions are the temperature range where a secondary peak appears for a spatially confined manganite system. The insets show the dependence of the MR at 117 K and near metal-insulator transition temperature.	38
4.4	The plots (a) to (f) show the normalized resistance versus the magnetic field of 2 micrometer width bridge. The arrows indicate the direction of the field sweep, the field is first increased to 1.08 T and then subsequently decreased to 0 T.	39
4.5	The plot shows the area of the R(H) loop versus temperature in the 2 micrometer and (inset) 25 micrometer micro-bridges.	41
5.1	(a) Resistance vs. temperature in various external magnetic fields. Note the abrupt changes of the resistance in the temperature range marked in yellow: as discussed in the text, these are signatures of spatial confinement. (Bottom-right inset) The magnification of the main figure showing the abrupt resistance changes in the confinement region. (b) Plot of $\ln(R)$ vs. $1/T$ for the 2 micrometer width microbridge. The slight change in slope may indicate the existence of T_{CO}	45
5.2	Representative time relaxation of the resistance in a 2 micrometer wide LPCMO film at three fields 0 T, 0.4 T and 1.1 T. At each field, the data for three temperatures, i.e., 115 K, 118 K, and 120 K, are shown.	48

5.3	(a) The temperature dependence of the normalized maximum resistance jump $\Delta R_{max}(\%)$ in various external magnetic fields for the 2 micrometer wide LPCMO microbridge and (b) for the 25 micrometer wide LPCMO sample.	49
5.4	(Color online) The magnetic field dependence of the normalized maximum resistance jump $\Delta R_{max}(\%)$ for the 2 micrometer and 25 micrometer wide LPCMO microbridges. As noted in the text, the positive values of $\Delta R_{max}(\%)$ indicate “up” jumps while negative values indicate “down” jumps.	50
5.5	(Color online) Illustration of phase domain volume change with time at different constant magnetic fields in the spatially confined microbridge. The red dotted circles indicate the site(s) of interest for explaining the existence of sharp resistance jumps. Note that the phase domains are illustrated based on the experimental observations of FMM domains in Ref. [10].	51
6.1	(a) Schematic diagram of the microbridge and its optical microscope images. (b) Temperature dependence of the resistance measured separately for the wide part of the sample and the zig-zag microbridge. The resistance was measured in 0.2 T for both 0 degree and 90 degree orientations of the magnetic field.	57
6.2	Temperature dependence of the in-plane AMR at $H = 0.2$ T, applied at 0 degree and 90 degree, for the zig-zag microbridge. Note that very high values of about 16,000 % are reached. The AMR measured for the wide part of the film is very small (~ 20 %) compared to that of the microbridge.	58
6.3	Temperature dependence of the resistance measured for various orientations (angle) of the magnetic field for (a) the zig-zag microbridge, (b) a 2 by 10 microbridge, and (c) a 2 by 2 microbridge. The insets show the temperature at which the maximum resistance jumps occur, T_J , plotted as a function of the angle. Note that the resistance jumps occur at two different temperature regions for the zig-zag microbridge but is less clear in the straight-line microbridges.	59
6.4	(a) Dependence of resistance on temperature and magnetic field for the zig-zag microbridge for angle of 0 degree and 90 degree. The vertical arrowheads mark temperatures at which the largest resistance jumps occur. ΔT denotes the temperature difference between the largest resistance jumps measured at angle of 0 degree and 90 degree. (b) The magnetic field dependence of the maximum AMR. At each field, this quantity is obtained from the temperature dependence of the AMR using data that are analogous to that shown in Fig. 6-2. (c) Dependence of ΔT and T_J on magnetic field for the zig-zag microbridge. As indicated previously, T_J is the temperature at which the maximum resistance jumps occur while the ΔT is the temperature difference between T_J (at 90 degree) and T_J (at 0 degree).	60

7.1	Temperature dependence of resistance at different applied d.c. currents upon application of the external magnetic field of (a) 0.2 T at 0 degree, (b) 0.2 T at 90 degree, (c) 1.1 T at 0 degree, and (d) 1.1 T at 90 degree in the microbridge of 56 micrometer length (2 micrometer width).	66
7.2	Temperature- and applied d.c. current-dependence of the in-plane C-AMR at (a) $H = 0.2$ T and (b) $H = 1.1$ T, respectively, in the microbridge of 56 micrometer length (2 micrometer width).	67
7.3	Applied d.c. current dependence of the maximum AMR magnitude at 0.2 T and 1.1 T, respectively.	68
7.4	Applied d.c. current dependence of the maximum AMR magnitude at 0.2 T for different bridge lengths.	69
8.1	(a) A schematic diagram of a typical TMR device. (b) The resistance change vs. magnetic field in the $\text{CoFe}/\text{Al}_2\text{O}_3/\text{Co}$ junction at room temperature. The arrows in the figure indicate the relative magnetization orientation of the CoFe and Co layers. [92]	72
8.2	(a) SEM image of the sample before scanning the electron beam. (b) SEM image of the sample after e-beam scanning; dark colored line (in the red rectangle) is induced by carbon deposit during the e-beam scanning. Note that white dots in SEM images are due to charging effect in the insulating substrate. (c) AFM image of the sample after e-beam scanning.	75
8.3	(a) A schematic illustration of e-beam scanning across the microbridge sample. (b) The temperature dependence of the resistance in a spatially confined LPCMO/LAO sample in the as-grown state, post-annealed state, and e-beam scanned state.	76
8.4	(a) The bias voltage dependence of the resistance vs. external magnetic field at 108 K in 600 e-beam scanned LPCMO/LAO microbridge. The arrows indicate the relative magnetization orientation in adjacent metallic domains. (b) Maximum MR magnitude vs. bias voltage curve.	77
8.5	Phenomenological model of e-beam induced TMR-like behaviour in a spatially confined EPS LPCMO/LAO thin film. (a-f) Temperature dependence of phase domain configuration in e-beam induced microbridge. (g) TMR behaviour and the relative magnetization configuration of metallic phase domains at (h) low R level and (i) high R level, respectively. Note that the arrows in (h) and (i) indicate the orientation of the magnetization in the metallic domains	79
8.6	(a) E-beam scan number vs. maximum TMR curve; a peak was observed at scan number 800. R vs. H curve (b) at scan number 100, (c) at scan number 800, and (d) at scan number 3,500, respectively.	80

9.1	Post annealing effect in spatially confined LPCMO films in (a) Ar gas flowing condition: annealing for 15 min at different temperatures and (b) air flowing condition: annealing for 30 min at different temperatures	87
9.2	The study of AMR manipulation by combination of bridges with different angles (a) A schematic diagram of the sample (LPCMO thin film on STO substrate). (b) AMR result obtained from the combination of Ch1 and Ch4 and (c) combination of Ch2 and Ch4, respectively. Note that (cal)s in (b) and (c) denote the values calculated using data from Ch1 and Ch4 for (b) (and Ch2 and Ch4 for (c)), e.g., $\text{Ch1} + \text{Ch4} (\text{cal}) = 1/2(\text{Ch1}) + 1/2(\text{Ch4})$.	88

Chapter 1

Introduction

1.1 Motivation

The discovery of colossal magnetoresistance (CMR), a 'colossal' change in resistivity upon application of an external magnetic field, in manganese oxide (manganite) has inspired researchers to seek not only the underlying complex physics but also possibilities of using them for next generation applications such as magnetic random access memory (M-RAM) and various types of magnetic sensors. This attractive and complex system has shown rich phase diagrams due to the strong correlation between charge, spin, orbital and lattice degrees of freedom. Many theoretical and experimental studies have shown that manganites are intrinsically inhomogeneous since the system tends to undergo phase separation (typically ferromagnetic metallic (FMM) and anti-ferromagnetic (AF) charge/orbital ordered insulating (COI) domains are involved) near the metal-to-insulator phase transition temperature. [1–7]

Both theoretical and experimental studies have shown that in many manganites the co-existing phases exist as nanometer-scale clusters and percolation can occur between the clusters of the same kind, e.g., joining between two adjacent FMM clusters. [1,2,6] Interestingly, it is experimentally found that not all of the phase separation is on the nanometer-scale. For example, the direct images from the studies of Uehara et al., Murakami et al., and Zhang et al. suggest the existence of the large-scale (up to a few micrometres) phase separation in $(\text{La}_{1-y}\text{Pr}_y)_{1-x}\text{Ca}_x\text{MnO}_3$ systems with $x \sim 0.33$ and $y \sim 0.5$ (in both bulk and film forms). [8–10] This large-scale phase separation is unexpectedly large compared to the nanometer size and implies that another mechanism is required to explain this phenomenon.

Experimentally, the existence of micrometer-scale phase separation in the LPCMO system means that it is able to trap small numbers of phase domains within narrow channels that are of few μm to hundreds nm. The relatively large sizes of the samples (few μm) imply that they are relatively easy to fabricate using conventional photo-lithography and chemical wet-etching techniques. Unlike conventional manganite samples, spatially confined LPCMO thin films have shown unusual electric signals originating from percolation events within the confined region of the sample. Because of the percolative character of the intrinsic phase

domains in spatially confined LPCMO thin films, sudden changes in resistance level can be observed at a certain temperature range where the sizes of the phase domains are comparable to the width of the sample. [12, 13] In this temperature range, relatively small external perturbations (such as temperature, magnetic field, electric field, and more) can cause a significant change in overall resistance level. In these systems, researchers could indeed trap small numbers of electronic phase domains and observe the electronic signals that originate from the percolation event within the narrow region of the samples. [11–14] For example, Zhai et al. reported giant and sharp drops of resistance as the temperature of the sample decreased below the metal-to-insulator phase transition temperature [12] and Wu and Mitchell observed sudden resistance jumps when the external magnetic field is increased at a fixed temperature. [13] The observed resistance jumps in these studies are attributed to the creation or annihilation of the percolation induced conduction path as temperature or external magnetic field is changed. Ward et al. successfully observed the fluctuation between two phases (COI vs. FMM) in a spatially confined $(\text{La}_{1/2}\text{Pr}_{1/2})_{5/8}\text{Ca}_{3/8}\text{MnO}_3$ (LPCMO) system which provides clear evidence for the metastability of the intrinsic phases in the LPCMO system. [14] Singh-Bhalla et al. reported intrinsic tunneling magnetoresistance behaviour in a spatially confined LPCMO system. [11]

The examples above show that the spatially confined manganite system, especially La-Pr-Ca-Mn-O, is an interesting system for experimentally revealing the effects of micro-scale electronic phase separation in manganites. However, a number of transport properties that are scientifically and technologically important were not previously studied in spatially confined manganite systems. In this thesis, I address a number of these novel transport properties in spatially confined $\text{La}_{0.3}\text{Pr}_{0.4}\text{Ca}_{0.3}\text{MnO}_3$ (LPCMO) systems: (a) The low magnetic field response of the CMR, (b) the long time metastability of the resistance, (c) the dependence of the resistance on the direction of the external magnetic field and how this can be manipulated with the bias current, and (d) local phase domain engineering to create the magnetic tunnel junction-like structure.

In the rest of this section, the motivation for investigating the above topics is briefly described:

Keeping in mind that the colossal magnetoresistance in manganites requires high magnitude of external magnetic field (above few Tesla), developing a device with low field colossal magneto-resistance (LF-CMR) could be a major benefit for applications such as nonvolatile memory and electronic sensors. As described in Chapter 4, a spatially confined LPCMO system is a feasible candidate for such LF-CMR due to the percolation-induced resistance jumps within the system that are very sensitive to the strength of the magnetic field. At a certain temperature range the conduction pathway is dominated by a small number of metallic and insulating domains, and hence, the percolation between two adjacent FMM

domains can have a large and sudden effect on the resistance in a spatially confined LPCMO thin film. As a result, the confined system is expected to have a large magnetoresistance effect even at relatively low external magnetic fields.

The time dependence of the resistance in manganites is an important class of transport measurements to investigate the self-organizing nature of inhomogeneous electronic phase separation in both bulk and thin film samples. Depending on the ground state of the system, the resistance can smoothly increase or decrease over the timescale of many minutes. This phenomenon often can be observed at a temperature range where multiple phase domains coexist (near the metal-to-insulator phase transition temperature). Measurements of the time evolution of the resistance of the LPCMO microbridges are essential to understand how the metastability of intrinsic phases affects the percolative behaviour in a spatially confined LPCMO microbridge over a long-time scale. Furthermore, since the electronic states of manganite films are strongly affected by external perturbations such as temperature and magnetic field, a systematic investigation of the response of the phase dynamics to a wide range of these parameters could reveal a deeper understanding on how they modify resistive time relaxation. Such information is important from both a scientific viewpoint as well as for future applications where one may need to control the time relaxation of resistance in reduced geometries of manganites. These issues are described in Chapter 5.

The anisotropic magnetoresistance (AMR) is the change in the resistance that depends on the magnetic field orientation with respect to either the current direction or the crystal axes. This property can be used in devices such as magnetic read head and magnetic switching sensors. In these applications, having a large AMR improves the corresponding sensitivities. In Chapter 6, we demonstrate and discuss how spatially confined LPCMO thin films can produce record-breaking values of the AMR which are several orders of magnitude greater than quantities previously reported in any material. Our discovery of such colossal AMR (C-AMR) will improve the scientific understanding of the electrical properties of spatially confined LPCMO systems, and can also provide important clues on engineering next generation AMR-based devices for technology.

Our discovery of C-AMR behaviour in a spatially confined LPCMO thin films also inspired us to seek further methods of manipulating the C-AMR magnitude. This prompted us to attempt to control the magnitude of the in-plane C-AMR with the d. c. bias current. It is known that applying d. c. electric current stabilizes the metallic state in electronic phase separated manganite thin films and hence we anticipate that the C-AMR will be particularly sensitive to this parameter. These studies are discussed in Chapter 7.

By considering the fact that the electronic phase domains within the spatially confined LPCMO thin film can be as large as the width of the system, a pseudo-low dimensional (pseudo 1- or 2-dimension) electronic device can be fabricated by engineering the phase domains or the boundaries between the phase domains. As shown in Chapter 8, by exposing the spatially confined LPCMO microbridges to an electron beam, we can observe significant

disturbances in their magneto-transport properties. In particular, we find that although scanning electron microscopy (SEM) is one of the most common micro-to-nano scale imaging methods, it could introduce significant damage to the LPCMO samples. This damage may include dislocation of oxygen elements in perovskite-type crystal structure of manganite (LPCMO) where Mn - O - Mn bond angle plays a key role for the electron conduction within the system. Using this experimental result, we attempt to create an artificial potential wall across the microbridge in which the nature of the electron tunneling depends on the relative magnetization directions of adjacent metallic phase domains. Our discovery of tunneling magnetoresistance behaviour in electron beam scanned LPCMO microbridges sheds light on how it can be used as a phase domain engineering technique for developing next generation electronic phase separation(EPS)-based devices.

1.2 Thesis Organization

In this thesis, I have studied novel magneto-transport properties of spatially confined thin films of $\text{La}_{0.3}\text{Pr}_{0.4}\text{Ca}_{0.3}\text{MnO}_3$. Brief descriptions of each chapter are given below:

Chapter 1 Motivations for the investigation of spatial confinement phenomenon in LPCMO thin films are described.

Chapter 2 Fundamental theoretical background is discussed: brief introduction to the physics of manganites and spatial confinement phenomenon in electronic phase separated manganite thin films.

Chapter 3 Experimental techniques are introduced: review of experimental methods (target preparation, thin film deposition, photo-lithography, transport measurement).

Chapter 4 The characteristics of the magneto-resistance in spatially confined thin films of $\text{La}_{0.3}\text{Pr}_{0.4}\text{Ca}_{0.3}\text{MnO}_3$ (LPCMO) are investigated: "*Re-entrant of magneto-resistance peak due to spatial confinement in LPCMO microbridge.*"

Chapter 5 Time dependence of the resistance relaxation in spatially confined LPCMO thin films is studied: "*Field-dependent resistive evolution in spatially confined LPCMO thin films.*"

Chapter 6 By tuning the geometry of LPCMO thin films, colossal anisotropic-magnetoresistance (AMR) is achieved: "*Colossal AMR in spatially confined LPCMO thin films.*"

Chapter 7 Bias current dependence of the C-AMR is investigated: "*Current dependence of colossal anisotropic magnetoresistance in LPCMO microbridges.*"

Chapter 8 Electron beam induced tunneling magnetoresistance (TMR)-like behaviour in spatially confined LPCMO thin films is studied.

Chapter 9 Summary, conclusions and directions for future works are presented.

1.3 List of Publications

2013 - 2016

(1) **J. Jeon**, H. S. Alagoz, R. Boos, J. Jung, and K. H. Chow, “*Reentrant low-field magneto-resistance in $\text{La}_{0.3}\text{Pr}_{0.4}\text{Ca}_{0.3}\text{MnO}_3$ film due to spatial confinement*,” Appl. Phys. Lett. **104**, 122405 (2014).

(2) **J. Jeon**, H. S. Alagoz, J. Jung, and K. H. Chow, “*Surface inhomogeneities and the electronic phase separated states in thin films of $\text{La}_{0.3}\text{Pr}_{0.4}\text{Ca}_{0.3}\text{MnO}_3$* ,” J. Appl. Phys. **115**, 233907 (2014).

(3) **J. Jeon**, H. S. Alagoz, J. Jung, and K. H. Chow, “*Low field colossal anisotropic magnetoresistance in spatially confined electronically phase separated $\text{La}_{0.3}\text{Pr}_{0.4}\text{Ca}_{0.3}\text{MnO}_3$ microbridges*,” Appl. Phys. Lett. **107**, 052402 (2015).

(4) **J. Jeon**, H. S. Alagoz, J. Jung, and K. H. Chow, “*Field Dependence of the Resistance Steps in Spatially Confined $\text{La}_{0.3}\text{Pr}_{0.4}\text{Ca}_{0.3}\text{MnO}_3$ thin films*,” J. Phys. Soc. Jpn. **85**, 044706 (2016).

(5) **J. Jeon**, J. Jung, and K. H. Chow, “*Current dependence of colossal anisotropic magnetoresistance in $\text{La}_{0.3}\text{Pr}_{0.4}\text{Ca}_{0.3}\text{MnO}_3$ microbridges*,” Submitted to J. Appl. Phys. (2016).

(6) H. S. Alagoz, **J. Jeon**, S. T. Mahmud, M. M. Saber, B. Prasad, M. Egilmez, K. H. Chow, and J. Jung, “*Recovery of oscillatory magneto-resistance in phase separated $\text{La}_{0.3}\text{Pr}_{0.4}\text{Ca}_{0.3}\text{MnO}_3$ epitaxial thin films*,” Appl. Phys. Lett. **103**, 232402 (2013).

(7) H. S. Alagoz, **J. Jeon**, R. Boos, R. H. Ahangharnejhad, K. H. Chow, and J. Jung, “*Ultra-sharp oscillatory magneto-resistance in spatially confined $\text{La}_{0.3}\text{Pr}_{0.4}\text{Ca}_{0.3}\text{MnO}_3$ epitaxial thin films*,” Appl. Phys. Lett. **105**, 162409 (2014).

(8) M. A. B. Narreto, H. S. Alagoz, **J. Jeon**, K. H. Chow, and J. Jung, “*Dynamic distortions and polaronic effects in the paramagnetic state of $\text{La}_{0.8}\text{Ba}_{0.2}\text{Mn}_{1-x}\text{Al}_x\text{O}_3$ manganites*,” J. Appl. Phys. **115**, 223905 (2014).

(9) H. S. Alagoz, **J. Jeon**, S. Keating, K. H. Chow, and J. Jung, “*Evolution and sign control of square-wave-like anisotropic magneto-resistance in spatially confined $\text{La}_{0.3}\text{Pr}_{0.4}\text{Ca}_{0.3}\text{MnO}_3$ / $\text{LaAlO}_3(001)$ manganite thin films*,” J. Appl. Phys. **119**, 143905 (2016).

Chapter 2

Basic Features of Manganites

The manganese oxides, also called manganites, have been extensively studied in the past several decades because they possess interesting physical properties, such as colossal magnetoresistance (CMR) and giant anisotropic magnetoresistance (AMR). These properties are illustrated by Fig. 2-1 which shows representative curves of the temperature dependence of the resistance in a manganite thin film ($\text{La}_{0.3}\text{Pr}_{0.4}\text{Ca}_{0.3}\text{MnO}_3$), showing a metal-to-insulator phase transition at T_{MIT} , under different conditions. One can notably observe a significant reduction of the resistance compared to 0 T when a magnetic field of 1 T is applied (Fig. 2-1(a)). This dramatic change in the resistance upon the application of a magnetic field is called colossal magnetoresistance (CMR). The CMR values in certain manganites are as high as $\sim 10^6$ %, a 'colossal' magnitude of magnetoresistance. Another interesting aspect of the manganite is shown in Fig. 2-1(b). The values of the resistance changes with the direction of external magnetic field with respect to the current direction. The changes in the resistance depending on the direction of the magnetic field with respect to either the current direction or the crystal axes is called anisotropic magnetoresistance (AMR). The magnitude of the AMR in notable manganites (20 \sim 100 %) is significantly larger than that of 3d metal alloys (2 \sim 4 %). [17, 18, 64, 65]

In many of these manganites, co-existence of energetically similar competing electronic phases such as ferromagnetic metallic (FMM), charge ordered insulating (COI), charge disordered insulating (CDI), and/or paramagnetic insulating (PI) plays a dominant role in determining the CMR material's magneto-transport properties. [1-4, 8, 19] From both theoretical and experimental studies, the co-existence of the competing phases in many manganites is known to have the following properties; (1) the electronic phases exist as nanometre-scale clusters (e.g., FMM and COI domains) and (2) percolation can occur between the nanometre-scale electronic phase clusters of the same kind, e.g., joining of two adjacent FMM domains. [1, 2, 6]

However, as described in Chapter 1, not all of the phase clusters are on the nanometre-scale and in some systems can be as large as micrometers (found only in experimental studies). This intrinsic self-organized electronic inhomogeneity is particularly sensitive to manipula-

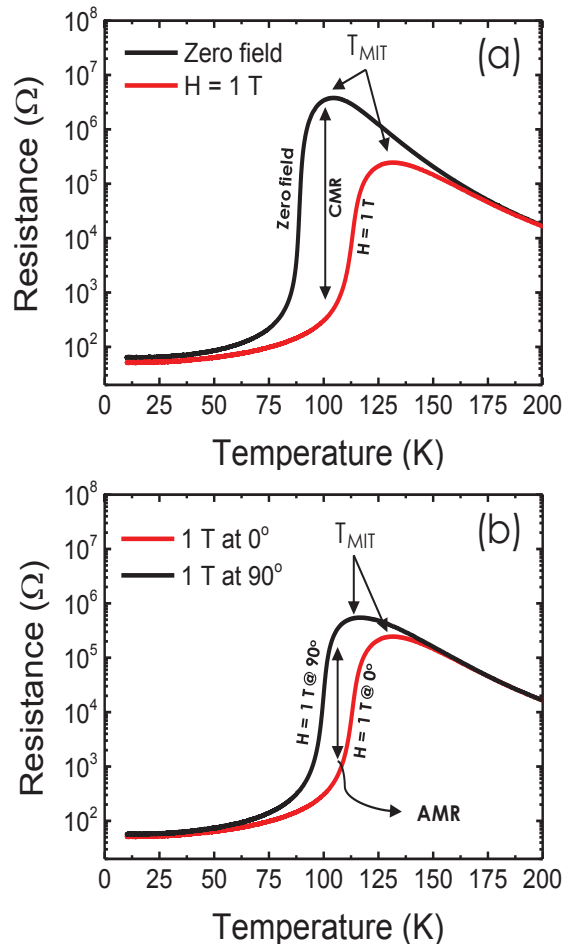


Figure 2.1: Examples of the CMR and the AMR in a wide manganite ($\text{La}_{0.3}\text{Pr}_{0.4}\text{Ca}_{0.3}\text{MnO}_3$) thin film: (a) Resistance vs. Temperature, $R(T)$ at $H = 0$ T (zero field) and at $H = 1$ T. (b) $R(T)$ at field (1 T) orientation parallel (at 0 degree) and perpendicular (90 degree) to the current direction, respectively.

Perovskite-Type Manganite Structure $RE_{1-x}AE_xMnO_3 : ABO_3$

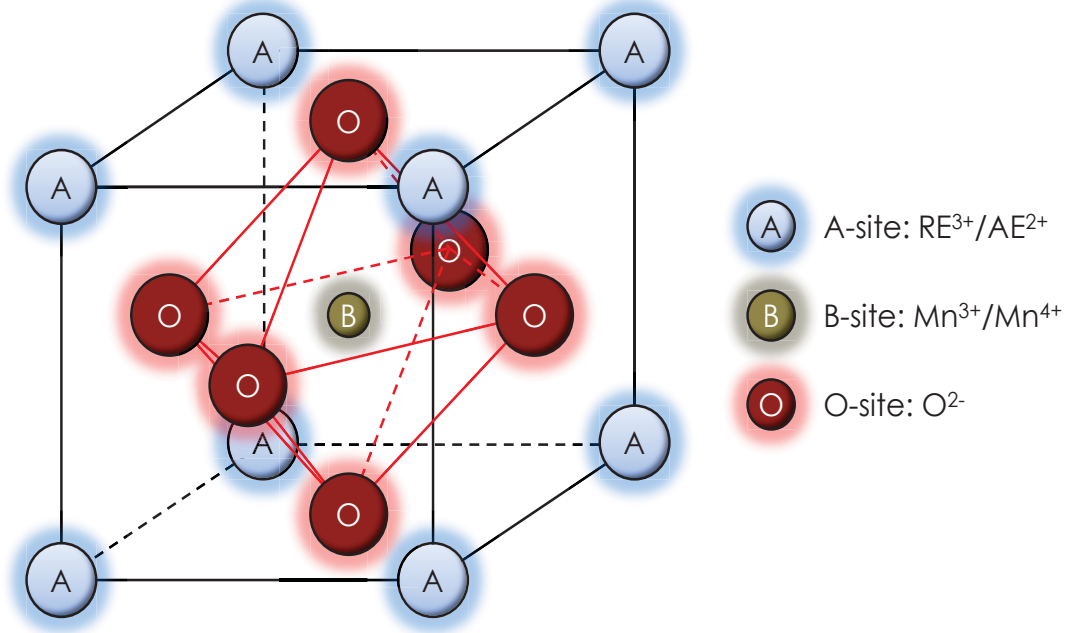


Figure 2.2: Cubic-perovskite structure of manganites. A-site contains large ions of rare earth trivalent lanthanide cation (e.g. La^{3+} , Sm^{3+}) or alkaline earth divalent (e.g. Ca^{2+} , Sr^{2+} , Ba^{2+}) elements. B-site contains Mn^{3+} or Mn^{4+} ions (relative smaller). The oxygen atoms surround the B-sites(Mn) with octahedral configuration.

tion via chemical doping, structural modifications, strain induction, and the application of external perturbations such as electric and magnetic fields. [1, 2, 6] Hence, electronic phase separated materials not only provide unique opportunities towards improving the understanding of the complex physics behind electronically phase separated systems, they also enable researchers to utilize their highly sensitive phase tunability for new applications. In the remainder of this chapter, I describe basic features of manganites that are useful for the qualitatively understanding of the exotic transport properties of hole doped manganites.

2.1 Structure of manganese oxides

Manganese oxides or manganites, $Re_{1-x}Ae_xMnO_3$, where Re is a rare earth trivalent element (e.g., La^{3+} , Sm^{3+}) and Ae is an alkaline earth divalent element (e.g., Ca^{2+} , Sr^{2+} , Ba^{2+}), generally form a nearly cubic perovskite-type structure which has the general formula of ABO_3 (see Fig. 2-2). In perovskite manganites, Re^{3+} and/or Ae^{2+} ions are located on the A-site (cubic environment; their relative amounts depend on the divalent element doping concentration x) and the Mn ion occupies the B-site at the center of the unit cell. The oxygen ions surround the Mn ion in an octahedral configuration.

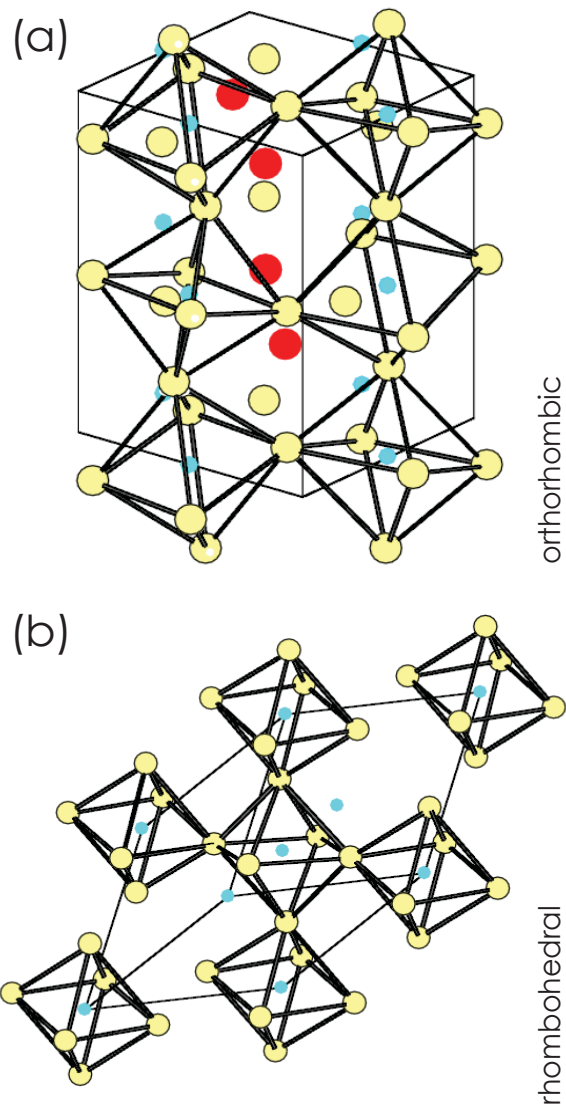


Figure 2.3: Structures of distorted perovskites of manganite due to the connection pattern of MnO_6 octahedra in the lattice structure: (a) orthorhombic and (b) rhombohedral. The figure is produced from Ref. [20].

The structures of manganites often show lattice distortion and are not exactly cubic. Two reasons are often considered as origins of the structural distortion in a manganite: (1) the Jahn-Teller effect, which occurs in a high-spin ($S = 2$) $\text{Mn}^{3+}(d^4)$ parent manganite, can deform the MnO_6 octahedron structure (see next section). (2) A lattice deformation can also occur from the connection pattern of MnO_6 octahedra in the lattice structure that forms the rhombohedral and orthorhombic structures in which the MnO_6 octahedra have alternating buckling (shown in Fig. 2-3). [20] The distortion of the structure can be quantized by a tolerance factor, f , defined by

$$f = \frac{(r_A + r_O)}{\sqrt{2}(r_B + r_O)}, \quad (2.1)$$

where r_A , r_B and r_O are the ionic sizes of A-, B- and O-site elements, respectively. Typical ion sizes are: $\text{La}^{3+} = 1.22 \text{ \AA}$, $\text{Ca}^{2+} = 1.06 \text{ \AA}$, $\text{Mn}^{3+} = 0.70 \text{ \AA}$, $\text{Mn}^{4+} = 0.52 \text{ \AA}$, and $\text{O}^{2-} = 1.32 \text{ \AA}$. [21] If $f \sim 1$, one can expect nearly cubic environment while $0.96 < f < 1$ forms rhombohedral (Fig. 2-3(b)) and $f < 0.96$ forms orthorhombic environment (Fig. 2-3(a)), respectively. The distorted environments with $f < 1$ accompany a bend of B - O - B bond angle which strongly affects the e_g electron hopping amplitude within the double exchange model. [22] As a result, the transport properties of manganites depend on doping level of alkaline earth divalent elements in A-site and the average size of the cations (A-site). The doping level, which controls the ratio between Mn^{3+} and Mn^{4+} ions, plays a key role in producing different types of electronic phases such as ferromagnetic metallic (FMM), anti-ferromagnetic insulating (AFI), paramagnetic insulating (PMI) and charge ordered insulating (COI) states. Changing/controlling the cation size by different ion doping leads to a distortion of the crystal structure of the manganite, resulting in distortions of the Mn - O - Mn bonds which reduces the hopping amplitude (will be discussed later in this chapter).

2.2 Crystal field effect and Jahn-Teller effect

In this section, we aim to explain how the electronic states and associated energies of manganites behave when Mn ions interact with oxygen ions that surround the Mn ions.

2.2.1 Perturbation due to the crystal: crystal field effect

The isolated manganese element, Mn, has five degenerate d-shell levels. The shapes of the five different orbitals are shown in Fig. 2-4(a) (d_{xy} , d_{yz} , d_{xz} , $d_{x^2-y^2}$ and $d_{3z^2-r^2}$). The degeneracy is present due to rotational invariance within the angular momentum $l = 2$ subspace. However when the Mn ion is surrounded by O ions, some directions of the crystal axes are certainly different compared to other directions due to the interaction between the Mn and O ions as shown in examples of $\text{Mn}(3d_{xy})$ and $\text{O}(2p_{x,y})$ (Fig. 2-4(b)) vs. $\text{Mn}(3d_{x^2-y^2})$ and $\text{O}(2p_{x,y})$ (Fig. 2-4(c)). This results in a splitting of the energies of the five $l = 2$ levels which is called the Crystal-field splitting.

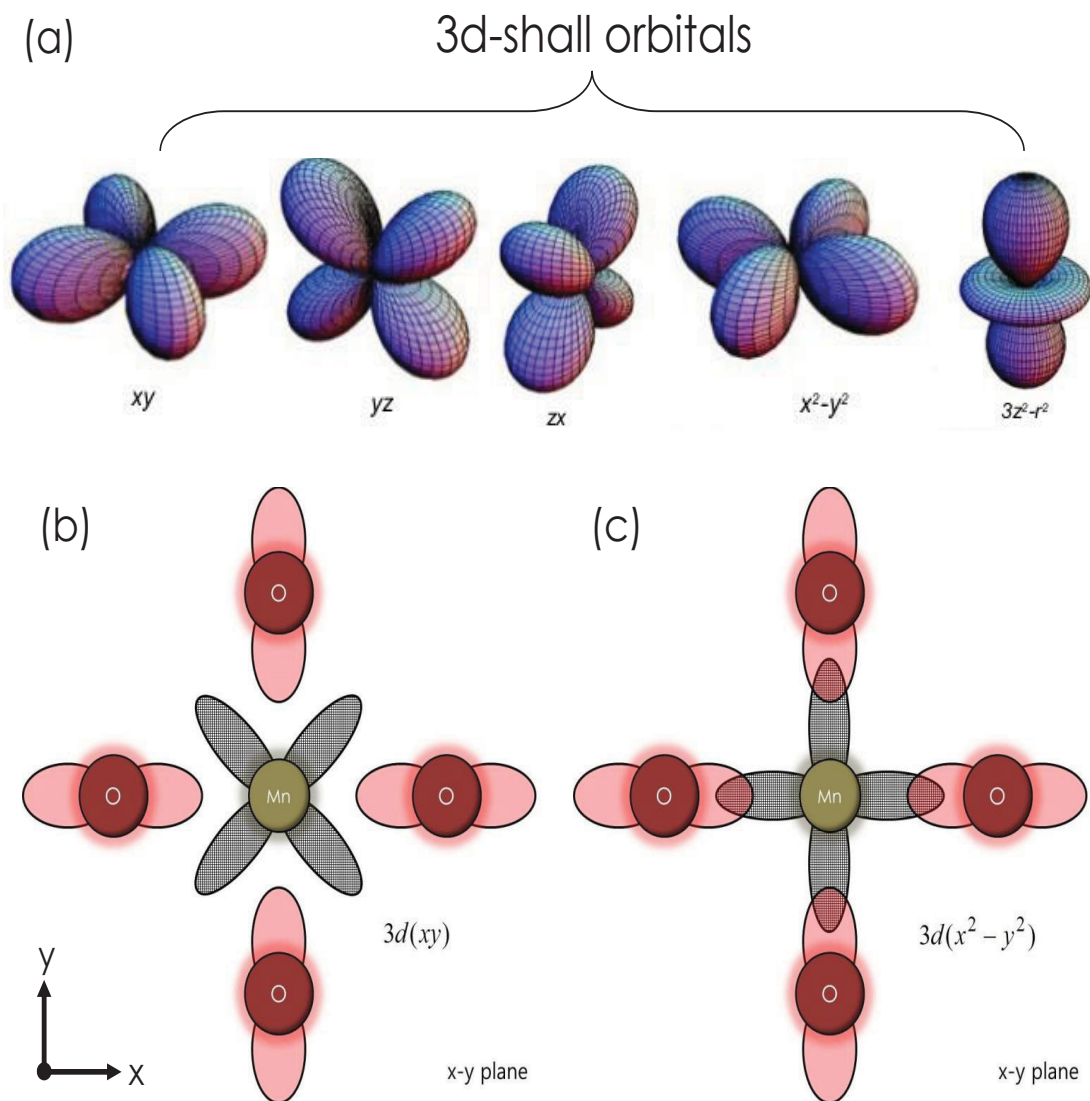


Figure 2.4: (a) The shapes of the five different orbitals of d-shell. (b) Crystal field effect between $3d_{xy}$ and $2p_{x,y}$. (c) Crystal field effect between $3d_{x^2-y^2}$ and $2p_{x,y}$.

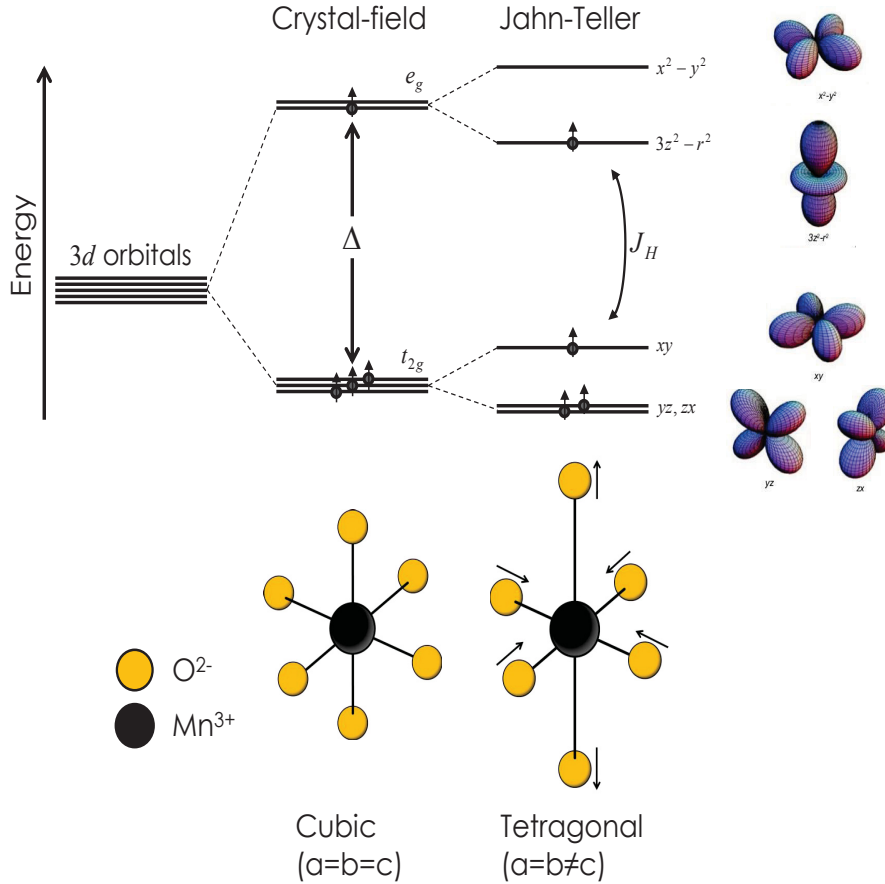


Figure 2.5: A schematic diagram of the Crystal-field splitting and Jahn-Teller effect: In the crystal field effect, the five degenerate orbitals split into the t_{2g} triplet levels and an e_g doublet. Due to the orbital-lattice interaction in $\text{Mn}^{3+}(d^4)$ parent manganese oxide, further splitting of the degeneracy occurs called the Jahn-Teller effect.

By symmetry, the d_{xy} , d_{yz} , and d_{zx} orbitals have the same energy if the three axes (x , y , z) are equivalent (cubic environment). Thus, they form a triplet. The other two orbitals $d_{x^2-y^2}$ and $d_{3z^2-r^2}$ form a doublet. Note that the triplet must have a lower energy than the doublet: As shown in the Fig. 2-4(c), the orbitals of doublet point along the directions where the oxygen ions are located (compare with Fig. 2-2) and hence the Coulomb repulsion increases the energy.

The actual splitting of the energies (Δ) is found to be about $1 \sim 2$ eV for manganites (both in theory and experiment). [23–25]

2.2.2 Jahn-Teller effect

In the crystal-field splitting, we considered the cubic symmetry that leads to an energy splitting into the t_{2g} triplet and e_g doublet (see Sec. 2.2.1). These remaining degeneracies can be further broken by the lattice motion/displacement. In $\text{Mn}^{3+}(d^4)$ parent manganese

oxide, the oxygen ions surrounding the Mn ion can re-adjust their positions, breaking the symmetry that leads to further splitting of the degeneracy. The splitting of the degeneracy due to the orbital-lattice interaction is called the Jahn-Teller effect. A schematic diagram of the Jahn-Teller effect is shown in Fig. 2-5. The Jahn-Teller effect tends to occur spontaneously because the energy penalization of the lattice distortion grows as the square of that distortion, while the energy splitting of the otherwise degenerate orbitals is linear. For this reason, it is energetically favorable to spontaneously distort the lattice thus removing the degeneracy. [25] Now, let us discuss the Jahn-Teller effect with a simple phenomenological model. [26] Assume that 'Q' is the distortion of the system (the distance of the distortion along a normal mode coordinate). The energy associated with Q can be written as;

$$E(Q) = \frac{1}{2}M\omega^2Q^2 \quad (2.2)$$

where M and ω are the mass of the anion and the angular frequency at a normal mode, respectively. Here, the E_{min} is zero when $Q = 0$ (no distortion). Phenomenologically, the distortion raises certain orbitals' energies while lowering the others. If all orbitals are either completely filled or empty, the overall energy can be described by eqn (2-2). When the orbitals are partially filled, the system can have a change in the total energy. In this case, the electronic energy dependence on Q could be very complicated, but one can write it as a Taylor series in Q, i.e., $E_{partial}(Q) \approx AQ + BQ^2 + CQ^3 + \dots$. If we assume Q is small, we can keep only the linear term (AQ or $-AQ$ corresponding to a raising or a lowering of the electronic energy where A is a positive constant). Then,

$$E(Q) = \pm AQ + \frac{1}{2}M\omega^2Q^2 \quad (2.3)$$

By the choice of the sign, two separated curves will be obtained (see Fig. 2-6). To find the minima, one can use $\partial E/\partial Q = 0$ which yields Q_0 by

$$Q_0 = \frac{A}{M\omega^2} \quad (2.4)$$

for the negative energy. Substituting this Q_0 into eqn (2-4), we can get the minimum energy.

$$E_0 = \frac{-A^2}{2M\omega^2} < 0 \quad (2.5)$$

If only this orbital (with Q) is occupied, then the system can save the net energy by spontaneously distorting the structure. Further numerical calculation can be found in p.63 - 69. [25]

So far, we have considered a static Jahn-Teller effect because the distortion is fixed on a particular axis of an octahedron. However, the distortion can change from one axis to another at high temperatures due to thermal excitation which is called a 'dynamic' Jahn-Teller effect. Another type of dynamic JT can be found in divalent doped manganites

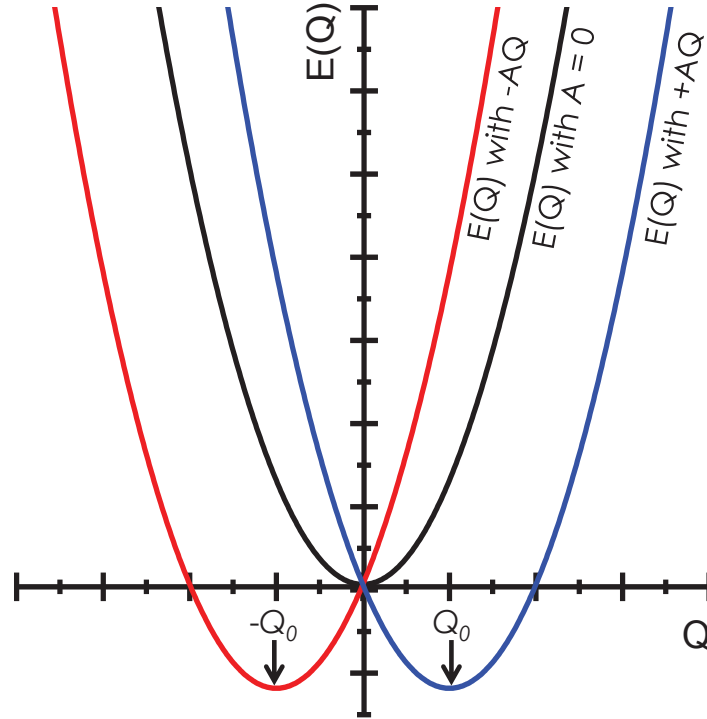


Figure 2.6: The energy of an octahedral structure as a function of distortion, Q according to eqn (2-3) and (2-4), respectively.

($\text{Re}_{1-x}\text{Di}_x\text{MnO}_3$) where $\text{Mn}^{3+}(d^4)$ and $\text{Mn}^{4+}(d^3)$ coexist with a ratio $(1 - x) : x$. While the $\text{Mn}^{4+}(d^3)$ parent manganite, such as CaMnO_3 , has no electron in an e_g level and hence it has no Jahn-Teller distortion induced energy splitting, the $\text{Mn}^{3+}(d^4)$ parent manganite such as LaMnO_3 which has a single electron in every e_g level undergoes the Jahn-Teller distortion. These undoped manganites (both $\text{Mn}^{4+}(d^3)$ and $\text{Mn}^{3+}(d^4)$ parent manganites) are electrical insulators: For the $\text{Mn}^{4+}(d^3)$ parent manganites there are no hopping e_g electrons and hence the system naturally is an insulator. By contrast, the $\text{Mn}^{3+}(d^4)$ parent manganites have an electron in every e_g level (see Fig. 2-5). However, the electrons cannot hop between atoms due to the Pauli exclusion principle (the spins with the same orientation cannot occupy the same energy level). Note that the spins in the $\text{Mn}^{4+}(d^3)$ parent manganites order in a more complex manner due to the Jahn-Teller effect and super-exchange interaction (this will be discussed in the following section). However, when divalent ions such as Ca^{2+} and Sr^{2+} are doped into $\text{Mn}^{3+}(d^4)$ parent manganites, the system contains both $\text{Mn}^{3+}(d^4)$ and $\text{Mn}^{4+}(d^3)$ and hence some of the e_g levels are empty. As a result, the e_g electrons in $\text{Mn}^{3+}(d^4 : t_{2g}^3 e_g^1)$ can hop to empty e_g levels in $\text{Mn}^{4+}(d^3 : t_{2g}^3 e_g^0)$ which creates conduction electrons as discussed in the following section.

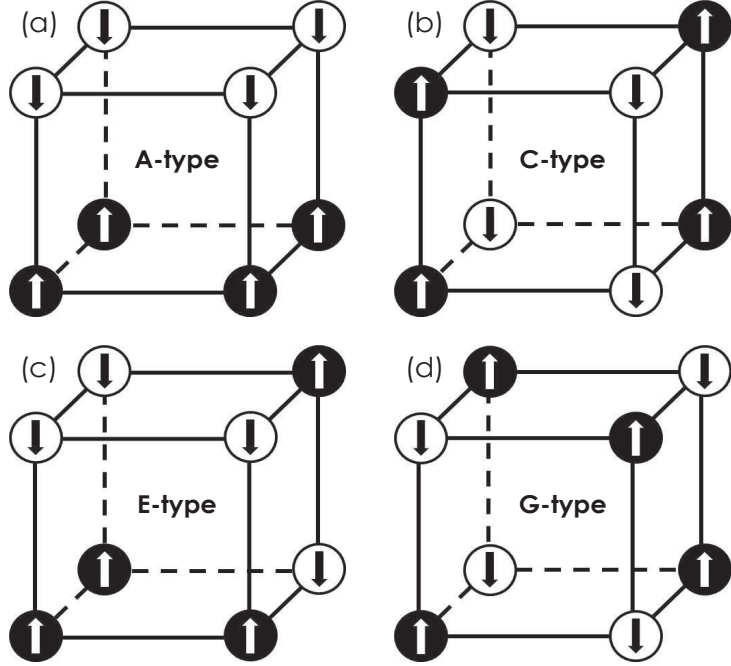


Figure 2.7: Four different types of antiferromagnetic order: (a) A-type, (b) C-type, (c) E-type, and (d) G-type, respectively.

2.3 Double exchange model

In this section, an early theoretical work for qualitatively understanding the ferromagnetic metallic behaviour in manganites is presented. As discussed in the previous section, $\text{Mn}^{3+}(d^4 : t_{2g}^3 e_g^1)$ parent manganite has 4 electrons (3 electrons in every t_{2g} level and 1 electron in every e_g level) with total spin of 2 ($S = 2$). All electrons are subject to electron repulsion/correlation effect. The electrons in the e_g state strongly correlate with O_{2p} states and tend to localize forming an antiferromagnetic (AF) insulator due to super-exchange (SE) interaction. [27] For example, LaMnO_3 shows A-type ordering in which the ferromagnetic ab plane is coupled antiferromagnetically along the c -axis. [27] This occurs by the Jahn-Teller distortion of Mn^{3+} ions which gives alternate long and short Mn - O bonds within the (100) plane. The orbitals on neighbouring Mn^{3+} ions are differently oriented and the super-exchange (SE) leads to an interaction between an occupied orbital on one atom with an unoccupied orbital on its neighbour. The in-plane interaction is thus ferromagnetic while the out-of-plane interaction is AF because of the SE interaction. Fig. 2-7(a)-(d) show 4 different types of antiferromagnetic order.

However when divalent ions such as Ca^{2+} or Sr^{2+} are doped with a certain proportion ($\sim 30\%$ is usually an optimum range) the e_g electrons can hop and hence act as conduction electrons. The t_{2g} electrons are stabilized by the crystal-field splitting and localized by the strong correlation effect ($S = 3/2$). Due to Hund's rule there exists a strong coupling between t_{2g} localized electrons ($S = 3/2$) and e_g conduction electron ($S = 1/2$). The

exchange energy J_H is about $2 \sim 3$ eV in manganites and exceeds the hopping interaction t_{ij}^0 of the conduction e_g electron between the neighbouring sites, i and j . For the case of $J_H \gg t_{ij}$ (strong coupling condition), the effective hopping interaction t_{ij} can be expressed by (Anderson-Hasegawa relation [28])

$$t_{ij} = t_{ij}^0 \cos(\theta_{ij}/2) \quad (2.6)$$

As shown in the equation above, the magnitude of the hopping depends on the relative angle (θ_{ij}) between the neighbouring spins (Mn^{4+} - Mn^{3+}). The ferromagnetic interaction via the exchange of the conduction electron whose spin has on-site coupling with the local spin (t_{2g}) is called "double-exchange interaction" (named "double" exchange interaction since the hopping occurs through the O_{2p} state). A schematic diagram is shown in Fig. 2-8(a).

The double exchange (DE) model qualitatively explains the ferromagnetic behaviour of manganites (below the metal-to-insulator phase transition temperature T_{MIT}). The different situations are qualitatively shown in Fig. 2-8(b)-(e). In an undoped manganite, the spins arrange antiferromagnetically due to the SE interaction in which the hopping magnitude becomes zero ($\theta_{ij} = 180^\circ$, Fig. 2-8(b)). Hence, insulating behaviour is expected in this configuration. At low temperature ($T \ll T_{MIT}$) of divalent doped manganite, ferromagnetic order of the spins is observed and it maximizes the hopping amplitude (conductivity) of the sample (Fig. 2-8(c)). Note that the e_g electron on a Mn^{3+} ion can only hop when spins between t_{2g} on Mn^{3+} and Mn^{4+} are aligned since the e_g electron and the 3 electrons in the t_{2g} level want to keep the spin orientations aligned due to J_H (Hund's coupling). Thus ferromagnetic alignment of neighbouring ions is required to keep the high-spin arrangement on both the donating and receiving ions. Since the ability to hop gives a kinetic energy saving, this allows the hopping process to reduce the overall energy. Therefore, ferromagnetic alignment allows the e_g electrons to hop through the crystal and the material becomes metallic. Near T_{MIT} , the spins orient in random directions (dynamically distorted) due to thermal-dynamic vibrations (Fig. 2-8(d)). Hence the hopping interaction is lowered because the angle between the neighbouring spins is increased. However, when a magnetic field is applied at this temperature, the spins tend to align along the external magnetic field and reduce the effective angle between the spins. This increases the hopping interaction which lowers the resistivity of the system leading to large magneto-resistance (CMR) behaviour (Fig. 2-8(e)). [29]

2.4 Phase separation and percolation model

The double exchange (DE) model discussed in the previous section explains how ferromagnetic metallic can arise in doped manganites with a simple but powerful concept. However, subsequent studies have shown that the DE model produces wrong T_{MIT} values (one even

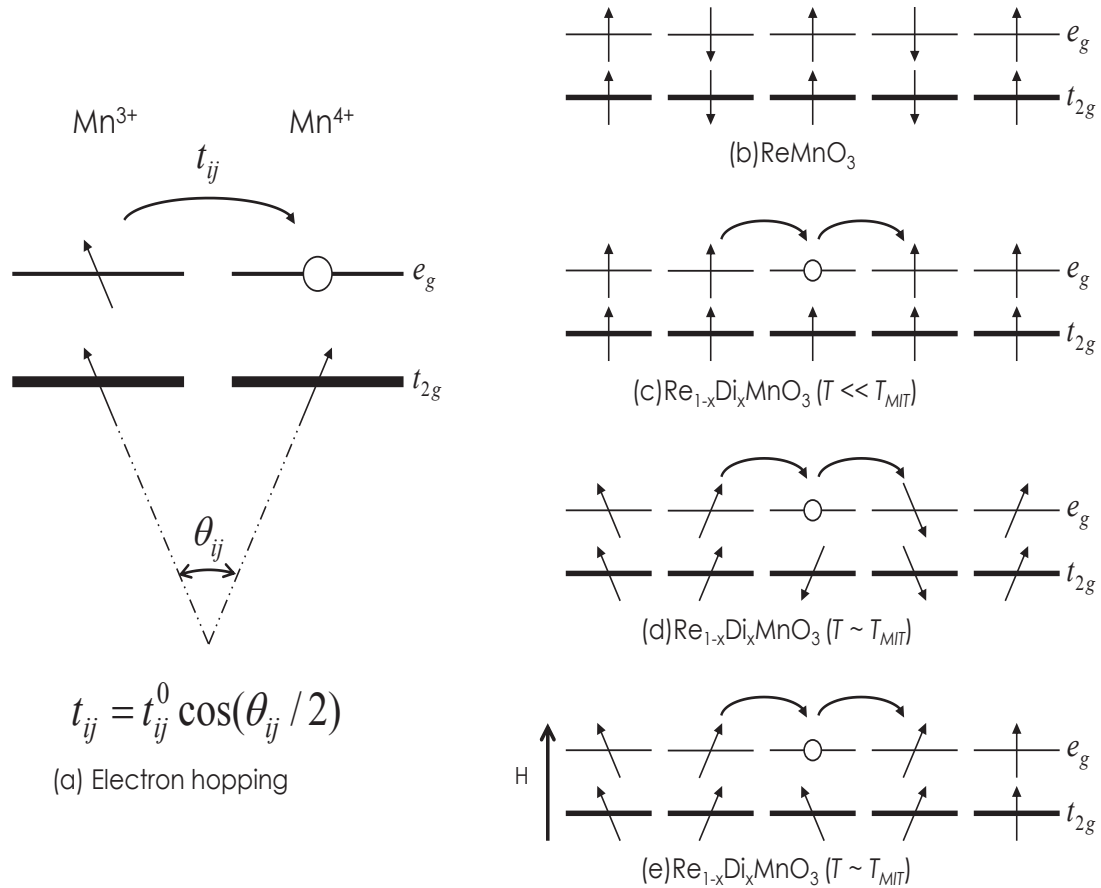


Figure 2.8: (a) A schematic diagram of double exchange interaction. (b) Antiferromagnetic order of undoped manganite. (c) Ferromagnetic order of divalent doped manganite at low temperature. (d) The spin orientations near the metal-to-insulator phase transition temperature where the spins orient in random direction due to thermal-dynamic vibrations. (e) The effect of external magnetic field near the metal-to-insulator phase transition temperature. [29]

found insulating behaviour below T_{MIT} or metallic behaviour above T_{MIT}) by a large factor. [30–32] Furthermore, more recent studies strongly suggest that manganites are intrinsically inhomogeneous due to the co-existence of the competing phase clusters (domains) while the DE model assumes that manganites are uniform and homogeneous. [28, 33] Such incomplete explanations have demanded other models to understand the transport properties of manganites.

From both theoretical and experimental studies, the presence of nano-scale electronic phase separation and percolation of phase separated clusters in manganites are now believed to play a prominent role in its intriguing transport properties such as the CMR effect. [1, 2] In this thesis, the percolation model is important for understanding the "spatial confinement phenomenon". In a spatially confined manganite, such as the LPCMO system, lateral sizes of phase domains are comparable to the width of the sample in which only a few phase domains can be trapped within the confined region. In such a situation, a single percolation event can cause a significant change in the overall resistance of the system.

As a simple example to qualitatively understand the notion of percolation, one can use a checkerboard plate where each space is occupied randomly with a probability p . The occupied spaces are filled in grey. In a random distribution of these spaces "clusters (black)" will be formed which are the sets of the several occupied spaces directly linked. Percolation deals with the links of these "clusters". Now, imagine that water can only flow through the occupied spaces (grey and/or black). As p increases there will be more links where the water can flow. And at a certain p (called threshold p), water can flow from A to B where the system actually percolates. This scenario is illustrated in Fig. 2-9: when $p = 0.2$, 20 percent of the checkerboard is occupied and few clusters are formed by direct links between the occupied states. However, at $p = 0.2$, a path from A to B is not formed, hence no flow of water is expected. At $p = 0.5$, 50 percent of the checkerboard is occupied and many clusters are formed that actually create a path from A to B in which flow of water is expected.

Note that the notion of percolation is not restricted to a certain shape but can be formed in any shape. In manganites, the percolation model is applied to study the electronic phase separation where black and white spaces correspond as ferromagnetic metallic (FMM) and charge ordered insulating (COI) phase domains, respectively. Now, the colossal magnetoresistance (CMR) behaviour in manganite can be explained by the percolation model. When the system's temperature is near the metal-insulator transition temperature, small and discontinued FM clusters (domains) are seeding randomly within the insulating background. However, the fraction of FM clusters grow as the external magnetic field is applied and percolates at some point. Here, a dramatic drop of the resistivity is expected due to the creation of a conduction path which leads to CMR behaviour.

Recent experimental work with advanced imaging techniques show direct evidence of the

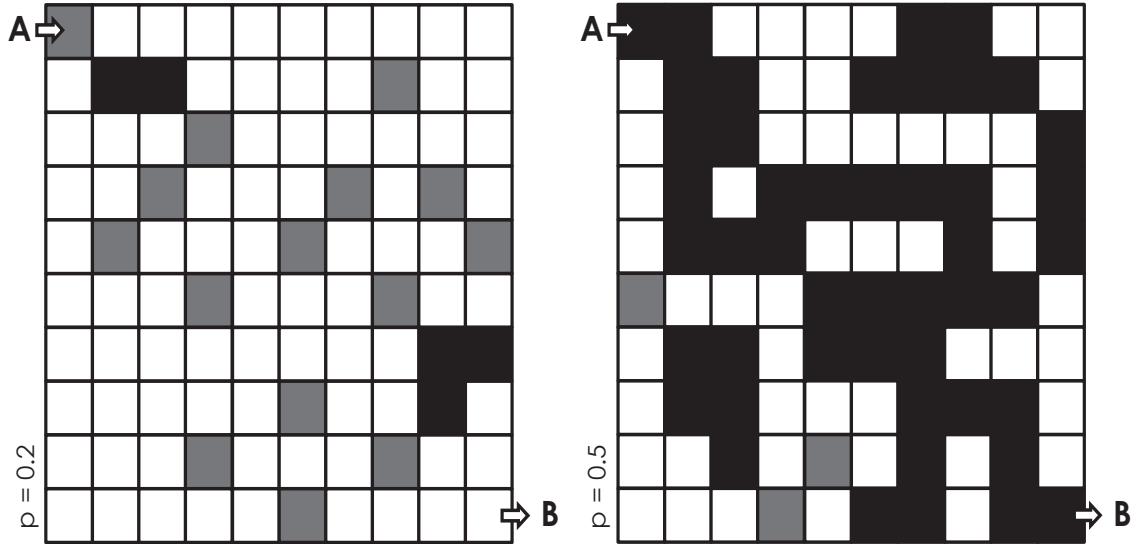


Figure 2.9: (Left) Random occupation of spaces with $p = 0.2$ where white, grey and black are unoccupied state, occupied state and cluster of the occupied states, respectively. (Right) Random occupation of spaces with $p = 0.5$ where the system percolates.

percolation phenomenon of micrometer size phase separation. [8–10] This micrometer scale phase separation seen in experiments does not seem to be well addressed in existing condensed matter physics theories; hence a phenomenological percolation model is often being used to explain the underlying mechanism of the observed events. [25]

2.5 Spatial confinement phenomenon in manganite system

Recent experimental studies of spatially confined films, i.e. where the lateral dimensions of the films are comparable to the size of inherent phase domains, have presented unique magneto-transport behaviour. A schematic illustration of spatial confinement in a manganite is shown in Fig. 2-10. In an electronic phase separated manganite, competing phases (usually charge ordered insulating (COI) phase (check pattern background) and ferromagnetic metallic (FMM) phase (dark blue)) co-exist near the metal-to-insulator phase transition temperature. The current flows through the FMM domain connections. However, if the lateral width of the system is reduced to the size of the inherent phase domains, the overall resistance can be significantly changed by the status of FMM domains within the narrow region. For example, when the FMM domains are separated by a COI domain a high resistance level is expected while the connection of FMM domains (percolation) significantly lowers the overall resistance. Hence in such a system percolation through the confined region plays a main role in determining its electronic transport properties.

For example, Zhai et al. found giant and ultrasharp discrete resistance steps near the metal-insulator transition in spatially confined $(\text{La}_{5/8-0.3}\text{Pr}_{0.3})\text{Ca}_{3/8}\text{MnO}_3$ wires (shown

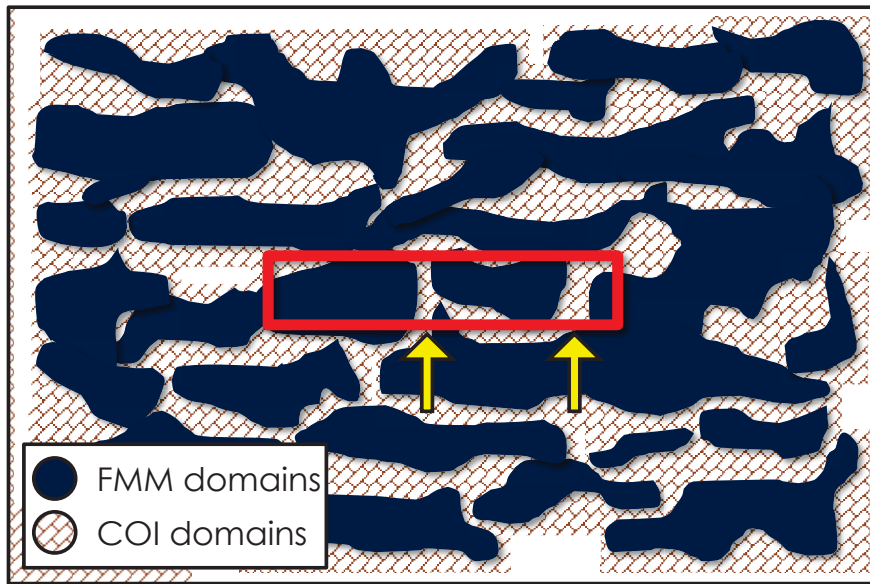


Figure 2.10: A schematic illustration of spatial confinement in manganite: in manganite system, ferromagnetic metallic (FMM) phase domains (dark blue) grow within the background of charge ordered insulating (COI) phase domains (check pattern background) and one can imagine the current easily flows through FMM domains. However, when the system's width is reduced to the size of the phase domains (red rectangle, spatial confinement), the conduction path can be annihilated or created by the percolation of FMM domains within the spatially confined region (the arrows indicate disconnection of FMM domains; when the FMM domains join a sharp resistance jump is expected). Figure is reproduced from Ref. [12].

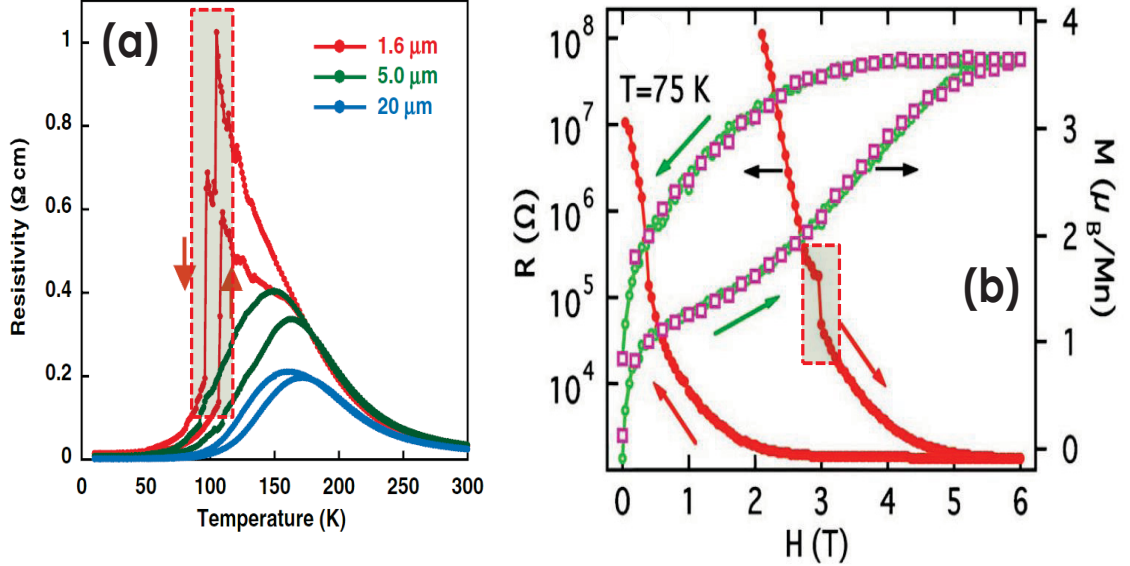


Figure 2.11: (a) Resistivity vs. temperature profiles for $(\text{La}_{(5/8-0.3)}\text{Pr}_{0.3})\text{Ca}_{3/8}\text{MnO}_3$ wires on LAO substrate under a 3.75 T external magnetic field. Sharp jumps of resistivity can be seen near the metal-to-insulator phase transition temperature for both cooling and warming process. [12] (b) Resistance vs. magnetic field curves and magnetization vs. magnetic field (with different field steps: 2000 Oe/step and 500 Oe/step, respectively) for $\text{Pr}_{0.65}(\text{Ca}_{0.75}\text{Sr}_{0.25})_{0.35}\text{MnO}_3$ structure at 75 K. [13]

in Fig. 2-11(a)). [12] From the result, one can see the appearance of the sharp resistivity jumps occurs when the width of the LPCMO wires is reduced to $1.6 \mu\text{m}$ while wider width wires do not show noticeable resistivity jumps. This result strongly suggests that the sharp resistivity jumps are likely the consequences of the reduction of conducting channels down to a single pathway, i.e., spatial confinement. Wu and Mitchell also observed sudden resistive jumps during the sweeping of the magnetic field in mesoscopic $\text{Pr}_{0.65}(\text{Ca}_{0.75}\text{Sr}_{0.25})_{0.35}\text{MnO}_3$ structures (shown in Fig. 2-11(b)). [13] It should be noted that the magnetization curves do not show any discrete jumps while the resistance curve shows sudden jumps during the field sweeping. They concluded that the jumps in the resistance vs. magnetic field curves originate from the magnetic-field-induced creation and annihilation of single or a few conducting filaments without a significant increase in phase fraction.

Fig. 2-12 shows magnetic force microscopy (MFM) images of electronic phase domain change and its corresponding resistivity as a function of temperature in wide thin films of $\text{La}_{0.33}\text{Pr}_{0.34}\text{Ca}_{0.33}\text{MnO}_3$. [10] As shown in the Fig. 2-12, during the cooling process, the MFM (dark color) domains grow within the COI/CDI (bright color) background and merge at the metal-to-insulator transition temperature T_{P1} . One can see the resistivity steeply decrease during this MFM 'merging' process directly demonstrating that percolation plays an important role in the resistivity of EPS manganites. By contrast, upon warming, the MFM domain size remains unchanged until near the transition temperature and the MFM

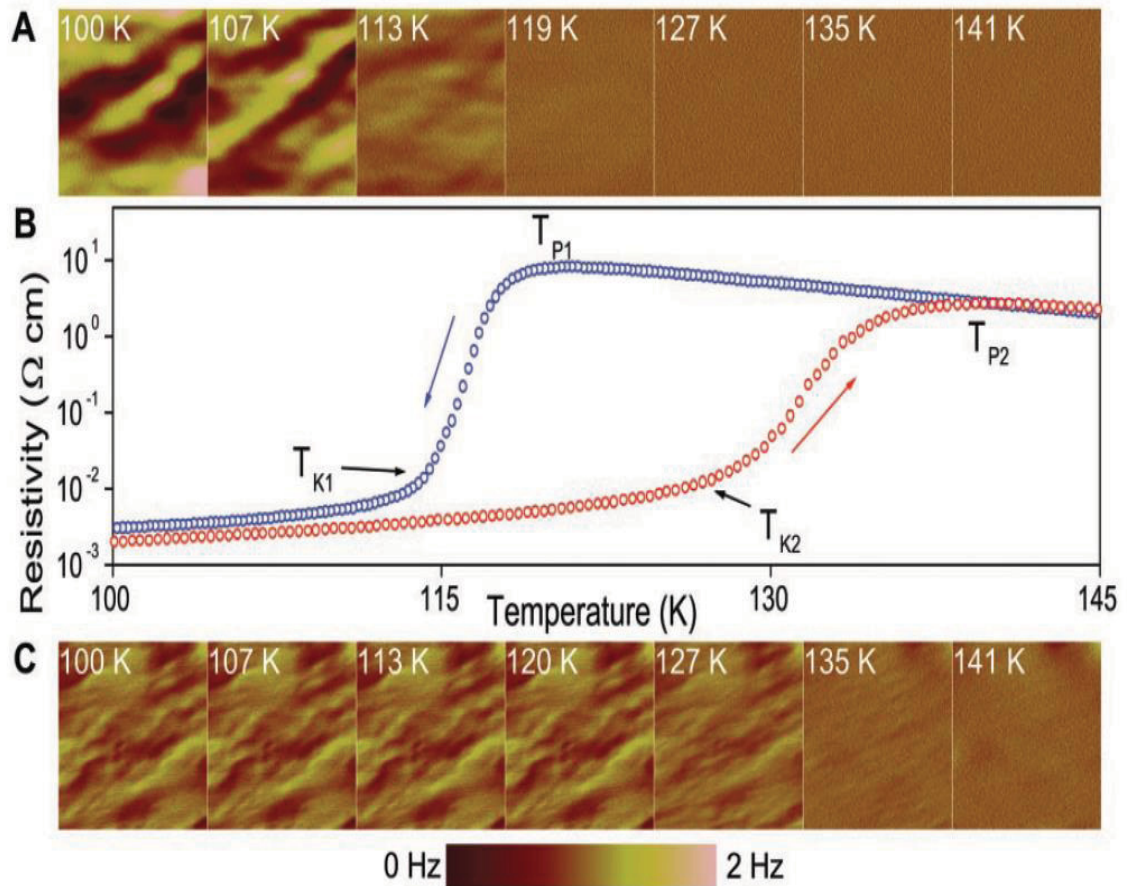


Figure 2.12: The temperature-dependent MFM image (a) for cooling process (scanned area: 6 by 6 micrometer) and (c) for warming process (scanned area: 7.5 by 7.5 micrometer). The corresponding resistance vs. temperature is shown for cooling (blue) and warming (red) processes, respectively. [10]

domains disappear at T_{P2} . Note that T_{P2} is higher than T_{P1} . This explains the thermal hysteresis of the LPCMO system. Furthermore, it is notable that some FMM domains are observed even well above T_{P2} , indicating magnetic inhomogeneity of the system even at high temperatures. [10]

In summary; as discussed in the above examples (as well as other research on spatially confined LPCMO systems), $(\text{La}_{1-x}\text{Pr}_x)_{1-y}\text{Ca}_y\text{MnO}_3$ thin films with $y = 0.3 \sim 0.35$ and $x = 0.5 \sim 0.6$ have shown noteworthy magneto-transport phenomena when the sample's lateral dimension is reduced to few μm . These fascinating confinement-based phenomena occur because these LPCMO systems possess large scale electronic phase separation with the sizes of the FMM and COI electronic phase domains also being on the order of micrometers. [8–10] Furthermore, samples (LPCMO films) with such lateral sizes (few micrometers) are straightforward to synthesize using standard photo-lithography and chemical wet-etching techniques. These characteristics of LPCMO described make them ideal systems for experimentally investigating certain novel magneto-transport properties that are governed by the effect of spatial confinement. In this thesis, I have specifically chosen the composition $\text{La}_{0.3}\text{Pr}_{0.4}\text{Ca}_{0.3}\text{MnO}_3$ for my investigations.

Chapter 3

Experimental Techniques

In this chapter, the experimental techniques for sample preparation and characterization of the resistivity of the samples in this thesis will be described. First, a solid state reaction method for synthesizing the sputtering target (bulk La-Pr-Ca-Mn-O system) is discussed. Then, the film deposition process by using the off-axis D. C. magnetron sputtering system is described. Next, the fabrication of spatial confined LPCMO systems by photo-lithography and chemical wet-etching process is explained. Finally, the general features of the transport measurement systems are introduced. Note that since the research in different chapters in this thesis uses different measurement techniques, specific methods and conditions for a certain subject will be re-discussed in each chapter.

3.1 Polycrystalline LPCMO bulk sputtering target

Prior to fabricating spatially confined thin films, it is necessary to prepare a sputtering target with good quality in order to deposit thin films. For the target fabrication, polycrystalline $\text{La}_{0.3}\text{Pr}_{0.4}\text{Ca}_{0.3}\text{MnO}_3$ (LPCMO) bulk samples are prepared using a standard solid state reaction method. In order to obtain the stoichiometry of LPCMO, La_2O_3 (Alfa Aesar 99.999 % purity), Pr_6O_{11} (Alfa Aesar 99.996 % purity), CaCO_3 (Anderson Physics Laboratory Inc. 99.995 % purity) and MnO_2 (Aldrich Chemical 99.99 % purity) powders are dried in an 80°C oven (Fisher Isotemp Oven) for more than 24 hours to remove undesirable moisture. Then precise amounts of each powder, according to the composition, are mixed and pressed into pellets. Depending on the purpose of the sample, different diameters of the pellets are used; 1/4" for testing bulk samples (1 ~ 2 g) and 1" for sputtering target (7 ~ 9 g), respectively. The pressed pellets are then calcined at 1100°C for 24 hours in air. The resulting samples are pulverized, pressed and sintered at 1200°C for 24 hours. This process is repeated once more to obtain a homogeneous chemical state of the samples. As the final process, the samples are pulverized, pressed and sintered at 1200°C for 48 hours. The electric transport properties of the prepared testing samples (1/4" pellets-cut into rectangular shape) are measured with standard four-point probe method to check the quality of the sample. After the characterization, the results are compared to previous studies (or to other researcher's

results). If the results agree with others (e.g. T_{MIT} within 5 %), the sputtering target is prepared in the same process and placed into D. C. sputtering system.

3.2 Thin film growth

The fabrication of thin films of the LPCMO system is achieved by using a D. C. off-axis magnetron sputtering system which is one of the most common film deposition techniques on single crystal substrates. A schematic diagram of the sputtering process and pictures of the sputtering system are shown in Fig. 3-1. The basic process of sputtering is as follows: In an argon-oxygen mixture filled chamber, when a constant voltage is applied between the target (cathode) and the substrate (anode), it ionizes the Ar gas and creates a plasma. Then, the energetic argon ions (Ar^+) accelerate towards a prepared sputtering target. The collisions of these Ar ions onto the target eject target atoms (LPCMO) and secondary electrons into the chamber space. These ejected atoms travel the distance to the substrate and sit on the heated substrate. As more target atoms sit on the heated substrate, they begin to bind to each other and form a tightly bound atomic layer and multiple layers of atomic layers are deposited at a rate depending on the sputtering conditions such as time, acceleration voltage, substrate temperature, etc. In our D. C. magnetron sputtering system, magnets are placed behind the target. These magnets induce a strong magnetic field near the target area and the field causes the secondary electrons to spiral along magnetic flux lines which increases the traveling distance of the electrons. This effect eventually increases the probability of collision between the electrons and Ar atoms near the target. As a result it generates a dense plasma which increases the efficiency of the sputtering process. An illustration of the sputtering process is shown in Fig. 3-1(c). Furthermore, the O_2 gas in the chamber acts as a reactive gas during the sputtering process which aids in maintaining the stoichiometry of the LPCMO thin films.

Before depositing the LPCMO films, a test film is first deposited in order to calibrate the deposition rate and also to check the quality of the film. The thicknesses of the films were characterized by a profilometer (Alphastep IQ) and atomic force microscopy (AFM, Asylum). The deposition rate was found to be 1.46 ± 0.15 nm/min. The thin films studied in this thesis were deposited on commercial (100)-oriented one-side polished SrTiO_3 (STO) and LaAlO_3 (LAO) substrates. Prior to the deposition of LPCMO thin films, the substrates were carefully cut and cleaned. Note that the substrates were cleaned with heated ($\sim 70^\circ\text{C}$) detergent (Alconox, Detergent 8) and an ultrasonic bath (Branson, B-42H). The cleaned substrates were then attached on a nickel plate with silver paste (Ted Pella, Inc., Leitsilber 200 silver paint) and dried in air for more than 3 hours. Before placing the prepared substrates into the sputtering system, inside the sputtering chamber was cleaned to get rid of any undesirable particles. Then, the substrates were placed into the sputtering chamber and vacuumed down to $\sim 3.0 \times 10^{-7}$ Torr. The LPCMO thin films were deposited at a temperature of 750°C in an oxygen-argon mixture (Ar: 20 mTorr, O_2 : 100 mTorr) environ-

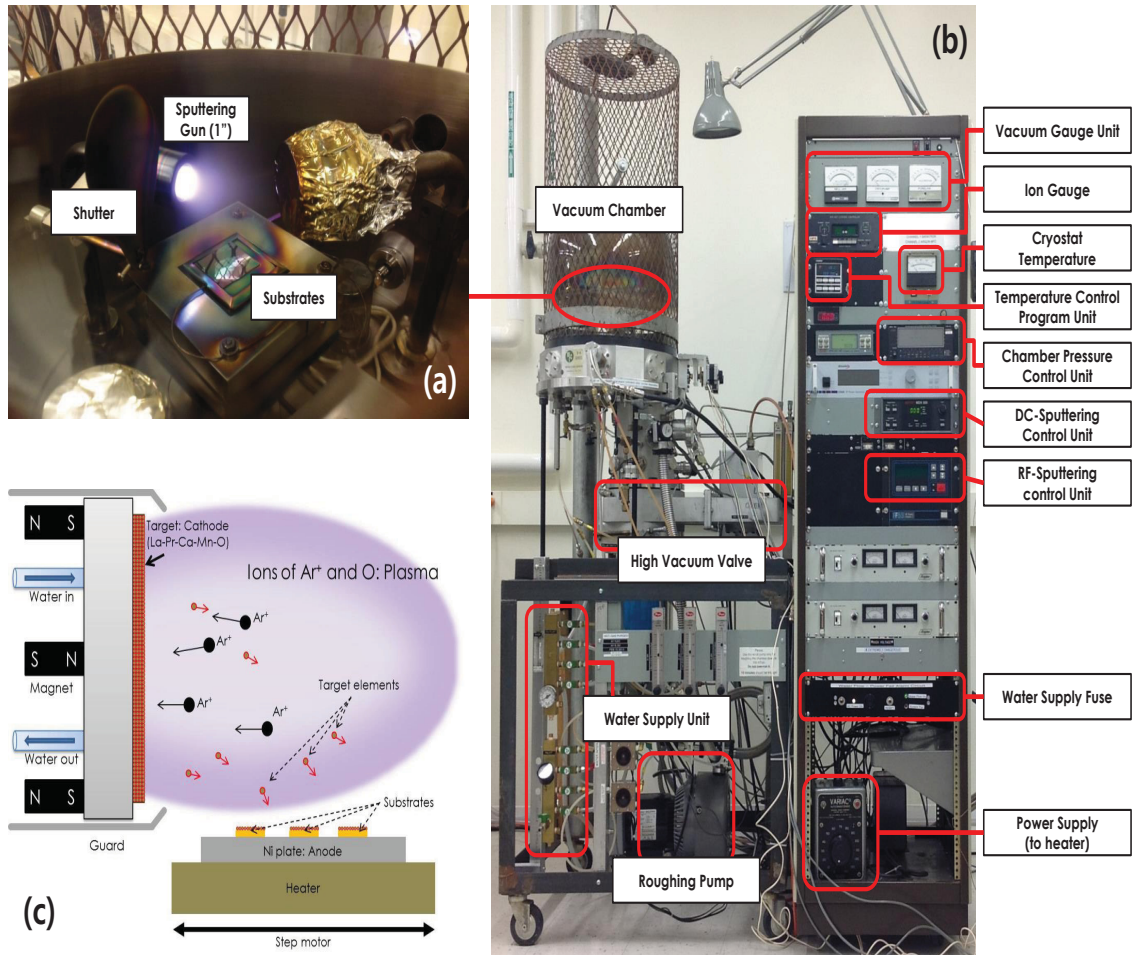


Figure 3.1: (a) A picture of the inside of the sputtering chamber: For LPCMO thin film deposition, a 1 inch magnetron sputtering gun is used where the shutter is installed to control (on/off) the sputtering. (b) A picture of the sputtering system: the system consists of a vacuum chamber, vacuum pump unit, water supply, and control station. (c) An illustration of off axis D. C. magnetron sputtering process: As Ar ions accelerate toward the sputtering target, the collisions of these Ar ions onto the target eject target atoms (LPCMO). Then the ejected atoms sit layer by layer on the heated substrate.

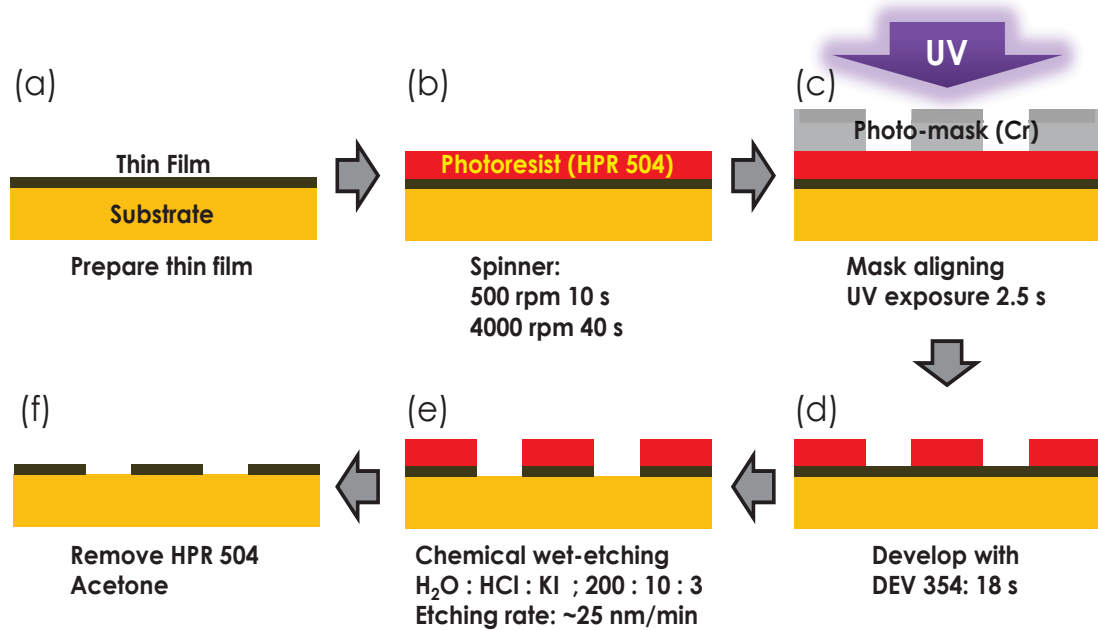


Figure 3.2: Procedure of photo-lithography and chemical wet-etching: (a) Sample preparation and surface cleaning. (b) Photoresist (HPR 504) spreading. (c) Mask aligning and UV exposure. (d) Development of the pattern (DEV 354). (e) Chemical wet-etching process. (f) Cleaning the photoresist.

ment. Furthermore, the plate with substrates was rotated ($\pm 10^\circ$) during the deposition in order to get uniform thickness of LPCMO films. The deposition time was adjusted to have the desired thicknesses of the films. After the deposition, the chamber was filled with pure oxygen at atmospheric pressure, then the films were cooled down to 650°C at a rate of $3^\circ\text{C}/\text{min}$ and annealed for 3 hours at this temperature. The films were then cooled down to room temperature at a rate of $20^\circ\text{C}/\text{min}$.

3.3 Device fabrication: photo-lithography and chemical wet-etching

Conventional photo-lithography with chemical wet-etching enables us to fabricate micrometer lateral dimensions of thin films. Fabricating micrometre-width bridge is an important part of the spatially confined sample preparation. The entire process of the photo-lithography was done in the Nanofab (University of Alberta). In order to obtain a desirable geometry of the bridge, the photo-mask patterns were designed by using L-edit program and printed with Cr coating on a quartz glass.

The photo-lithography process is the following (shown in Fig. 3-2): (1) Prepare the sample (clean the surface of the thin films). (2) Place the cleaned sample on a spinner (Solitec photoresist spinner station) and put a drop of photo-resist (HPR 504) on the surface of

the film then run the spinner (initial spin 500 rpm for 10 s, main spin at 4,000 rpm for 30 s) in order to have uniform spread of the photo-resist on the surface. After the spreading process, the photo-resist covered sample should be baked in a vacuum oven at 120° for 90 s. (3) Align the sample under a photo-mask and press the mask so that no light leaks when the sample is exposed to ultra-violet (UV) light. Then, UV light is turned on for 2.5 s. (4) This was followed by developing (photo-resist melting process) the sample in a developer (DEV 354) for 18 s. When the development was done, the pattern's quality was checked by optical-microscopy. (5) The developed sample is immersed in chemical solution to remove undesirable parts of the LPCMO pattern (chemical wet-etching process). The optimum etching solution for the manganite was found to be HCl + H₂O + KI with a ratio of 10 : 200 : 3 that had an etching rate of $\sim 25 \pm 5$ nm/min for LPCMO thin films. When the wet-etching was done, the sample was immersed into water to remove the solution. In order to confirm the removal of the undesirable part of the pattern, the resistance of the etched part was measured ($> 2 \times 10^9 \Omega$). Also, the pattern was carefully checked with an optical microscope. (6) Finally, if the pattern had no problem, the remaining photo-resist was removed by acetone.

3.4 Transport measurements

The magneto-transport measurements of the prepared samples were achieved by a home-built anisotropic magneto-resistance (AMR) system. A picture of the AMR system is shown in Fig. 3-3. The AMR system consisted of a vacuum unit, cryogenics, measurement unit and magnet unit. Each unit is controlled and monitored by a PC with home built LabView drivers. To help the understanding of the system, a schematic and block diagram is shown in Fig. 3-4. Prior to mounting the samples, the electrodes were sputtered from R. F. sputtering with a pure Ag target (2" disk). Then, the wires with indium coated ends were connected onto the electrodes and samples were loaded into the system. The samples were attached on the oxygen-free copper with a grease (Apiezone N-type) for good thermal conduction. Note that thin kapton film is placed between the sample and the copper block for electrical isolation (with good thermal conduction). Then, the system was closed, sealed and vacuumed by using a turbo pump (Varian DS202). In order to remove undesirable molecules in the system, the pumping was run until the pressure is on the order of 10^{-6} Torr. Then, the cryogenic (Sumimoto RDK-408D2 and CSW 71) unit was turned on to cool down the system. The temperature of the sample is controlled by a temperature controller (LS 332 controller) that is connected to a heater (Vishay type 301470) and a thermometer (Cernox cx-1050-AA). The temperature range of the transport measurement was 10 - 300 K.

The measurement unit of the system consist of two nanovoltmeters (Keithley 2182), two AC/DC current sources (Keithley 6221) and two sourcemeters (Keithley 2410) so that 4 samples can be characterized at the same time. The configuration of the 4 point probe

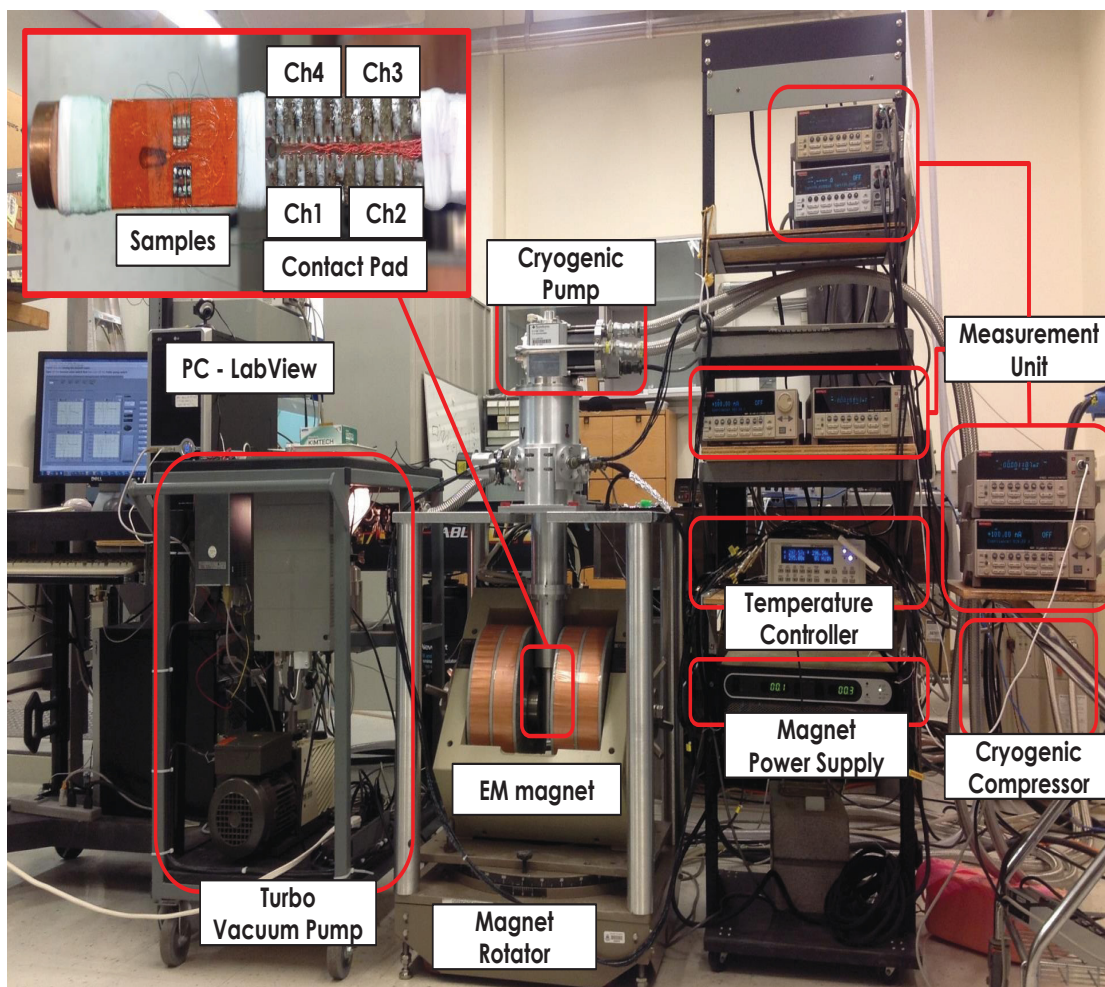


Figure 3.3: A picture of anisotropic magneto-resistance (AMR) system that is consisted of vacuum unit, cryogenics, measurement unit and magnet unit, respectively. The inset of the picture shows inside of the AMR system where the samples are placed.

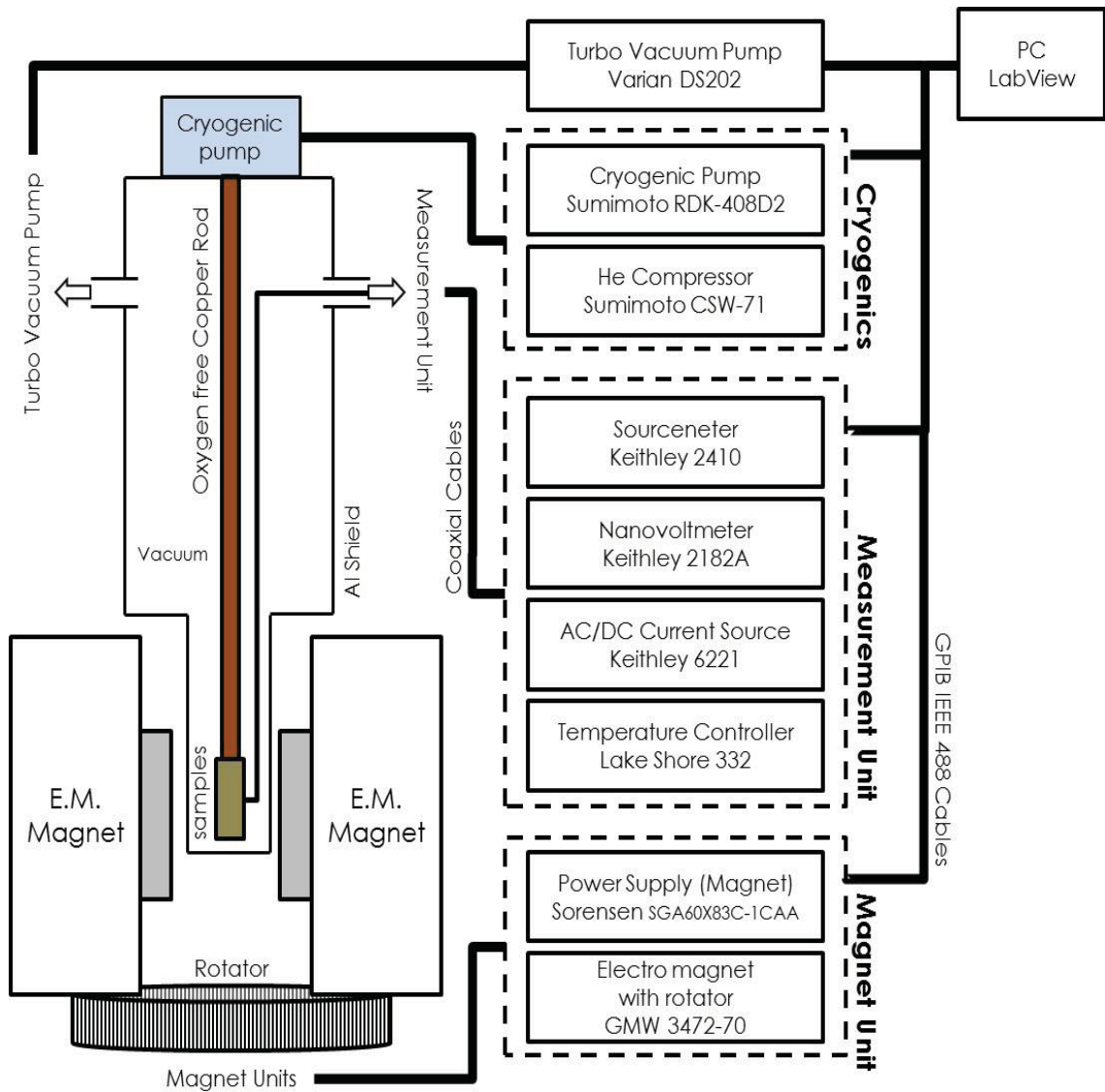


Figure 3.4: A schematic and block diagram of transport measurement system.

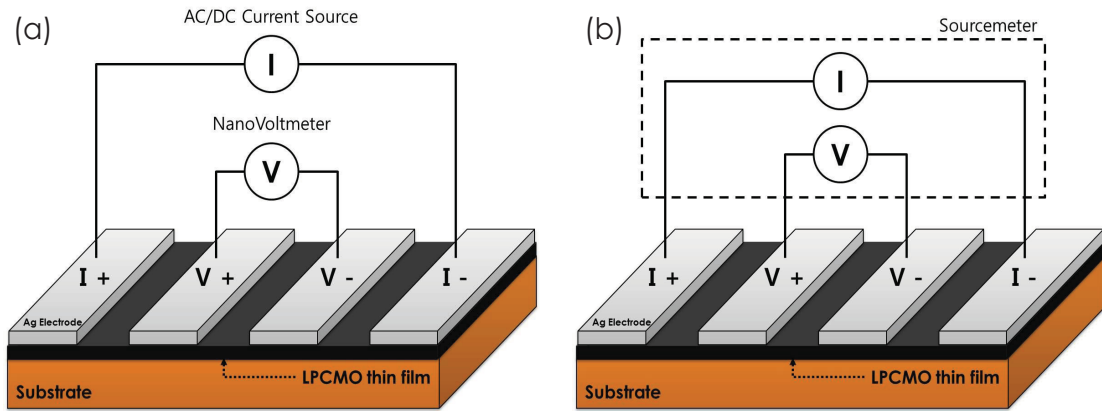


Figure 3.5: The 4 point probe method for (a) AC/DC current source and nanovoltmeter combination and (b) sourcemeter unit.

method used to measure the resistance of each sample is shown in Fig. 3-5. Also, in order to minimize measurement noise, all the wires are properly shielded and separated from vibration sources.

In the following chapters, different types of transport properties are carried out; resistance vs. magnetic field, resistance vs. field angle and resistance vs time. Detailed measurement conditions will be further described in each chapter.

Chapter 4

Re-entrant Low-field Magneto-resistance in LPCMO Film due to Spatial Confinement

4.1 Introduction

In many manganites, the co-existence of phases (such as FMM, COI, etc.) is believed to play a very prominent role in determining the material's magneto-transport properties, including the existence of colossal magnetoresistance (CMR). [9, 13, 34] Keep in mind the fact that the CMR effects in manganites often require high magnetic field of about few (or even tens) Tesla (e.g., > 3 T is required to achieve significant CMR). This is one of the reasons that the development of devices using CMR material (manganite) has been delayed. In this chapter of the thesis, we investigate the influence of the spatial confinement-induced jumps in the temperature dependence of the resistivity on the low field colossal magneto-resistance (LF-CMR), a parameter that is of particular relevance in device applications such as nonvolatile memory, electronic sensors, etc. [3, 19, 35–39] The LF-CMR of a confined LPCMO system has not been previously reported and may be different from a 'wide' film. As discussed in Chapter 2, the electronic phase separation (EPS) is particularly large-scale in $(\text{La}_{1-y}\text{Pr}_y)_{1-x}\text{Ca}_x\text{MnO}_3$ (LPCMO) [8, 10, 40, 41] where the size of the domains can be on the order of μm below the metal-insulator transition temperature T_{MIT} . Consequently, it has been found that sudden jumps in the resistivity (below the metal-insulator transition temperature) exist when the temperature or magnetic field is changed slightly. [12, 14, 42, 43] These jumps occur in a μm wide sample because the transport pathway may contain only a small number of domains, and hence the transition of a single domain from insulating to metallic (or vice versa) can have a very significant effect on the conduction path. The high sensitivity of the resistance jumps to the magnetic field suggests that the spatially confined system may have a very different LF-CMR compared to a wide system. Here, the LF-CMR was investigated in $\text{La}_{0.3}\text{Pr}_{0.4}\text{Ca}_{0.3}\text{MnO}_3$ thin film micro-bridges of $2 \mu\text{m}$ and $25 \mu\text{m}$ in width. The $2 \mu\text{m}$ wide micro-bridge showed confinement-induced resistance

jumps while the 25 μm wide micro-bridge showed smooth changes in the resistance as temperature/magnetic field was changed. A broad single maximum is observed in a field of 1.08 T in the temperature dependence of the MR for both films. However, at lower magnetic fields two separate maxima appear in the temperature dependence of the MR for the spatially confined 2 μm wide micro-bridge. The maximum at a lower temperature has a much weaker dependence on magnetic field than the one at higher temperatures close to T_{MIT} .

4.2 Experimental details

The studies were carried out on two $\text{La}_{0.3}\text{Pr}_{0.4}\text{Ca}_{0.3}\text{MnO}_3$ films of thickness 45 nm deposited on SrTiO_3 (STO) substrates by direct current magnetron sputtering, and patterned as indicated in the insets of Fig. 4-1. The micro-bridge parts of the film are 2 μm by 2 μm and 25 μm by 25 μm in Fig. 4-1(a) and Fig. 4-1(b), respectively, and because of their small areas compared to the rest of the films, are expected to contribute significantly to the transport properties in both films. For example, from geometrical considerations alone (i.e., assuming a uniform resistivity throughout the film), the resistance ratios between the microbridge and the rest of the film (between the voltage contacts) are $\sim 25:1$ and $\sim 15:1$ for the 2 $\mu\text{m} \times 2 \mu\text{m}$ and 25 $\mu\text{m} \times 25 \mu\text{m}$ bridges, respectively. The square geometry is chosen so that both films have very similar resistances at room temperature, as indicated in Fig. 4-1. The appropriate geometries were obtained by using standard photolithography and a manganite wet-etching solution (potassium iodide (KI) + hydrogen chloride (HCl) + deionized water (H_2O)) to pattern the LPCMO films, then using a suitable wet-etchant to remove the irrelevant parts of the manganite film. Silver was used for electrical contacts in a four point configuration (outside of the regions shown in the insets in Fig. 4-1). A Keithley 6221 DC/AC current source was used to provide a constant current of 1 μA to the film, the voltage was measured with a Keithley 2182A nanovoltmeter, and the resistance R subsequently calculated (also, see Chapter 3 for details). Homemade LABVIEW programs were used to control the temperature, set the magnetic field, calculate and record the resistances, etc.

4.3 Results and discussion

Fig. 4-1 shows the temperature dependence of the resistance of both LPCMO micro-bridges in various applied magnetic fields. After first field-cooling the sample to 10 K, the data were collected upon warming at a rate of 3 K/min and the current and magnetic field applied in the directions shown in the insets in Fig. 4-1(a) and (b). In the narrow, i.e. 2 μm , bridge, sharp jumps in the resistance are observed between 100 K and 130 K at some fields, as indicated in more detail in Fig. 4-2(a). These jumps are most prominent in the absence of an applied field. With an increasing field, the onset of the jumps moves to higher

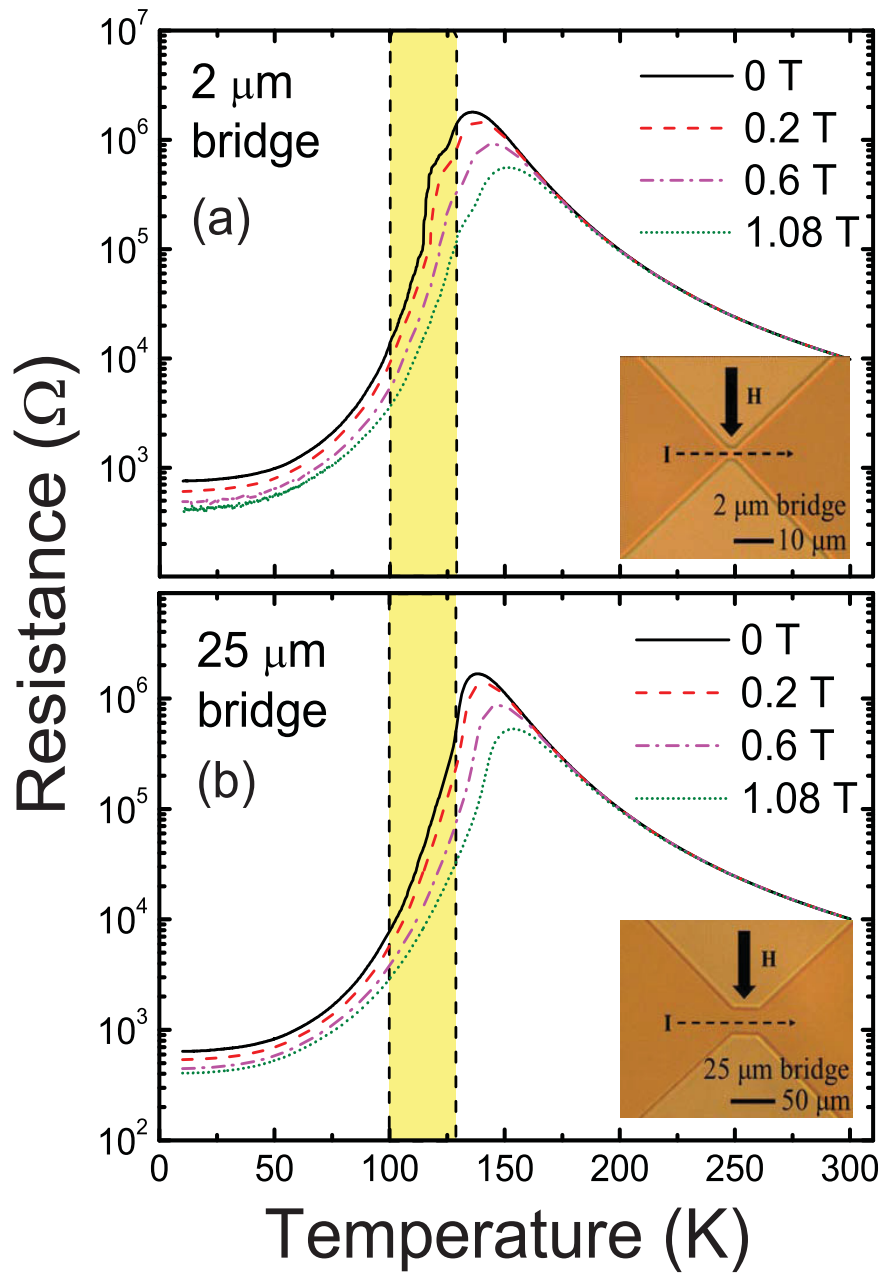


Figure 4.1: Temperature and field dependence of the resistance in the (a) 2 micrometer and the (b) 25 micrometer width micro-bridges during warming. The shaded regions are shown expanded in Fig. 4-2. The insets show pictures of the 2 by 2 and 25 by 25 micro-bridges with the directions of the current (I) and magnetic field (H) indicated.)

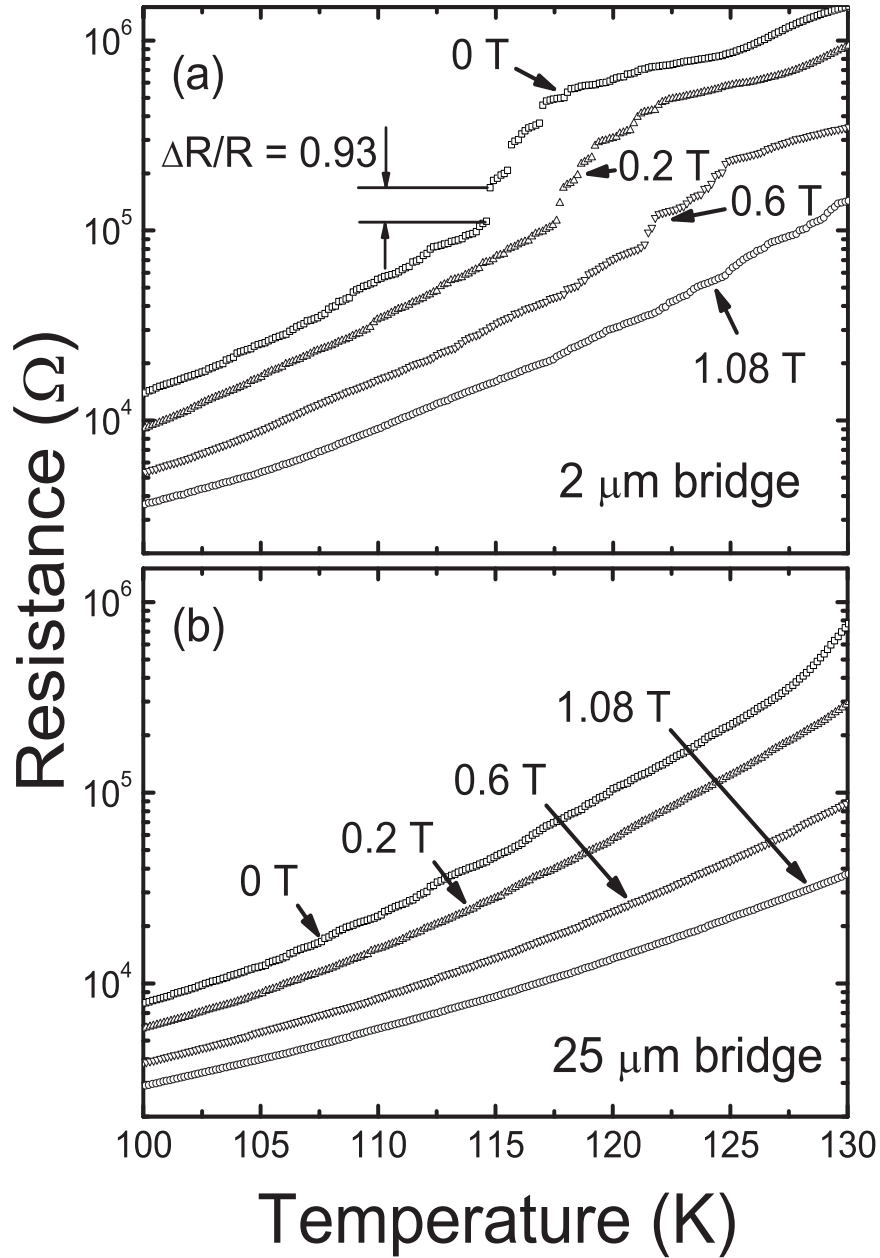


Figure 4.2: Temperature and field dependence of the resistance in the (a) 2 micrometer and the (b) 25 micrometer micro-bridges during warming process. These plots are an expansion of Fig. 4-1 (the shaded regions) from 100 K to 130 K.

temperatures and the size of the jumps decreases (at fields larger than 1 T, they are barely visible). As indicated in Fig. 4-2(b), in the wide, i.e. 25 μm , bridge, these jumps are very suppressed, although some evidence for them might still exist at the lower fields.

By considering the models put forth by other researchers who have studied spatially confined manganite bridges (width of a few micrometers to hundreds nanometers), [3,9,11–13,34,42] we suggest the following qualitative mechanisms for the behaviour of resistance vs. temperature, $R(T)$, profile below T_{MIT} observed in Fig. 4-1 and Fig. 4-2. First, consider the $H = 0$ T data for the 2 μm bridge. At low temperatures, e.g., 10 K, the LPCMO film is made up of an electronically phase-separated state consisting of FMM and COI/CDI domains, and there is significant percolation between the FMM domains. Upon warming from 10 K, the volume fraction of the FMM domains decreases and the resistance of the system increases. The sharp jumps in $R(T)$ occur when the metallic and insulating domain sizes are comparable to the width of the bridge, i.e., μm . Here, the conduction pathway is dominated by a small number of metallic and insulating domains, and hence the loss of percolation between two adjacent FMM domains can have a large, and sudden, effect on the resistance. Upon further warming, the FMM domains shrink in size until they are much smaller than the width of the bridge, and a local transition of a metallic region into insulating does not have a dramatic effect on the resistance; hence, the jumps are no longer apparent. As noted above, the onset of the jumps shifts to higher temperature as the magnetic field is increased. This is consistent with the fact that the FMM domains and the relative volume of metallic to insulating regions are larger in a higher magnetic field, and hence a higher temperature must be reached before the width of the sample becomes comparable with the size of the metallic/insulating domains. At high fields (e.g., 1.08 T), the jumps are barely visible, implying that such fields prevent the formation of metallic/insulating domains of μm size. The lack of jumps in the 25 μm bridge implies that we never reach the regime such that we can confine a small number of metallic/insulating domains within the sample, and its transport properties should approach those of a normal wide film.

The existence of the large jumps in $R(T)$ at low fields and their high sensitivity to the magnitude of the field introduces additional characteristics into the magnetoresistance of the narrow bridge. The magnetoresistance is defined by

$$MR = \frac{[R(0) - R(H)]}{R(0)}, \quad (4.1)$$

where $R(0)$ and $R(H)$ are the resistance at zero field and non-zero field, respectively. This is illustrated in Fig. 4-3, which shows the temperature dependence of the MR in the 2 μm and 25 μm bridges. In the 25 μm film (Fig. 4-3(b)), the MR peaks near the T_{MIT} (137 K); such behaviour is typical of wide films. [4,44]

However, in the 2 μm bridge, a second peak of $MR(T)$ appears (at ~ 117 K in Fig. 4-2(b) shaded region), which is particularly clear at the low fields (0.2 T). In other words,

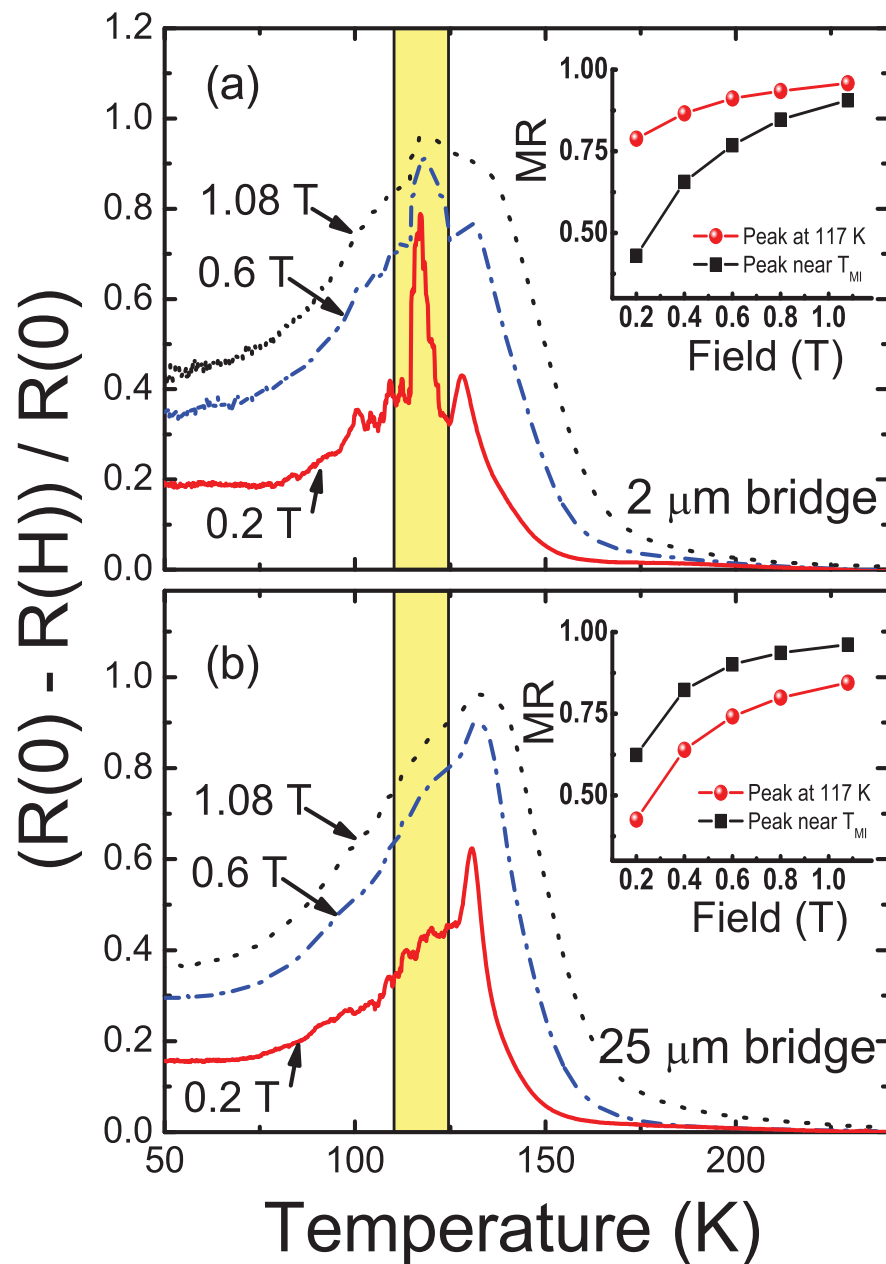


Figure 4.3: Temperature and field dependence of the magnetoresistance in the (a) 2 micrometer and the (b) 25 micrometer micro-bridges during warming. The shaded regions are the temperature range where a secondary peak appears for a spatially confined manganite system. The insets show the dependence of the MR at 117 K and near metal-insulator transition temperature.

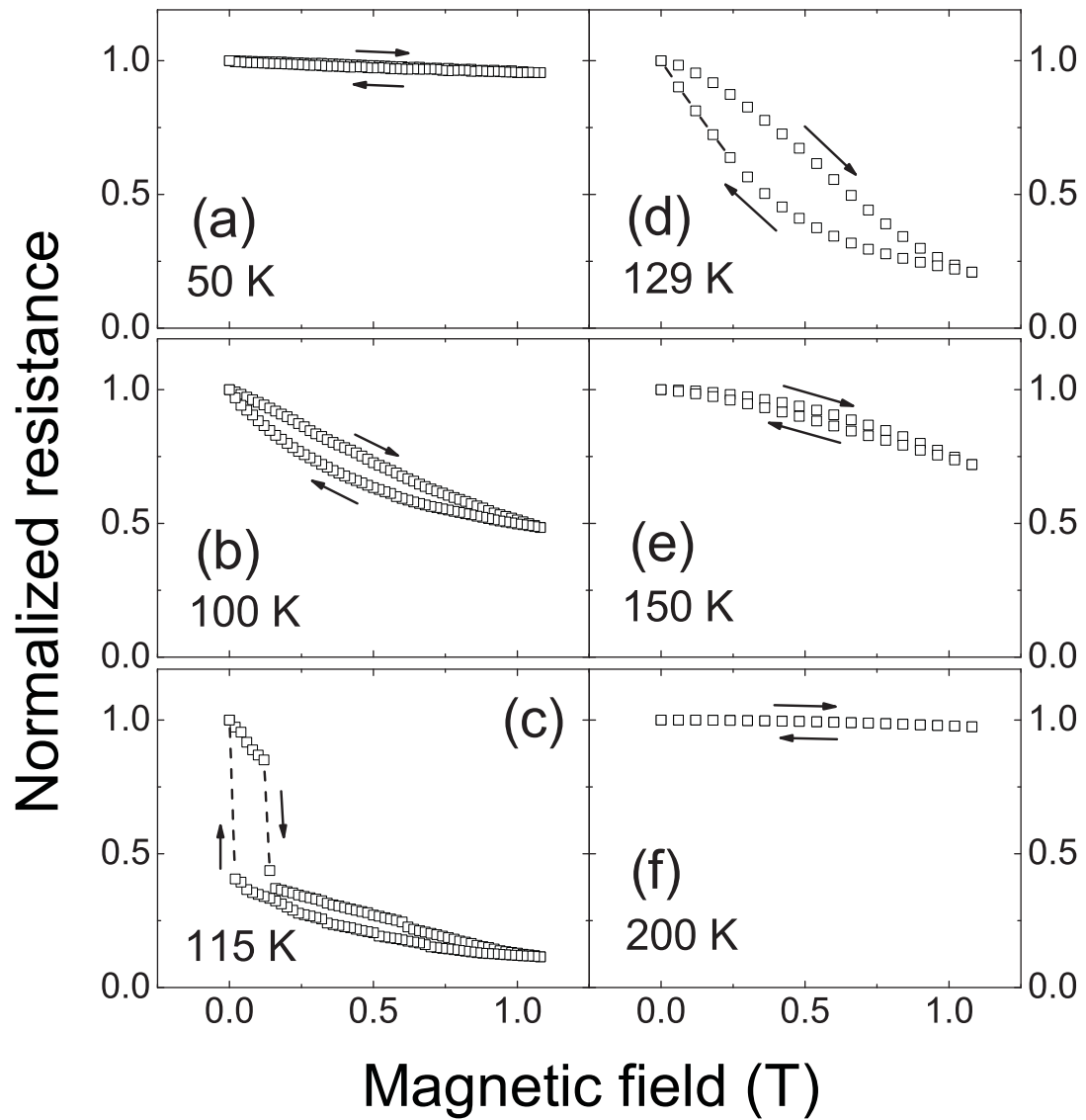


Figure 4.4: The plots (a) to (f) show the normalized resistance versus the magnetic field of 2 micrometer width bridge. The arrows indicate the direction of the field sweep, the field is first increased to 1.08 T and then subsequently decreased to 0 T.

the significant changes in the shape of $R(T)$ with small changes in the external magnetic field produces a MR enhanced region below the T_{MIT} in the $2\ \mu\text{m}$ bridge. Furthermore, this lower temperature MR peak is more robust with field than the MR peak near the T_{MIT} . For example, when the external magnetic field is reduced from 1.08 T to 0.2 T, the MR at the higher temperature peak is reduced by $\sim 47\%$ while the MR at the lower temperature peak is reduced by only $\sim 16\%$ (see the insets in Fig. 4-3). Note also that the low field (0.2 T) MR at the low temperature peak remains large with a value of ~ 0.8 in the $2\ \mu\text{m}$ bridge, while in $25\ \mu\text{m}$ bridge, the value is only ~ 0.4 .

We point out that some randomness is expected in the jumping events since the domains do not have exactly the same configuration from one measurement to the next. Nevertheless, we have measured the $R(T)$ curves several times and verified that the behaviour is very similar each time. Hence, the results in Fig. 4-3 are quite reproducible.

As we shall discuss below, the existence of spatial confinement in the $2\ \mu\text{m}$ bridge also produces interesting additional features in the magnetic field dependence of the resistance, i.e., $R(H)$, and the associated hysteresis loops. The normalized $R(H)$ at various temperatures is shown in Fig. 4-4(a) to (f) for the $2\ \mu\text{m}$ bridge (normalized to the value of R for $H = 0\ \text{T}$); at each temperature, the field is first increased to 1.08 T and then subsequently decreased to 0 T with a rate of 2 mT/s. Notice there is significant hysteresis between the upward and downward scanning directions at most temperatures below 150 K. The shapes of the hysteresis loops in the $2\ \mu\text{m}$ bridge fall into two general categories: in one case, such as in Fig. 4-4(b) and Fig. 4-4(d), the hysteresis loop is smooth. However, at some temperatures such as that shown in Fig. 4-4(c), there are sharp and large changes in R during the field scan superimposed upon the smooth hysteresis loop. In contrast to the $2\ \mu\text{m}$ bridge, we note that in the $25\ \mu\text{m}$ bridge, the hysteresis loops are all of the former, i.e. smooth, type. Clearly, the appearance of the jumps in $R(H)$ in the $2\ \mu\text{m}$ bridge is due to the effects of spatial confinement. For example, the sharp decrease in the resistance at $\sim 0.2\ \text{T}$ for 115 K (Fig. 4-4(c)) upon increasing field indicates that under these conditions, the bridge contains only a few insulating/metallic domains; here, the conversion of a local insulating region into a FMM region in the bridge dramatically enhances the percolation within the bridge and produces a large sudden decrease in the resistance. During the downward sweep of the field, the reverse takes place albeit at a lower field, i.e. it is the single disconnection of the percolation path within the bridge that produces the sharp increase of the resistance. We also point out that with increasing temperature around 115 K, the ‘‘jump field’’ also increases: for example, while the resistance sharply decreases at $\sim 0.2\ \text{T}$ for 115 K, the drops take place at 0.3 T for 117 K, and at 0.86 T for 119 K (not shown), consistent with the decrease of the FMM volume and domain size with increasing T.

The areas of the hysteresis loops are plotted versus temperature in Fig. 4-5 for both the $2\ \mu\text{m}$ and the $25\ \mu\text{m}$ bridges. In the $25\ \mu\text{m}$ bridge, there is a single peak in the normalized area at $\sim 130\ \text{K}$, near the T_{MIT} . This is consistent with the fact that the phase competition

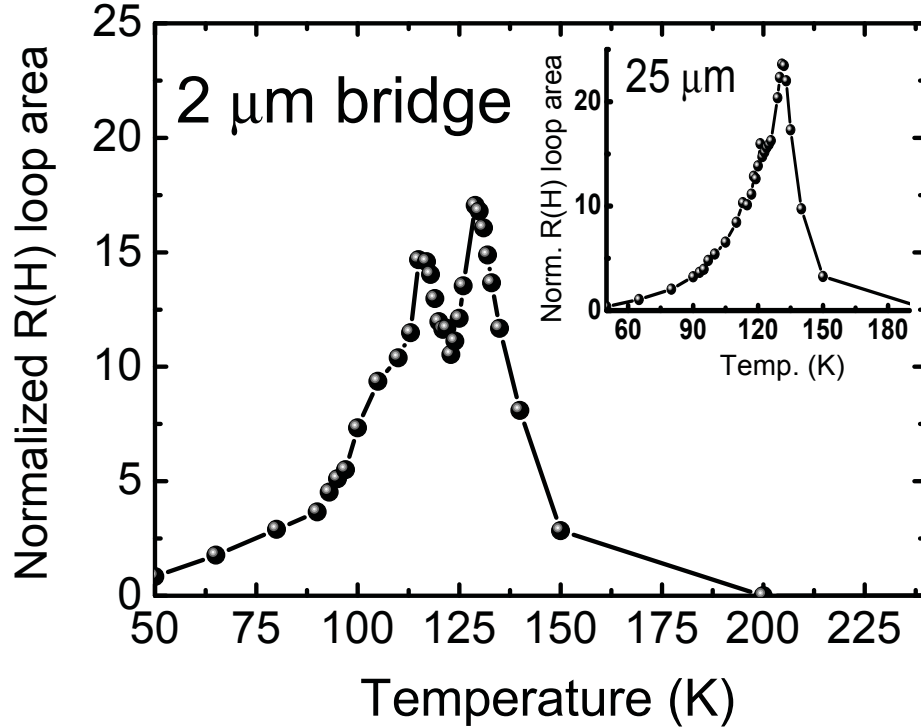


Figure 4.5: The plot shows the area of the $R(H)$ loop versus temperature in the 2 micrometer and (inset) 25 micrometer micro-bridges.

in this sample is the most prominent near the T_{MIT} , [13, 45, 46] and that the size of the (normalized) hysteresis loop is a measure of the phase competition within the system. (The dominant phases are FMM and COI at 50 K and 200 K, respectively.) Notably, the spatial confinement in the 2 μm bridge produces a second peak in the normalized area (occurring at ~ 115 K), as shown in Fig. 4-5. These two peaks are located in the same temperature range as the peaks in the temperature dependence of the MR on temperature (see Fig. 4-3).

4.4 Conclusions

In conclusion, we find that the sudden jumps in the temperature dependence of the resistance that appear in a spatially confined LPCMO 2 μm micro-bridge produces additional features in its magnetoresistance. Two peaks are seen in the temperature dependence of the magnetoresistance as well as the temperature dependence of the area of the hysteresis loops that exist in an isothermal magnetic field scan of the resistance. One of the peaks is close to the metal-insulator transition temperature, as expected for a standard manganese film, while the additional peak occurs at lower temperatures where co-existing metallic and insulating domains have sizes comparable to the spatially confined region. The magnetoresistance of the latter peak is considerably less sensitive to magnetic field than the former. Furthermore, its value at 0.2 T is enhanced by about 100% compared to that of

the 25 μm bridge at the same temperature and field. These results imply that the spatially confined LPCMO thin film requires relatively low field to produce 'colossal' magnetoresistance. Keep in mind that CMR occur at high field (≥ 3 T) in wide manganite thin films. Our results suggest that fabrication of the LF-CMR devices such as nonvolatile memory, magnetic sensors are feasible by using the spatial confinement phenomena.

Chapter 5

Field Dependent Resistive Evolution in Spatially Confined LPCMO Thin Films

5.1 Introduction

In the previous chapter, we have shown the effects of the external magnetic field in a spatially confined LPCMO thin film ($2\ \mu\text{m}$ width). This system exhibited sharp jumps in the resistance with slight modifications of the temperature and magnetic field. These dramatic and sudden resistance switching behaviours are of particular interest for applications such as those related to fast switching sensors. [11, 12, 38, 43, 47–49] Another parameter that may be of interest for better scientific understanding, as well as reliable operation, of spatially confined devices is the long time evolution of the resistance.

It is well established that the isothermal resistance of many manganite films changes with time. In “wide” LPCMO (and also other manganite) films whose smallest lateral dimensions are many orders of magnitude larger than the size of the intrinsic electronic phase domains (e.g., FMM and COI), a smooth evolution of the resistance is seen that changes over the timescale of many minutes. The resistance R in such wide films can increase or decrease with time t depending on the nature of the final state of the system, and this phenomenon mostly occurs at temperatures and/or magnetic fields where phase-competition is taking place within the sample. [2, 50–54]

The time evolution of the resistance of spatially confined manganites are much less studied than in wide films. However, those that do exist show marked contrast with the smooth long-time evolution of the resistance observed in wide films. For example, Wu and Mitchell [13] investigated narrow $\text{Pr}_{0.65}(\text{Ca}_{0.75}\text{Sr}_{0.25})_{0.35}\text{MnO}_3$ thin films, another manganite system with micrometer sized electronically phase separated domains, and showed the existence of sudden giant resistance steps in $R(t)$ which are sporadically distributed on the long-time relaxation of R over a waiting period of approximately an hour. These discrete resistance steps were attributed to the switching of individual conducting filaments to insu-

lating ones within the microbridge. Furthermore, the $R(t)$ of $(\text{La}_{0.5}\text{Pr}_{0.5})_{0.625}\text{Ca}_{0.375}\text{MnO}_3$ microbridges have also been studied by Ward et al. [14, 55] over a small temperature range (80 - 83 K) near the metal-insulator transition temperature T_{MIT} . However, these studies were not focussed on the long-time relaxation of $R(t)$; in fact, a high magnetic field (3.75 T) was applied to ensure that the sample had ferromagnetic alignment, hence suppressing this kind of metastability. (Nevertheless, despite the fact the starting and final average resistances and hence the electronic phase separated volumes are the same, “telegraph noise” was observed. Namely, they saw frequent fluctuations in $R(t)$, often manifesting as jumps between a small number of resistance levels.)

In this chapter, our primary goal is to carry out systematic investigations of the field dependence of the long-time metastability of the resistance of the LPCMO microbridges and to contrast this behaviour with that taking place in LPCMO wide films. Since the electronic states of manganite films are strongly affected by external perturbations such as temperature and magnetic field, [2, 4] a systematic investigation of the response of the phase dynamics to a wide range of these parameters could reveal a deeper understanding on how they modify $R(t)$. Such information is important from both a scientific viewpoint as well as for future applications where one may need to control the time relaxation of resistance in reduced geometries of manganites. Here, we report that at certain temperatures near the metal-insulator transition temperature, sharp jumps in the long-time relaxation of $R(t)$ are found in spatially confined LPCMO thin film microbridges. The sizes and directions of these abrupt changes in resistance can be significantly controlled by the magnitude of the applied magnetic field. These behaviours are described within a phenomenological percolation/de-percolation model.

5.2 Experimental details

The samples used in this chapter are the same samples used in Chapter 4. In this chapter, we shall refer to the $2\ \mu\text{m} \times 2\ \mu\text{m}$ sample as the “2 μm wide” film, “2 μm microbridge”, etc. Analogously, we use the terminology “25 μm wide” film, “25 μm microbridge”, etc. to refer to the LPCMO film containing the $25\ \mu\text{m} \times 25\ \mu\text{m}$ microbridge. The following sequence was used to measure $R(t)$ at a particular temperature and field: Initially the sample was heated up to 300 K (in order to thermally “reset” the system of electronic domains), then cooled down to 10 K in a zero field, and then raised to the temperature of interest. At the relevant temperature, the desired magnetic field was applied and kept unchanged while the resistance was measured as a function of time up to 3,000 seconds.

5.3 Results and discussion

In the electronically phase separated LPCMO system, it is well known that at a fixed magnetic field the metallic phase domains within the sample grow and shrink upon cooling

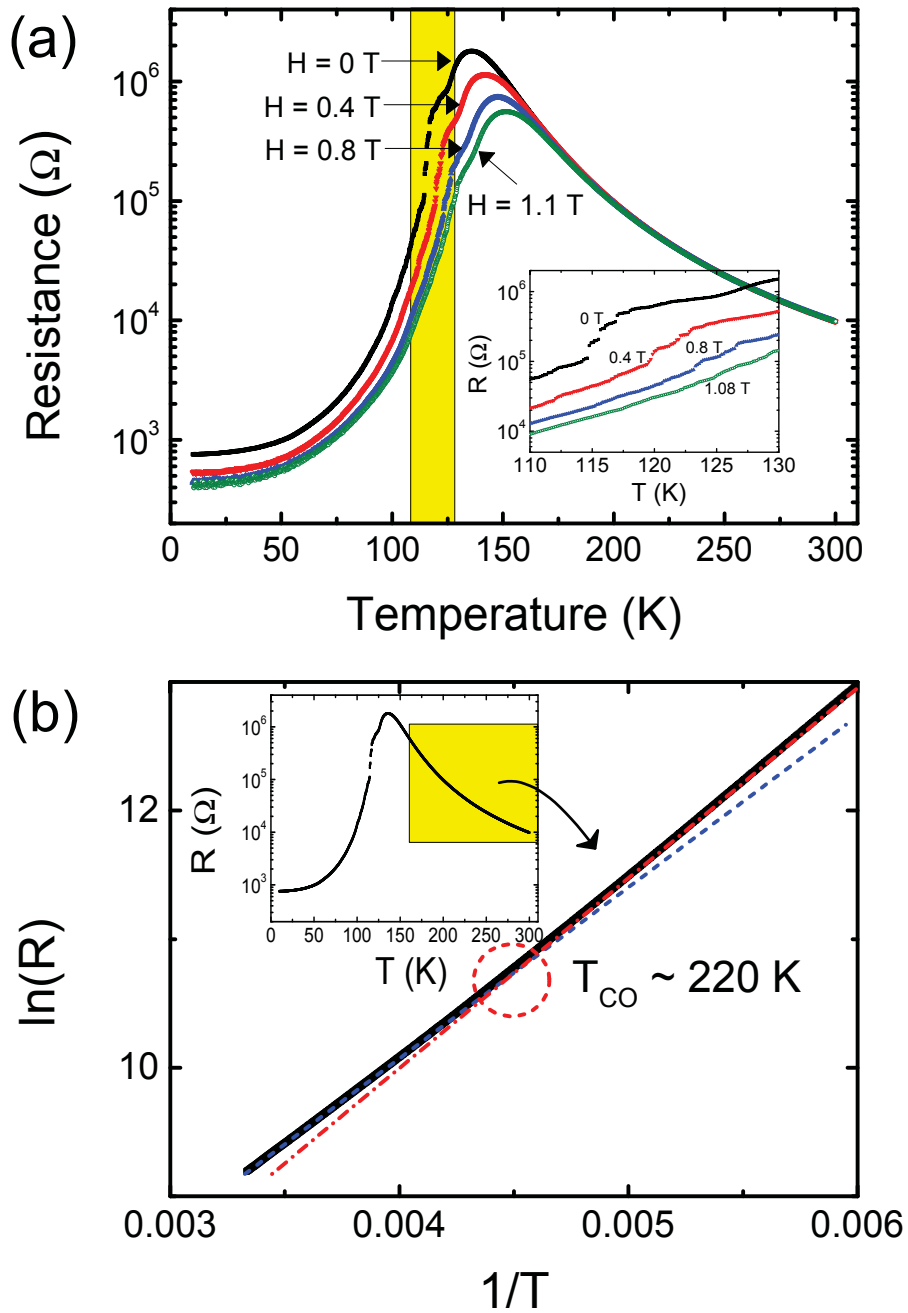


Figure 5.1: (a) Resistance vs. temperature in various external magnetic fields. Note the abrupt changes of the resistance in the temperature range marked in yellow: as discussed in the text, these are signatures of spatial confinement. (Bottom-right inset) The magnification of the main figure showing the abrupt resistance changes in the confinement region. (b) Plot of $\ln(R)$ vs. $1/T$ for the 2 micrometer width microbridge. The slight change in slope may indicate the existence of T_{CO} .

and warming, respectively (see Chapter 2). [9,10] As discussed in Chapter 2, the spatially confined LPCMO films (the lateral dimension is comparable to the size of the electronic phase domains) show abrupt resistance jumps with slight changes of the temperature or the magnetic field because the creation or annihilation of a single percolating filament can dominate the resistance of the entire small-sized sample. These discrete jumps hence provide a signature that spatial confinement is occurring, and identifies the temperature range where this phenomenon is relevant. The temperature dependence of the resistance (R vs. T) for the 2 μm wide LPCMO film in various external magnetic fields is shown in Fig. 5-1(a). (The sample was first field-cooled from room T to 10 K, then the R(T) data were collected upon warming at a rate of 3 K/min.)

Note that in the remainder of the chapter, we shall refer to the non-metallic phase simply as the “insulating state” and not attempt to distinguish between the individual components (such as PMI, COI, charge-disordered insulating (CDI)) within this state. However, for the sake of completeness, we note that in the early study of Hwang et al. [40] the intrinsic electronic phases of $(\text{La,Pr})_{0.7}\text{Ca}_{0.3}\text{MnO}_3$ were considered to be the PMI and FMM phases. However, later studies have shown the evidence of multiphase (FMM, CDI, COI, PMI, etc.) coexistence in LPCMO at $T < T_C$. [8, 11, 19, 51, 52, 56–58] In particular, $(\text{La}_{1-x}\text{Pr}_x)_{0.7}\text{Ca}_{0.3}\text{MnO}_3$ with $x \sim 0.6$ is suggested to be a paramagnetic insulator (PMI) at room temperature (~ 295 K) and a portion of this phase enters into an antiferromagnetic COI state below T_{CO} (~ 220 K). [8, 19, 51, 52, 56–59, 75] The remaining PI regions below T_{CO} have also been referred to as a strain-stabilizing CDI phase. In a bulk system, the PMI to COI phase transition is accompanied by a bump/kink in the sample’s resistance at ~ 220 K. [8, 19, 52] However, this signature can be suppressed in thin films due to the lattice mismatch between the LPCMO film and the STO substrate, i.e., substrate induced strain. [41, 56, 60, 75] (Analogous to the work in Ref. [60], a careful examination of our $\ln R$ vs $1/T$ data (see Fig. 5-1(b)) does show evidence of a slight change in slope at ~ 220 K, consistent with the existence of T_{CO} in our microbridge.) As the temperature of a LPCMO sample is lowered below the T_C and T_{MIT} , FMM domains are believed to be seeding and growing within the insulating phase background. [75] At very low temperatures, the sample is expected to be predominantly in a single-phase ferromagnetic state.

We now return to a discussion of the data in our 2 μm microbridge. Sharp jumps in the resistances are clearly seen below the metal-insulator transition temperature in the temperature range 100 K and 130 K, indicating that the microbridge part of the 2 μm wide film is spatially confined at these temperatures. As briefly mentioned in introduction of this chapter, recall the well-known behaviour in a *wide* LPCMO (and also other manganite) film: at temperatures where phase-competition is taking place, one commonly observes a smooth time-dependent resistance with a relaxation rate of many seconds as the electronic phases slowly evolve with time. [2, 50–52, 54] Either an increase or a decrease of the resistance with time can take place, depending on the nature of the final stable state in the film. For

example, in zero field or low field, the isothermal resistance can increase with time since the high resistance (insulating) state turns out to be the ultimate stable state. On the other hand, the resistance tends to decrease with time when a significant external magnetic field is applied because of the preferential formation of metallic domains. [54]

As we shall discuss in more detail below, and also as reported in Ref. [13] for PCSMO microbridges, when the LPCMO film is spatially confined, the time evolution of the resistance can be very different from the wide film. Fig. 5-2 shows representative resistive time-relaxation behaviour in the $2\ \mu\text{m}$ wide microbridge within the spatially confined temperature region in various magnetic fields. Unlike wide films where the width of the sample is significantly larger than the average size of the electronic phase domains, the resistance in the confined film shows abrupt jumps in addition to the overall change with time. The size as well as the “direction” of the jumps depend on both the temperature and the magnetic field.

Fig. 5-2(a) to (c) show the resistive relaxation behaviour of the $2\ \mu\text{m}$ LPCMO microbridge in zero field. Here, the resistance increases with time, indicating that there is an overall conversion of the FMM regions (low resistance) within the microbridge into insulating states (high resistance), the latter apparently being the long-time equilibrium state in the absence of a magnetic field. Recall that within the microbridge, only a few percolation pathways occur and these govern the behaviour of the entire sample. Therefore, it seems reasonable to surmise that sharp upward (resistance increasing) jumps are observed because within the microbridge, a small FMM region that transforms to insulating phase can sometimes break (at least) one of these pathways and hence significantly increase the resistance of the entire sample. It is notable that these jumps are mostly unidirectional: they all occur in the up direction, suggesting a strong overall preference for the sample to become less metallic as time increases.

The relaxation behaviour of the resistance in an external magnetic field of 1.1 T (the highest field attainable in our apparatus) is illustrated in Fig. 5-2(g) to (i). In contrast to $H = 0\ \text{T}$, at these relatively high fields, the FMM phase forms preferentially. This leads to behaviour that is opposite of that in zero field. In particular, the resistance decreases with time, indicating an overall conversion of the insulating regions into metallic ones. As a consequence, some of these conversions suddenly produce additional percolation paths within the microbridge. Because of the small size of the microbridge, this newly created percolation path(s) dominates the resistance and produces the sharp downward (resistance decreasing) jumps that are seen on top of the overall long-time decrease of the resistance. At this field, the jumps are again essentially unidirectional but in the down direction, in agreement with the tendency for the sample to become more metallic with time.

The fact that low (zero) and high magnetic fields produce an overall increase and decrease, respectively, of the resistance implies that we should be able to find a value of the magnetic field where the time-relaxation can be minimized. As illustrated in Fig. 5-2(d) to

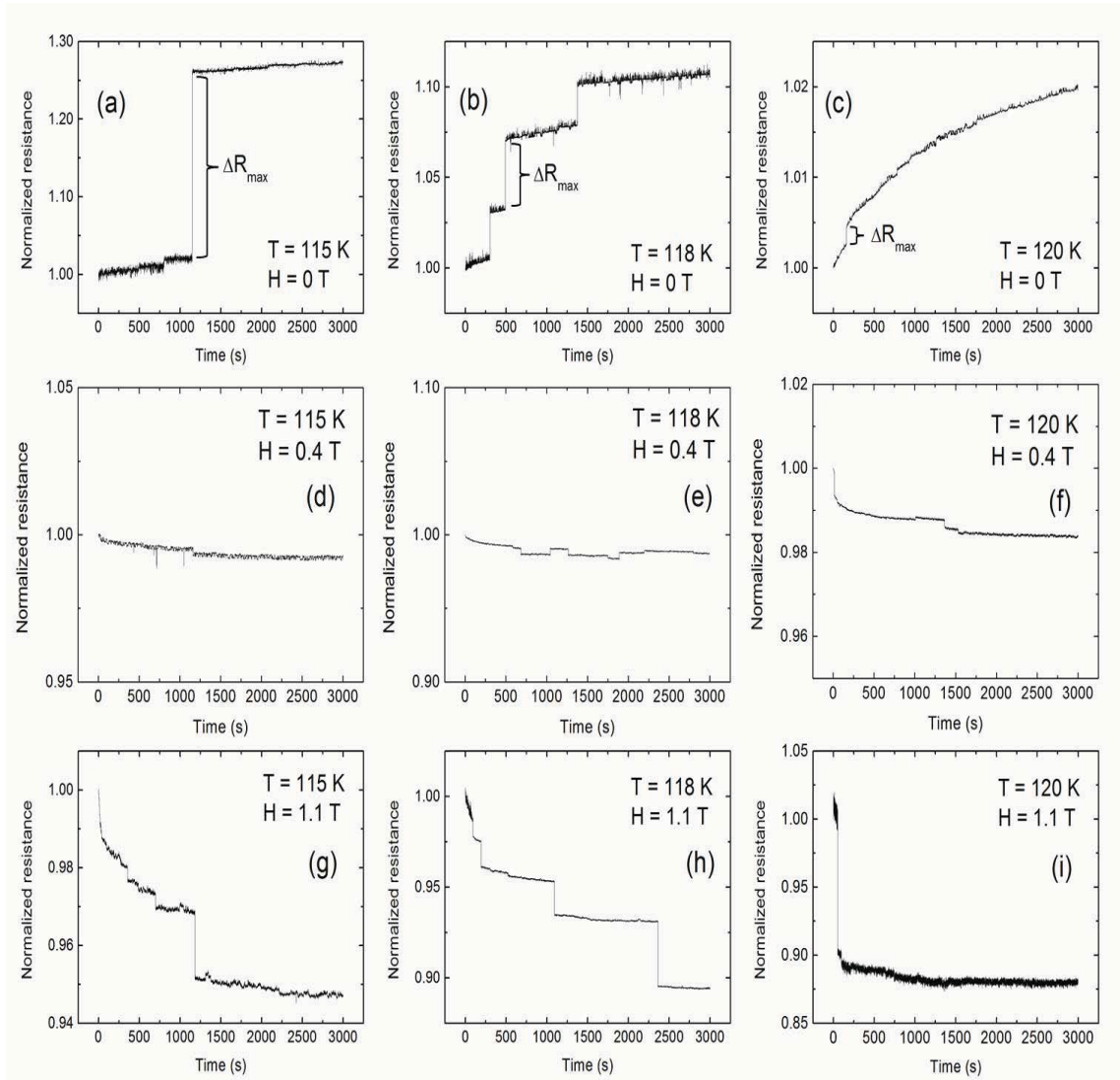


Figure 5.2: Representative time relaxation of the resistance in a 2 micrometer wide LPCMO film at three fields 0 T, 0.4 T and 1.1 T. At each field, the data for three temperatures, i.e., 115 K, 118 K, and 120 K, are shown.

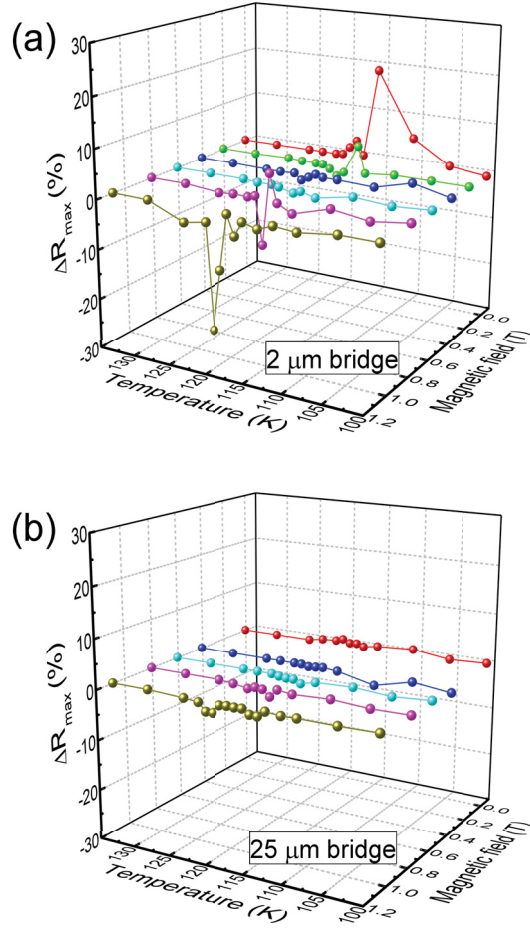


Figure 5.3: (a) The temperature dependence of the normalized maximum resistance jump $\Delta R_{max}(\%)$ in various external magnetic fields for the 2 micrometer wide LPCMO microbridge and (b) for the 25 micrometer wide LPCMO sample.

(f), this indeed occurs when a field of ~ 0.4 T is applied, producing a significant suppression of the long-time relaxation. On the timescale of seconds, the sample continues to exhibit sharp resistance jumps. However, these jumps are of much smaller magnitude than at $H = 0$ T and 1.1 T, and furthermore both up and down resistance jumps can be observed at certain temperatures (see Fig. 5-2(e) for example).

Note that there are variations in the sizes, numbers, and the location in time, of the resistance jumps from one isothermal measurement to another because of the random nature of the phase domain seeding and growth. However, the overall tendencies as illustrated in Fig. 5-2 are maintained. Furthermore, the resistive time relaxation at temperatures outside of the spatially confined temperature region behaves as expected for a wide LPCMO film, i.e., it does not show abrupt resistance jumps (not shown).

In order to quantify the behaviour of the abrupt resistance jumps at a particular tem-

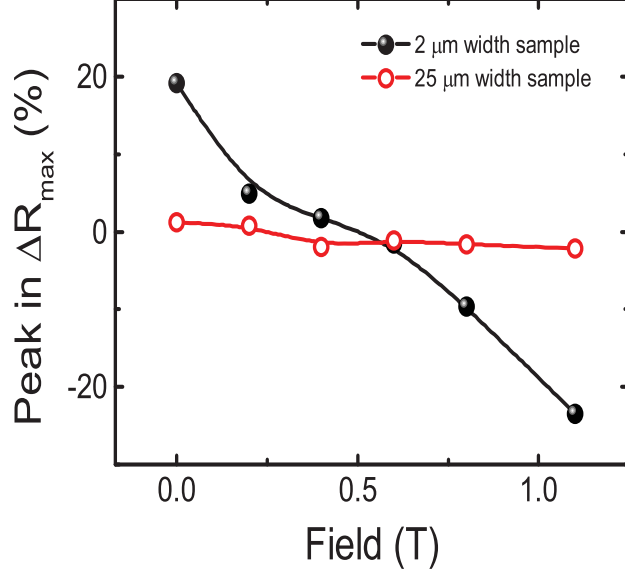


Figure 5.4: (Color online) The magnetic field dependence of the normalized maximum resistance jump $\Delta R_{max}(\%)$ for the 2 micrometer and 25 micrometer wide LPCMO microbridges. As noted in the text, the positive values of $\Delta R_{max}(\%)$ indicate “up” jumps while negative values indicate “down” jumps.

perature, we introduce the parameter $\Delta R_{max}(\%)$. This parameter is defined as $100 \times [R(t_f) - R(t_i)] / R(t_f)$ where $R(t_i)$ and $R(t_f)$ are the values of the resistances at the beginning and end of the largest abrupt resistance jump at a particular temperature (within the measured time interval of 3000 s), respectively. Hence, $\Delta R_{max}(\%)$ is a phenomenological parameter useful for characterizing the “typical size” of the jumps at a fixed temperature; it provides a figure of merit for the “ability” of a conversion of a metallic region into insulating, or vice versa, to create a significant change of the resistance through the microbridge (and hence the whole sample). Note that upward and downward jumps lead to positive and negative $\Delta R_{max}(\%)$, respectively. Examples of this quantity are marked in Fig 5-2(a), (b), and (c).

The magnetic field and temperature dependence of $\Delta R_{max}(\%)$ is shown in Fig. 5-3 for the 2 μm and 25 μm microbridges. As implied earlier, the abrupt resistance jumps are only observed within the spatially confined temperature range as defined by the $R(T)$ measurements. It can be seen from Fig. 5-3 that the magnetic field controls the temperature of the peak in $\Delta R_{max}(\%)$, as well as its magnitude and sign. For example, consider the data for the 2 μm microbridge shown in Fig. 5-3(a) as well as Fig. 5-4. The peaks in $\Delta R_{max}(\%)$ for 0 T and 1.1 T occur close to 115 K and 120 K, respectively. The peak in $\Delta R_{max}(\%)$ is positive at 0 T and monotonically decreases with an increasing field. At 0.4 T, the peak is small and then becomes progressively more negative when the field is further increased (e.g. 0.8 T and 1.1 T). It is hence notable that the magnetic field is such a versatile parameter for tuning not only the existence of sharp percolative jumps within a LPCMO film with

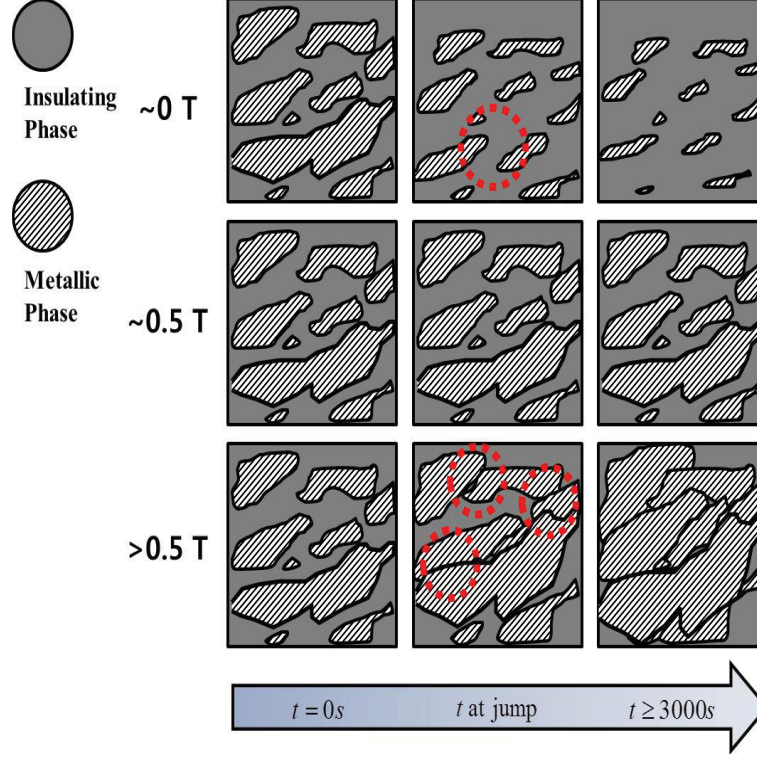


Figure 5.5: (Color online) Illustration of phase domain volume change with time at different constant magnetic fields in the spatially confined microbridge. The red dotted circles indicate the site(s) of interest for explaining the existence of sharp resistance jumps. Note that the phase domains are illustrated based on the experimental observations of FMM domains in Ref. [10].

micron-sized lateral area, but also their directions and magnitudes.

We suggest the following explanations for the behaviour of the peaks of $\Delta R_{max}(\%)$ observed in Fig. 5-3 and Fig. 5-4: A larger magnetic field at a particular temperature produces an increase in the overall volume of the metallic domains within the sample and of course, a reduction of the volume of the insulating regions. Hence, the temperature range where spatial confinement occurs, i.e., when the sizes of domains are comparable with the width of the LPCMO wire, should become closer to the T_{MIT} when the magnetic field is increased since higher temperatures result in smaller sized domains. Since the existence of abrupt resistance jumps only occurs in the spatially confined regime, i.e., where a single conversion of a metallic region into a insulating region (or vice versa) has a strong influence on the resistance of the whole sample, the peak in $\Delta R_{max}(\%)$ should move to higher temperatures as the magnetic field is increased. The magnitude of the peak in $\Delta R_{max}(\%)$ at a fixed temperature and field is determined by how far the starting resistance at $t = 0$ is from equilibrium. The sign of the peak in $\Delta R_{max}(\%)$ is determined by whether the microbridge evolves into a more metallic (downward jumps in resistance and hence negative peaks) or a more insulating (upward jumps in resistance and hence positive peaks)

configuration. Note that at the intermediate field of ~ 0.4 T, the magnitudes of $\Delta R_{max}(\%)$ are close to zero at all temperatures, as is the difference between $R(\infty)$ and $R(0\text{ s})$. This indicates that the total volume fraction of the metallic and insulating domains is nearly time-independent at this intermediate field, which seems to be close to a “critical” value. Application of a significantly lower or higher magnetic field than this critical field results in more dynamic behaviour: at low magnetic fields, the microbridge evolves towards a more insulating state (growth of insulating regions at the expense of FMM ones) while in high magnetic fields, it evolves towards a more metallic state (growth of FMM regions at the expense of insulating ones).

A qualitative model of the time-evolution summarizing the phase volume at different fields is shown in Fig. 5-5. A joining or disjoining of metallic (FMM) domains induces the sharp resistance jump (indicated by the red dotted circles in the illustration) superimposed on the $R(t)$ due to the long-time evolution of the phase fractions. [9,10,53] In particular, (1) at low (or zero) magnetic fields, FMM domains can disjoin as the FMM volume decreases. This can destroy a percolation path(s) within the microbridge, creating the “up” jumps of the resistance superimposed upon an overall increase of the $R(t)$. (2) At high magnetic fields, there is an overall growth of the volume of the FMM domains with time. This can create a percolation path(s) within the microbridge, resulting in “down” jumps of the resistance superimposed upon an overall decrease of the $R(t)$. (3) At a certain magnetic field (~ 0.4 T in our sample), the long-time resistance relaxation as well as the sharp jumps are suppressed because the average FMM and insulating volumes are time-independent. Experimentally, our field of 0.4 T is not exactly at this critical field, and hence some long-time relaxation as well as a combination of “up” and “down” sharp jumps are observed in $R(t)$.

By contrast to the behaviour described above for the $2\ \mu\text{m}$ wide microbridge, the $25\ \mu\text{m}$ wide bridge shows only relatively weak $\Delta R_{max}(\%)$ within the field range studied (see Fig. 3(b)). This sample is approaching the non-confined limit (behaves as a “wide” sample) at all temperatures and magnetic fields, where many percolating paths contribute to the behaviour of the resistance.

Finally, we note that in addition to the sporadic resistance jumps that we have described in this chapter, the frequent jumps in $R(t)$ analogous to those observed in Ref. [14,55] are sometimes also seen. These “telegraph noise” patterns can vary significantly from one measurement to another. They are beyond the scope of the present studies, but it may be interesting to investigate them over a wide range of magnetic fields and temperatures in the future. Furthermore, since it is known that the $(\text{La}_{1-x}\text{Pr}_x)_{1-y}\text{Ca}_y\text{MnO}_3$ series shows a rich electronic/magnetic phase diagram, [8,58,59] modification of the cation/hole doping concentration could be another avenue of investigating the metastability of the different coexisting phases in LPCMO microbridges.

5.4 Conclusions

In conclusion, we have investigated the temperature and magnetic field dependence of the long-time resistive metastability in spatially confined $\text{La}_{0.3}\text{Pr}_{0.4}\text{Ca}_{0.3}\text{MnO}_3$ thin films. It is found that the sharp resistance jumps during time relaxation measurements occur in the temperature range where the sizes of the competing electronic phase domains are comparable to the lateral dimension(s) of the LPCMO film, such as in the $2\ \mu\text{m} \times 2\ \mu\text{m}$ microbridge. These jumps can be tuned by the magnetic field: At low magnetic fields, the sharp jumps can be large and increase the resistance of the sample. At high magnetic fields ($\sim 1\ \text{T}$), the sharp jumps can also be large but decrease the resistance of the sample. An intermediate field ($\sim 0.4\ \text{T}$) exists where almost no resistance jumps occur. A qualitative model is introduced to explain these results. Such information is useful for improving the scientific understanding of the metastability of a spatially confined manganite system over a broad range of external magnetic field and temperature, and may also have ramifications for single domain phase engineering for applications.

Chapter 6

Low Field Colossal Anisotropic Magnetoresistance in Spatially Confined Electronically Phase Separated LPCMO Microbridges

6.1 Introduction

The anisotropic magnetoresistance (AMR), i.e., the values of the resistance that depend on the direction of the magnetic field with respect to either the current direction or the crystal axes, is an important property for various applications, such as sensors of magnetic field directions. In these applications, having a high value of the AMR improves the detector's sensitivity and the corresponding read times, etc. [61–63] The magnitudes of the AMR in some manganites are significantly larger than the values of $\sim 5\%$ to $\sim 20\%$ in ferromagnetic 3d alloys [64] that are commonly used in present sensor technologies, and can be as high as $\sim 40\%$ and $\sim 200\%$ for in- and out-of-plane configurations, respectively. [17, 18, 65] Furthermore, unlike the 3d alloys, the AMR in many manganites varies significantly with temperature and has a peak near the metal-insulator transition temperature T_{MIT} . [63, 66–69] Although, the mechanism of the AMR in these electronically phase separated (EPS) manganites is still an ongoing topic of discussion, mechanisms such as the spin-orbit and magneto-elastic couplings have been suggested to be important for explaining its existence. [67, 70, 71]

A possible method of dramatically modifying the AMR in a manganite is to fabricate a system which is dominated by the anisotropic volume growth of the metallic domains under an applied magnetic field \mathbf{H} . The orientation of \mathbf{H} can then be used to sensitively change the nature of the percolation, and hence lead to highly field-direction-dependent resistivities. A potentially excellent experimental realization of such a system is a spatially confined thin film of manganite whose lateral dimensions are made comparable to the sizes of the metallic and insulating domains within the sample.

Recent investigations [47,65] have shown that the AMR in LPCMO microbridges behave differently from wide films of LPCMO. In Ref. [47], Alagoz et al. reported sharp jumps in the resistivity (and hence AMR) during the isothermal in-plane rotation of \mathbf{H} in a narrow temperature range below the T_{MIT} of $\text{La}_{0.3}\text{Pr}_{0.4}\text{Ca}_{0.3}\text{MnO}_3$ microbridge. The observation by Chen et al. [65] of a “giant” enhancement of the in-plane AMR, i.e., the difference in the resistivities when the field is applied in the film’s plane in directions parallel and perpendicular to the current direction, in a $\text{La}_{0.325}\text{Pr}_{0.3}\text{Ca}_{0.375}\text{MnO}_3$ stripe of micrometer width is of particular relevance to our present work. They observed a low-temperature in-plane giant AMR peak with a magnitude close to 40 %. The result was explained with a phenomenological model where the AMR at lower temperature is due to the metallic domain elongation along the external magnetic field direction. The enhancement of the AMR in this dimensionally reduced system compared to a wide film is certainly noteworthy, but we suggest that a much more prominent enhancement of the AMR should be possible in a truly spatially confined EPS system. For example, no sharp jumps in the temperature dependence of the resistance are seen in their samples; the lack of this signature suggests that their stripes are barely in the spatially confined limit, and therefore do not experience the full benefit of anisotropic domain percolation.

In this chapter, we report the generation of “colossal” anisotropic magnetoresistance (C-AMR) in $\text{La}_{0.3}\text{Pr}_{0.4}\text{Ca}_{0.3}\text{MnO}_3$ wires of a few micrometers in width and which are clearly narrow enough to trap a small number of metallic and insulating domains. These microbridges can exhibit an in-plane AMR that is as high as about 16,000 %, i.e., several orders of magnitude larger than any previously reported in-plane AMR in manganite films. Notably, the enhancement of the in-plane AMR occurs at low magnetic fields, a regime that is of particular interest for applications. The origin of the C-AMR is discussed within a phenomenological anisotropic domain growth model.

6.2 Experimental details

$\text{La}_{0.3}\text{Pr}_{0.4}\text{Ca}_{0.3}\text{MnO}_3$ films of thickness 45 nm were deposited on SrTiO_3 substrates by off-axis direct current (d.c.) magnetron sputtering. The deposition was carried out at 750°C in an oxygen-argon mixture, with O_2 and Ar pressures of 100 mTorr and 20 mTorr, respectively. The detailed film synthesis process can be found in Chapter 3. X-ray diffraction (XRD) measurements carried out on the LPCMO/STO films confirmed that they are epitaxial, single phased, and subjected to tensile strain. The films were then patterned using photo-lithography and chemical wet-etching. A chemical solution of $\text{HCl} + \text{H}_2\text{O} + \text{KI}$ was used for the wet-etching at a rate of ~ 0.64 nm/s. In the temperature dependent resistance ($R(T)$) measurements, the sample was cooled from room T with a rate of 3 K/min. Home-made LABVIEW drivers were used for the data acquisition and system control. In order to directly compare between the “wide” and “spatially confined” configurations, both types of resistances were measured on a single film. The “wide film” resistance was measured be-

tween the two Ag electrodes marked I+ and V+, while the “spatially confined” resistance was measured for the microbridge using the four Ag electrodes I+, V+, I- and V- (see the Fig. 6-1(a)). A Keithley 6221 DC/AC current source and Keithley 2182A nanovoltmeter were used in these measurements.

6.3 Results and discussion

We first note that we fabricated a number of confined microbridges with different geometries (straight and zig-zag) and lengths. They could be grouped into two categories but without a clear correlation with the shape of the system: (a) microbridges whose $R(T)$ displays large sharp percolation jumps just below T_{MIT} ; (b) microbridges whose $R(T)$ displays percolation jumps which are two or three orders of magnitude smaller than the former ones. It is found that microbridges from the first category can consistently manifest C-AMR. Hence, we will start by presenting the C-AMR properties of a notable member from this group.

Fig. 6-1(a) shows the schematic diagram and the microscope images of the microbridge part of the primary samples discussed in this chapter. The main part of Fig. 6-1(b) presents $R(T)$ at $H = 0.2$ T for the wide part (2 mm width) and the spatially confined (microbridge) part of the same film. The magnetic field was applied in the film’s (x-y) plane with an angle $\theta = 0^\circ$ and 90° , where the angle θ is defined in Fig. 6-1(a). The microbridge has a width of $2 \mu\text{m}$ and a total length of $56 \mu\text{m}$ with sections along the x and y axes as indicated in Fig. 6-1(a).

The different results between the wide and confined parts of the sample, shown for 0.2 T, are clearly apparent in Fig. 6-1(b): (1) The microbridge part shows abrupt resistance jumps below the T_{MIT} whereas the wide part presented a conventional metal-insulator transition curve. As discussed in more detail elsewhere (also in previous chapters), [42,72] the sharp jumps in $R(T)$ in the microbridge signify that the sample is in a temperature region where the size of the EPS is comparable to the width of the bridge and only a small number of domains are controlling its resistance. Here, as the microbridge’s temperature decreases, the volume fraction of COI domains decreases while FMM domains continually grow. When the FMM domains, which are separated by the COI domains, percolate with other neighboring FMM domains, the resistance abruptly decreases. (2) Notably, in the microbridge, the temperatures of the abrupt jumps are strongly dependent on the direction of the magnetic field, i.e., θ . For instance, the largest drop in the resistance occurs at 103.5 K for $\theta = 90^\circ$ compared to 95 K for $\theta = 0^\circ$. Consequently, in the microbridge, there is a gigantic AMR in the temperature interval sandwiched by the $\theta = 0^\circ$ and $\theta = 90^\circ$ primary drop temperatures. (Although features such as the sharp jumps, etc. occur at slightly different temperatures due to the random nature of the domain seeding [14,55] within the microbridge, the results on the AMR are generally reproducible if the measurements are repeated within the same sample.) The wide part of the film does not exhibit such behaviour since the resistances in different field directions are very similar and therefore its AMR remains relatively small at

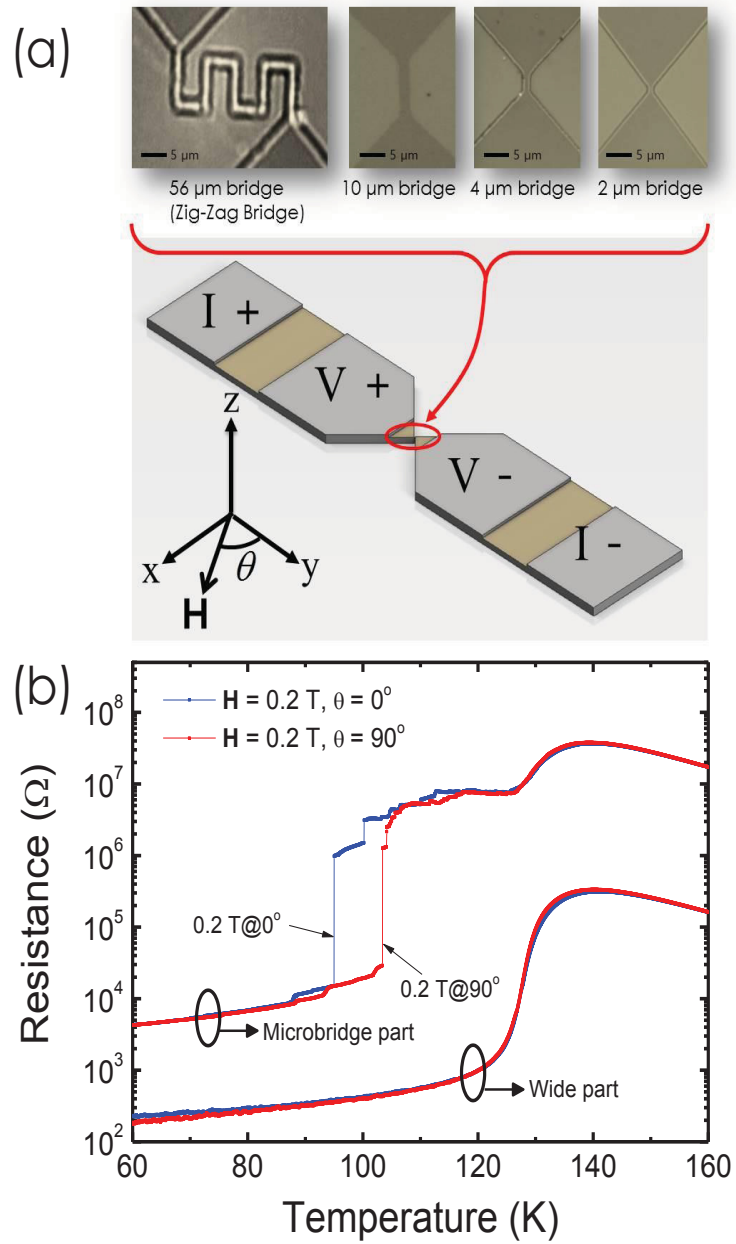


Figure 6.1: (a) Schematic diagram of the microbridge and its optical microscope images. (b) Temperature dependence of the resistance measured separately for the wide part of the sample and the zig-zag microbridge. The resistance was measured in 0.2 T for both 0 degree and 90 degree orientations of the magnetic field.

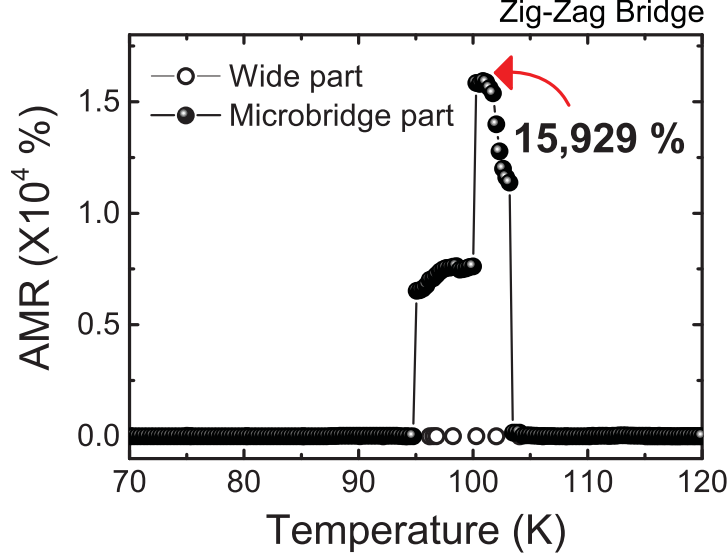


Figure 6.2: Temperature dependence of the in-plane AMR at $H = 0.2$ T, applied at 0 degree and 90 degree, for the zig-zag microbridge. Note that very high values of about 16,000 % are reached. The AMR measured for the wide part of the film is very small (~ 20 %) compared to that of the microbridge.

all temperature range.

In order to quantify the anisotropy in the resistance, we define the in-plane AMR as

$$AMR = \frac{(R_{\parallel} - R_{\perp})}{R_{\perp}} \times 100\% \quad (6.1)$$

where R_{\parallel} and R_{\perp} are the resistances for $\theta = 0^{\circ}$ and $\theta = 90^{\circ}$, respectively. The temperature dependence of AMR at $H = 0.2$ T is shown in Fig. 6-2. The maximum magnitude of the AMR of the wide part of the film is only about ~ 20 % and occurs close to its T_{MIT} , similar to that conventionally seen in other manganites. [63, 66–69, 73] In contrast to the AMR behaviour (single peak near the T_{MIT}) in the wide part of the film, the AMR in the microbridge is double peaked: one peak occurs close to the T_{MIT} with a magnitude of $\sim 10\%$ (not seen in Fig. 6-2 because of the scale) while the other peak has an extraordinary value of $\sim 16,000$ %. This “colossal” value of the AMR occurs in the temperature region where the abrupt jumps occur in Fig. 6-1 and is remarkably higher compared to any reported in-plane AMR values in manganite films (magnitudes less than ~ 40 %).

We emphasize that the C-AMR is unique to the spatially confined geometry where only a few domains are trapped. Our results imply that within this particular microbridge, the metallic domains are anisotropic in shape and are preferentially elongated [74, 75] along (or in the vicinity of) the x direction. Upon cooling, as the elongated domains grow in size, this leads to the appearance of percolation at higher temperatures for $\theta = 90^{\circ}$ (H along the x direction) compared to $\theta = 0^{\circ}$ (H along the y direction) and the resultant abrupt

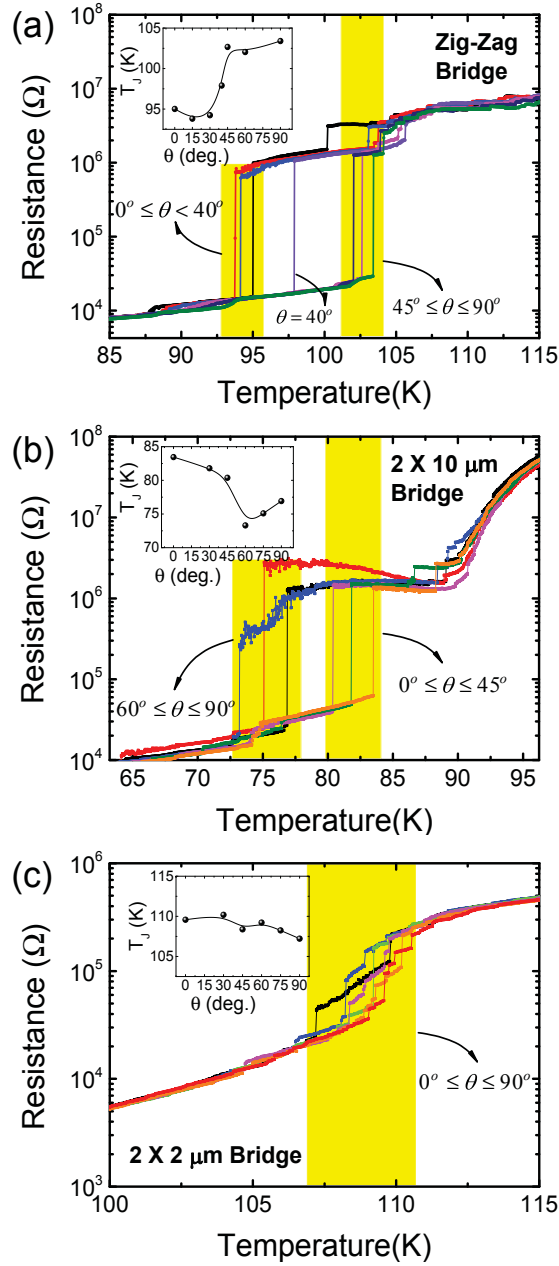


Figure 6.3: Temperature dependence of the resistance measured for various orientations (angle) of the magnetic field for (a) the zig-zag microbridge, (b) a 2 by 10 microbridge, and (c) a 2 by 2 microbridge. The insets show the temperature at which the maximum resistance jumps occur, T_J , plotted as a function of the angle. Note that the resistance jumps occur at two different temperature regions for the zig-zag microbridge but is less clear in the straight-line microbridges.

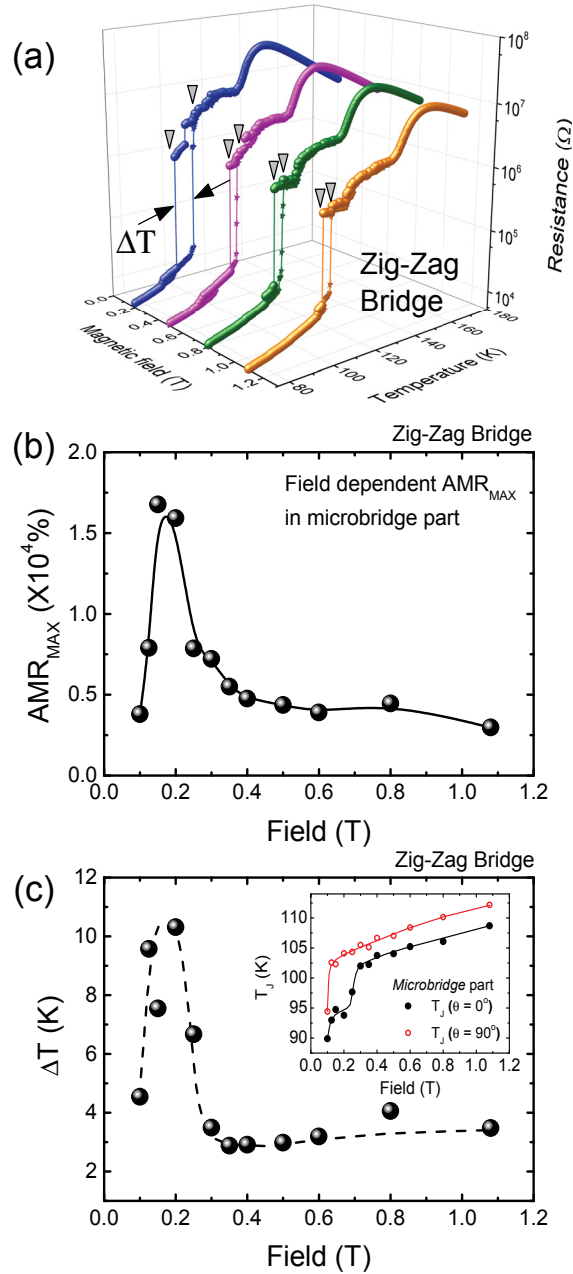


Figure 6.4: (a) Dependence of resistance on temperature and magnetic field for the zig-zag microbridge for angle of 0 degree and 90 degree. The vertical arrowheads mark temperatures at which the largest resistance jumps occur. ΔT denotes the temperature difference between the largest resistance jumps measured at angle of 0 degree and 90 degree. (b) The magnetic field dependence of the maximum AMR. At each field, this quantity is obtained from the temperature dependence of the AMR using data that are analogous to that shown in Fig. 6-2. (c) Dependence of ΔT and T_J on magnetic field for the zig-zag microbridge. As indicated previously, T_J is the temperature at which the maximum resistance jumps occur while the ΔT is the temperature difference between T_J (at 90 degree) and T_J (at 0 degree).

drop in the resistance occurs at higher temperatures in the former. As a consequence, there is a temperature interval where colossal AMR exists. At lower temperatures where the metallic volume fraction is large and dominates the resistance of the microbridge, the role of the anisotropy in the percolation diminishes and the AMR due to this mechanism diminishes since the resistances at $\theta = 0^\circ$ and $\theta = 90^\circ$ become similar. Hence, the much smaller observed values of the AMR at temperatures outside of the percolation regime are attributed to an intrinsic mechanism such as the spin-orbit interaction. [67, 73, 76]

Further insight into the creation of C-AMR was obtained by carrying out measurements of $R(T)$ in a field of 0.2 T for angles θ between 0° and 90° (see Fig. 6-3(a)). As shown in Fig. 6-3(a), for each value of θ studied, there exists a particularly large abrupt jump in the resistance at a temperature which we will label as T_J . Interestingly, the values of T_J can be grouped into two distinct temperature regions for the zig-zag bridge (yellow rectangles in Fig. 6-3(a) and the inset). For angles below 40° , T_J is between 92.5 K and 95.0 K whereas for angles between 45° and 90° , T_J has a value between 102.5 K and 104.0 K. The measurements performed on straight microbridges, such as a $2 \mu\text{m} \times 10 \mu\text{m}$ microbridge (Fig. 6-3(b)) that also displays C-AMR but with peak values of only $\sim 3,700\%$ instead of $\sim 16,000\%$, revealed separation of T_J values but are not as clearly grouped as in the zig-zag bridge. Finally, the microbridges that show small jumps in R vs T and no C-AMR, for example the $2 \mu\text{m} \times 2 \mu\text{m}$ microbridge shown in Fig. 6-3(c), do not display a clear separation in T_J . These results imply that the magnitude of the C-AMR is correlated with the existence of a large separation of the T_J values. This large separation could be caused by the domains which are “trapped”/“pinned” in certain directions; the ones that follow the domain growth preferred direction and the other ones that are perpendicular to the domain growth preferred direction. For magnetic fields that are applied in directions that are along, or in the vicinity to, one of these “special” orientations, the resultant $R(T)$ are very similar.

At this point, it may be tempting to associate the existence of the preferred domain growth directions with the geometry of the microbridge. For example, a zig-zag microbridge is longer and possesses more edges and corners than a straight microbridge and these differing configurations may be responsible for the special directions. However, we have found that microbridges with the same geometries grown on nominally identical STO substrates display considerable variance in the size of the percolation jumps and hence the C-AMR. Hence, although the geometry of the microbridge may certainly play some role in controlling the C-AMR, it is not the major factor. Instead, we suggest that the observed behaviour may be caused by the following factors: (a) The structural phase transition intrinsic to the STO substrate. Twin boundaries are formed in STO during its cubic-to-tetragonal structural phase transition near 105 K. [77] These defects introduce non-uniform deformations into the LPCMO microbridge that may enhance the field-dependent anisotropy in $R(T)$ and the AMR. [78, 79] (b) A non-uniform distribution of micro-strains that create

“trapping”/“pinning” of FMM domains in certain orientations. [42] The non-uniformity of the strain could be produced by a non-uniform oxygen distribution on the surface of the STO substrate. This in fact, has been shown to occur during thin film deposition at high temperatures. [80,81] SEM/EDS analysis of the surface of our STO substrates before and after thin film deposition confirmed that the oxygen distribution in the STO substrates becomes more inhomogeneous after the film deposition. The details of the thin film growth process, which could lead to a non-uniform distribution of micro-strains, are likely to be important in determining the strength of these unique transport properties. Such factors may also be responsible for the differences observed in Ref. [65] (bridge width $1.5 \mu\text{m}$) and in our studies (bridge width $2 \mu\text{m}$).

Finally, we detail how the C-AMR can be tuned by the magnetic field strength by presenting the magneto-transport properties of the zig-zag microbridge for H up to 1.1 T. Typical R(T) curves for $\theta = 0^\circ$ and $\theta = 90^\circ$ and several H are shown in Fig. 6-4(a). These data enable us to monitor the temperature T_J (at which the largest abrupt jump in R(T) takes place) as well as the size of the jump at this temperature. Several features are notable: (1) As shown in Fig. 6-4(b), there is a peak in AMR_{MAX} , the maximum value of the in-plane AMR(T) for a particular field, at a relatively low magnetic field of ~ 0.2 T. This peak value of AMR_{MAX} is $\sim 16,000$ %. If the magnetic field is increased beyond 0.2 T, AMR_{MAX} declines with increasing field, concomitant with the overall suppression of the size of the resistance jump at T_J . It should be emphasized, however, that the AMR at magnetic fields away from H_{MAX} are still much larger than those reported in other manganites. (For example, the $\text{AMR}_{MAX} \sim 3,800$ % and $\sim 3,000$ % at 0.1 T and 1.1 T, respectively.) (2) The temperature T_J for both $\theta = 0^\circ$ and $\theta = 90^\circ$ increases with increasing H (along with the T_{MIT}), as shown in the inset of Fig. 6-4(c). The difference $\Delta T = T_J(90^\circ) - T_J(0^\circ)$ shown in Fig. 6-4(c) is therefore the temperature range where the percolation enhanced AMR is expected to occur. Both ΔT and AMR_{MAX} occur at approximately the same field (i.e. ~ 0.2 T). At a particular temperature, one expects the fractional volume of the metallic domains within the microbridge to increase with magnetic field. The decrease of both ΔT and AMR_{MAX} in high fields may reflect the progressively reduced influence of a single domain percolation event on the resistance because the electronic phase separation is no longer comparable to the lateral size of the microbridge.

6.4 Conclusion

In conclusion, colossal low field (~ 0.2 T) in-plane anisotropic magnetoresistance (C-AMR) greater than 16,000 % can be created in spatially confined LPCMO films.

Here, we would like to emphasize that the C-AMR found in this sample ($\sim 16,000$ %) is remarkably greater by many orders of magnitude compared to any reported in-plane AMR values in standard manganite films (20 % \sim 40 %) or in ferromagnetic 3d alloys (5 % \sim 20 %). Having a high value of the AMR is especially important for improving the detector’s

sensitivity and the corresponding read times, etc. [61–63]

We believed the C-AMR in the spatially confined LPCMO thin film is caused by anisotropic domains growth process upon cooling the sample. This study may be propaedeutic to a way of enhancing the anisotropic magneto-transport properties in manganite systems and may be relevant for next generation sensor and switching applications.

Chapter 7

Current Dependence of Colossal Anisotropic Magnetoresistance in LPCMO Microbridges

7.1 Introduction

In the previous chapter (Chapter 6), we have reported the observation of “colossal” anisotropic magnetoresistance (C-AMR) in $\text{La}_{0.3}\text{Pr}_{0.4}\text{Ca}_{0.3}\text{MnO}_3$ microbridges at low magnetic fields (~ 0.2 T). The resistance in these confined systems can be strongly dependent on the direction of the magnetic field, showing an in-plane AMR that is as high as $\sim 16,000$ %, i.e., several orders of magnitude larger than any values previously reported in manganite films, and was attributed to the existence of anisotropic percolation within the microbridge. These effects are much larger than those due to the spin-orbit interaction which causes conventional AMR.

The study in this chapter is motivated by the knowledge that applying an electric current to the manganite can significantly change the nature of the percolation within the sample. In particular, a number of studies have shown that a percolation channel of the metallic domains can be created by applying a sufficiently large electric current in certain EPS manganite films. [14, 82–86] For example, Ward et al. [14] reported that increasing the current in a confined $(\text{La}_{1/2}\text{Pr}_{1/2})_{5/8}\text{Ca}_{3/8}\text{MnO}_3$ wire changes a single domain’s preferred state from insulating to metallic while Tokubo et al. [82] presented evidence that an electric current stabilizes the metallic state in a thin film of $\text{Pr}_{1-x}(\text{Ca}_{1-y}\text{Sr}_y)_x\text{MnO}_3$ ($x=0.45$, $y=0.25$). Given the sensitivity of the EPS state and hence the percolation properties to the bias current, one may expect that the current can significantly modify the C-AMR within a spatially confined LPCMO microbridge; however, the extent of such a manipulation has thus far not been reported.

In this chapter, as an extension of Chapter 6, we report attempts to control the magnitude of the colossal in-plane anisotropic magnetoresistance by varying the bias d.c. current in spatially confined thin films of $\text{La}_{0.3}\text{Pr}_{0.4}\text{Ca}_{0.3}\text{MnO}_3$. Dramatic increases of the in-plane

C-AMR magnitudes are observed by reducing the bias current. For example, one of our samples exhibited a variation in the C-AMR from $\sim 900\%$ to over $\sim 24,000\%$ as the current is decreased from $1\ \mu\text{A}$ to $10\ \text{nA}$ (at low magnetic fields). These studies demonstrate that the d.c. bias current can be a method to artificially tune, via changes to the percolation, the in-plane C-AMR in spatially confined LPCMO systems over a wide range of values.

7.2 Results and discussion

Fig. 7-1(a) and (c) show the resistance vs temperature profiles at different bias currents in the spatially confined LPCMO microbridge of $56\ \mu\text{m}$ length at $H = 0.2\ \text{T}$ and $1.1\ \text{T}$, respectively, for the magnetic field applied in the direction $\theta = 0^\circ$ (see Fig. 6-1 for the definition of θ). Note that the samples used in this chapter are the same samples studied in Chapter 6 and have been described in detail there. This sample shows the largest C-AMR among all the samples that were studied. Note that only the temperature range (which is below the metal-to-insulator transition temperature) where signatures due to spatial confinement exist, i.e., sharp jumps in resistance, is shown in the figure. It turns out that this is also the temperature regime where there are particularly noticeable changes in the R vs T profiles due to the magnitude of the bias current. In this temperature regime, the sharp jumps in resistance are strongly dependent on the applied bias current, whereas either very weak or no clear current dependence is found outside this temperature region, i.e., $T < 85\ \text{K}$ or $T > 125\ \text{K}$. At low bias currents, the sample has a tendency to show sharp resistance jumps with large magnitudes while the sharpness and the magnitude of the jumps are more likely to be suppressed at high currents. Similar features are also observed when the field orientation is at $\theta = 90^\circ$ (see Fig. 7-1(b) and (d)). However, due to the anisotropy of the domain percolation in the confined part of the sample, the main jumps in the resistance occur at higher temperatures compared to those at $\theta = 0^\circ$, which leads to the existence of the C-AMR (see Chapter 6).

The effect of the bias current on the C-AMR is shown in Fig. 7-2 where the C-AMR is defined as $[(R_{\parallel} - R_{\perp})/R_{\perp}] \times 100\%$ where R_{\parallel} and R_{\perp} are the resistances for magnetic field applied along $\theta = 0^\circ$ and $\theta = 90^\circ$ respectively. For both $H = 0.2$ and $1.1\ \text{T}$, there is a general tendency for the maximum C-AMR magnitude to decrease as bias current increases, with the changes being more systematic at the higher magnetic field. (From previous studies of the magnetic field dependence of the C-AMR in this sample (Chapter 6) it was found that the largest AMR at a fixed bias current of $100\ \text{nA}$ occurs at $\sim 0.2\ \text{T}$.) Furthermore, note that the temperature range of the C-AMR moves toward higher temperature at greater bias current.

The maximum value of the C-AMR vs. bias current at $H = 0.2\ \text{T}$ and $1.1\ \text{T}$ is plotted in Fig. 7-3. As noted above, a dramatic increase of the C-AMR is found when the bias current is decreased. In fact, in this sample, the current can be used to adjust the C-AMR_{MAX} by nearly an order of magnitude: from a remarkably large value of $\sim 24,000\%$ at $10\ \text{nA}$ for H

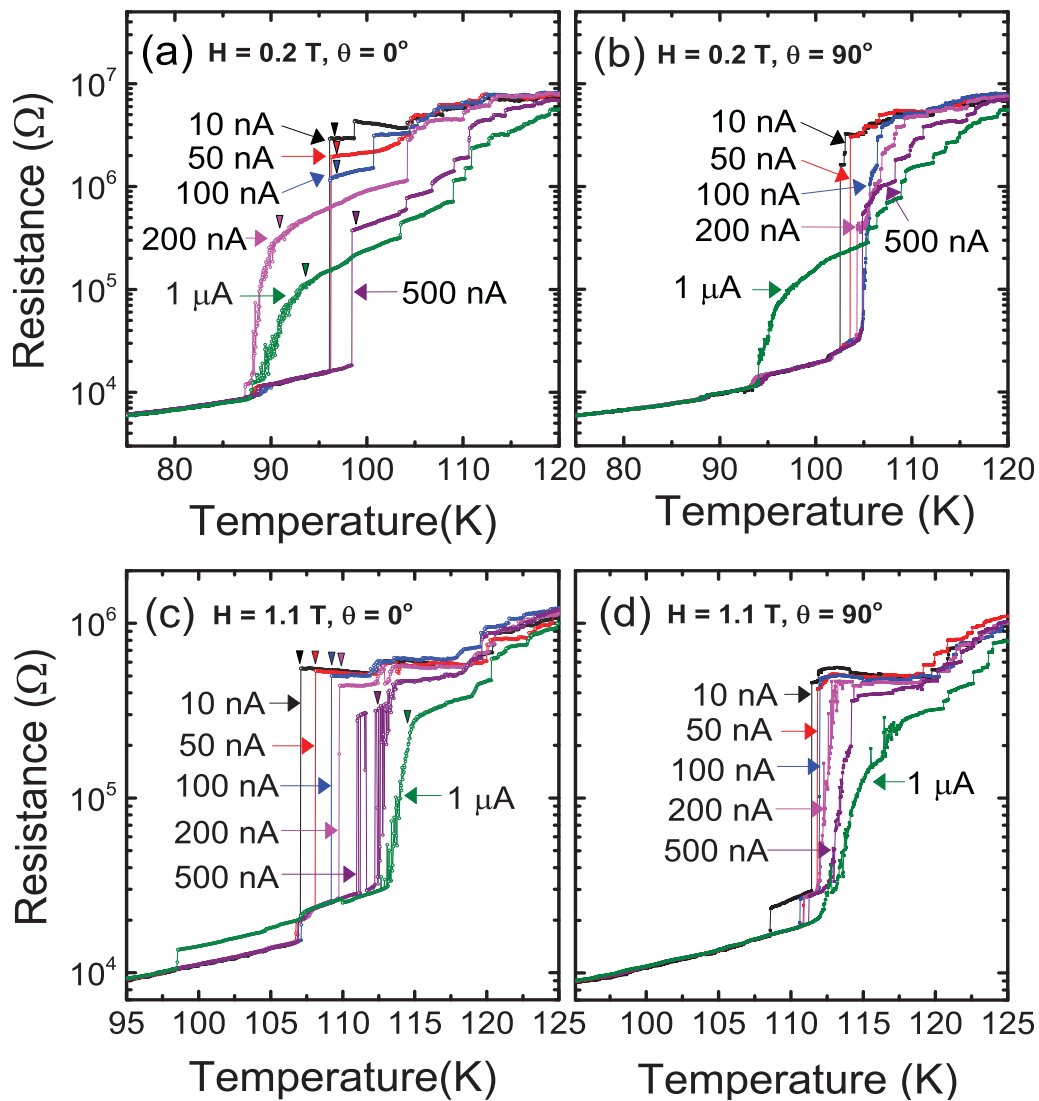


Figure 7.1: Temperature dependence of resistance at different applied d.c. currents upon application of the external magnetic field of (a) 0.2 T at 0 degree, (b) 0.2 T at 90 degree, (c) 1.1 T at 0 degree, and (d) 1.1 T at 90 degree in the microbridge of 56 micrometer length (2 micrometer width).

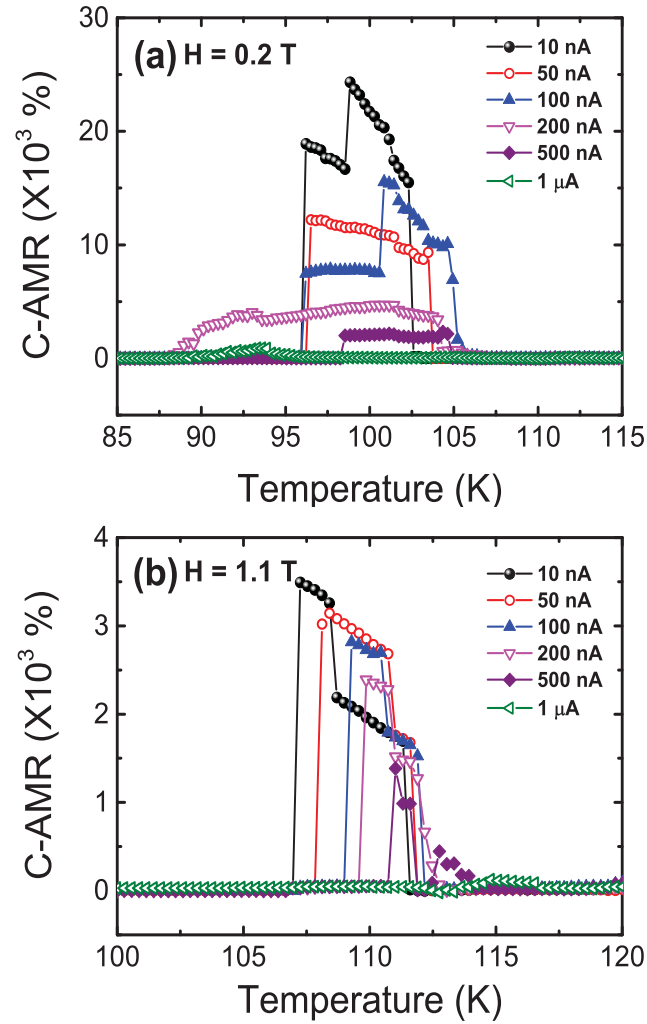


Figure 7.2: Temperature- and applied d.c. current-dependence of the in-plane C-AMR at (a) $H = 0.2$ T and (b) $H = 1.1$ T, respectively, in the microbridge of 56 micrometer length (2 micrometer width).

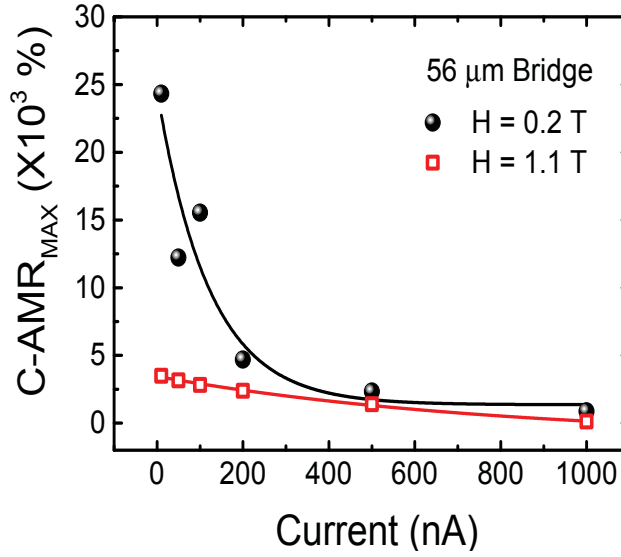


Figure 7.3: Applied d.c. current dependence of the maximum AMR magnitude at 0.2 T and 1.1 T, respectively.

= 0.2 T (which is $\sim 50\%$ higher than our previous $C\text{-AMR}_{MAX}$ of $\sim 16,000\%$ reported in Chapter 6 for 100 nA) to $\sim 900\%$ at $1\ \mu\text{A}$. Furthermore, there is a large difference in $C\text{-AMR}_{MAX}$ between 0.2 T and 1.1 T at low currents, but this difference is much smaller at high currents.

We now discuss the mechanisms for the above results. It was suggested in previous chapters that C-AMR exists, at a particular (magnitude of) magnetic field and bias current, because the metallic domains are anisotropic in shape and are preferentially elongated along the x-direction compared to the y-direction (for reasons that are still being investigated, also see Chapter 6). Upon cooling the sample, the elongated domains grow in size but percolation occurs at higher temperatures for $\theta = 90^\circ$ (magnetic field along the y direction) compared to $\theta = 0^\circ$ (magnetic field along the x direction) and the resultant abrupt drop in the resistance occurs at higher temperatures in the former. Hence, there is a temperature interval where colossal AMR exists. As discussed in the previous chapter, at a fixed bias current, the decrease of the $C\text{-AMR}_{MAX}$ at high magnetic fields compared to the low fields (see Fig. 7-2 and Fig. 7-3) may reflect the progressively reduced influence of a single domain percolation event on the resistance because the electronic phase separation is no longer comparable to the lateral size of the microbridge.

Turning to our present results regarding the dependence of the C-AMR on the bias current, it appears that when a higher current is applied to our sample within the confinement temperature region, the system prefers to be in a more metallic configuration. For example, the resistance level at temperatures slightly above the onset of the jumps (see Fig. 7-1) tends to decrease with increasing the bias current. Also, we have observed that at a fixed

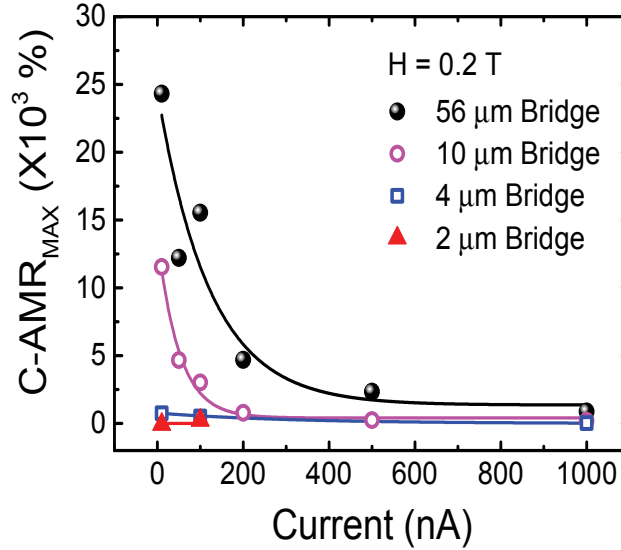


Figure 7.4: Applied d.c. current dependence of the maximum AMR magnitude at 0.2 T for different bridge lengths.

temperature within the confinement regime, increasing the current often produces sudden decreases in the resistance (not shown), i.e., into a more metallic state. The increase of the volume fraction of the metallic phase with increasing current also produces more percolation paths through the confined part of the sample as the electronic phase separation becomes no longer comparable to the size of the microbridge (analogous to the effect of increasing the magnetic field). This effect decreases the magnitude of the (largest) percolation jumps in the R vs T profile and consequently the C-AMR (see Fig. 7-2 and Fig. 7-3). As seen in Fig. 7-3, the difference between the $C\text{-AMR}_{MAX}$ at 0.2 T and 1.1 T is significantly larger at low bias currents compared to high currents. At the higher values of the injected currents, the creation of “many” conduction paths implies that the shape anisotropy induced by the direction of the magnetic field becomes comparatively much less influential. Note that the increase in metallicity with the bias current also produces a general tendency for the temperature of the largest resistance percolation jump to increase with the current (see Fig. 7-1). Hence, it is reasonable to find an accompanying increase in the temperature range of the C-AMR toward higher temperature with greater bias current (see Fig. 7-2).

Incidentally, we suggest that, as proposed by Refs. [22,82], the injected current enhances the metallic state within the system because it favors ferromagnetism through the double exchange interaction. Note that the Joule heating effect is deemed to be a less likely mechanism since the shift of the jump temperature is opposite to what is expected from the heating effect of the current. i.e., In our microbridge, the metallic phase is less favorable at higher temperatures and therefore, one would expect that the larger bias current induces the jump transition at lower temperature if Joule heating was the cause of the shift. [82, 86–88]

Finally, we have checked that the observed bias current dependence of the C-AMR is a general phenomenon in other confined LPCMO films. Consider, in particular, the 10 μm bridge which happens to exhibit significant low field C-AMR. As shown in Fig. 7-4, the low-field C-AMR increases strongly with decreasing current, qualitatively analogous to the behaviour shown by the 56 μm bridge. On the other hand, the 4 and 2 μm bridges were samples that did not exhibit any low field C-AMR; this quantity remains small for all values of the bias current.

7.3 Conclusion

In conclusion, the magnitude of the colossal in-plane anisotropic magnetoresistance in spatially confined LPCMO thin films can be dramatically modified by using the bias d.c. current to change the percolation within the sample. As an example, the low field anisotropic magnetoresistance value was changed from $\sim 900\%$ to over $\sim 24,000\%$ as the current is decreased from 1 μA to 10 nA. These studies demonstrate that the d.c. bias current can be a useful method for adjusting the colossal anisotropic magnetoresistance in spatially confined LPCMO systems over a wide range of values.

Chapter 8

Electron Beam Induced TMR-like Behaviour in Spatially Confined LPCMO-LAO Thin Films

8.1 Introduction

Spin electronics (spintronics) is based on the engineering of the intrinsic spin of the electron via magnetic moment of the materials. The giant magnetoresistance (GMR) device, which is used as the spin valve of hard disk drive read heads, is one of the most successful applications of the spin-tunneling based techniques. [62, 89, 90] The magnetic tunneling junction (MTJ) or tunneling magnetoresistance (TMR) devices, which are fabricated by multiple layers of ferromagnetic metals that are separated by thin insulating layers, are a candidate for next generation spin based application. A typical structure of TMR device is shown in Fig. 8-1(a); the ferromagnetic metals (Co and CoFe) are separated by a thin insulating layer (Al_2O_3). Since TMR has more sensitive switching field and higher magnitude of MR than GMR devices, the applications based on TMR are expected to perform faster and consume less energy. [62, 64, 91] The TMR between two ferromagnetic layers $i = 1, 2$ separated by a thin insulating layer depends on the relative orientation of the magnetization and the spin polarization $P_i = 2a_i - 1$ where a_i is the fraction of majority-spin-electrons in the density of states of layer i . Then, the TMR is expressed by [92, 93]

$$TMR = \frac{\Delta R}{R} = \frac{R_{\uparrow\downarrow} - R_{\uparrow\uparrow}}{R_{\uparrow\uparrow}} = \frac{2P_i P_j}{1 - P_i P_j} \quad (8.1)$$

where $R_{\uparrow\downarrow}$ and $R_{\uparrow\uparrow}$ are the resistance for antiparallel and parallel magnetization orientation between two magnetic materials, respectively. Fig. 8-1(b) shows a typical TMR behaviour (resistance change vs. field) in the CoFe/ Al_2O_3 /Co magnetic tunnel junction. [92] One can notably see the change in the resistance level depending on the relative orientation of the magnetization in the metallic layers (the arrows in Fig. 8-1(b) indicate the relative magnetization orientation of the FMM layers).

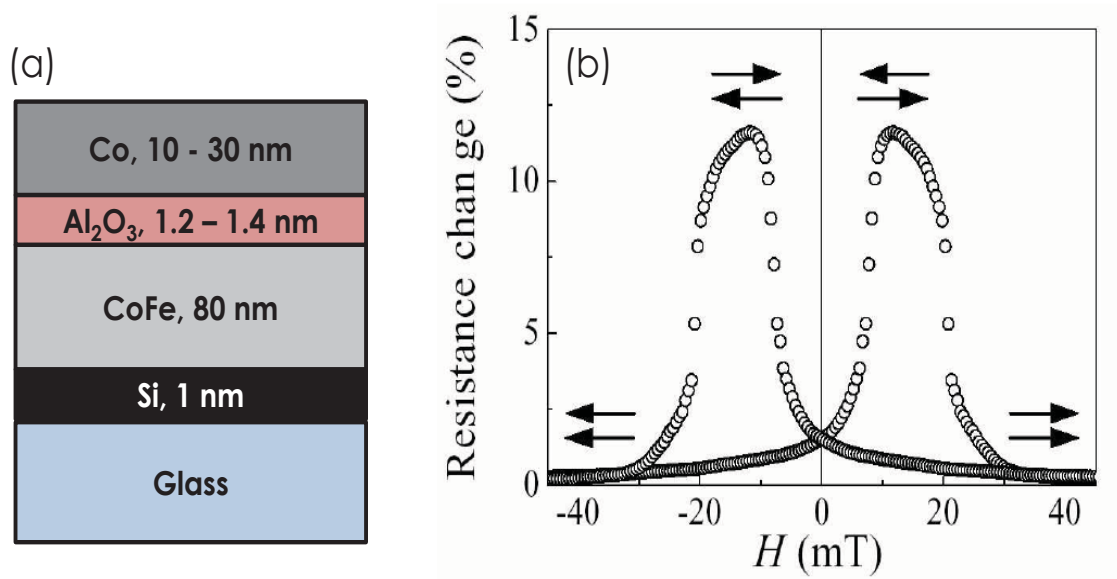


Figure 8.1: (a) A schematic diagram of a typical TMR device. (b) The resistance change vs. magnetic field in the CoFe/Al₂O₃/Co junction at room temperature. The arrows in the figure indicate the relative magnetization orientation of the CoFe and Co layers. [92]

In some manganites it is believed that the spin polarization is close to unity ($P \sim 1$), implying that there is one completely empty spin-split band.

The divalent doped manganite of $\text{La}_{1-x}\text{Di}_x\text{MnO}_3$ with $\text{Di} = \text{Ca}, \text{Sr}, \text{and Ba}$ (especially with $x \sim 0.3$) is of great interest for TMR device applications since many of the devices using these materials exhibit large TMR values (few hundreds percents) due to their half-metallic nature (according to the given definition of TMR, the magnitude can be infinite for half metals ($P = 1$)). [4, 93–100] For example, Ishii et al. have found a TMR value of $\sim 230\%$ at 10 K in $\text{La}_{0.7}\text{Sr}_{0.3}\text{MnO}_3$ (top: 70 unit cells) - LaAlO_3 (1nm) - $\text{La}_{0.7}\text{Sr}_{0.3}\text{MnO}_3$ (bottom: 170 unit cells) where the spin polarization is $\sim 70\%$. [100] Philipp et al. observed TMR value of about 300% at 4.2 K in a $\text{La}_{2/3}\text{Ca}_{1/3}\text{MnO}_3$ - grain boundary - $\text{La}_{2/3}\text{Ca}_{1/3}\text{MnO}_3$ device where the polarization is estimated to be about 77% . [93] In order to achieve low-field induced MR behaviour, it is necessary to fabricate multi-layered structures of these materials (as shown in the above examples where TMR effects occurred at $H < 1$ T). However, the process of fabricating a multi-layered manganite is not trivial since a *dead layer* may intrinsically exist between films' boundaries. [101]

To avoid this difficulty, researchers have also attempted to produce the TMR devices from single layered film with grain boundaries and the results were successful. [93, 97–99] In recent studies, Singh-Bhalla et al. reported intriguing results that intrinsic TMR is seen in spatially confined LPCMO thin film grown on an NdGaO_3 (011) substrate. [11, 102] Their results show about 10% of TMR that is smaller than the few hundreds percents of multi-layered or grain boundary manganites. Although the magnitude is small, it is notable

that TMR can be produced by neighbouring FMM phase domains with thin insulating COI between them. This implies the feasibility of TMR devices by manipulating intrinsic phase domains of EPS manganites. Pr doped La-Ca-Mn-O system has a special advantage for phase domain engineering. As noted in the previous parts of this thesis (e.g. see Chapter 2) the system possesses large-scale ($\sim \mu\text{m}$) intrinsic electronic phase domains [8, 10, 11] and one can conveniently fabricate systems in which the lateral dimensions are similar to the intrinsic domains by conventional photo-lithography techniques. [11, 12, 38, 43, 47–49] In such a spatially confined system, the changes of the status of a small number of phase domains significantly affects the system’s transport properties (as discussed in previous chapters of this thesis). However, due to the random nature of the domain seeding process, artificial manipulation of individual domains within the system can be challenging.

In this chapter, we attempt to artificially manipulate the intrinsic electronic phase domains by using local electron beam scanning. Interestingly, we could create TMR values of $\sim 300\%$ in an e-beam scanned $\text{La}_{0.3}\text{Pr}_{0.4}\text{Ca}_{0.3}\text{MnO}_3$ (LPCMO) microbridge. We believe the electron beam scanning creates a partially ‘bad’ metallic phase which acts as an insulating barrier between adjacent large-scale metallic phase domains. From the investigations, the effective insulating-potential barrier height is found to be $\sim 300\text{ mV}$ since the TMR effect disappears above this bias limit.

8.2 Experimental details

For the study, $\text{La}_{0.3}\text{Pr}_{0.4}\text{Ca}_{0.3}\text{MnO}_3$ (LPCMO) thin films with spatial confinement ($2\ \mu\text{m}$ width) are used. Thin films of LPCMO are deposited on LaAlO_3 substrates by using off-axis d.c. magnetron sputtering techniques. Note that thin films on LAO substrates induce compressive strain between the substrate and LPCMO film. [45, 103, 104] The films are grown in an oxygen-Ar mixture (100 mTorr for oxygen, 20 mTorr for Ar, respectively) at a temperature of 750°C . Then, this was followed by an annealing at 650°C for 3 hours in a pure oxygen filled chamber at atmospheric pressure. When the films are prepared, conventional photo-lithography and chemical wet etching techniques are used to fabricate micrometer-wide bridges in order to achieve spatial confinement (see detailed process in Chapter 3). Ag electrodes are deposited on top of the samples. Then the transport measurements are achieved by using the 4-pt probe method. The measurement system consists of AC/DC current sources (Keithley 6221), nanovoltmeters (Keithley 2182A), and sourcemeters (Keithley 2410). All the measurements are monitored and controlled by home-built LabView drivers. The electron beam scanning was achieved by using a commercial scanning electron beam microscopy (SEM) device (Tescan Vega-3 SEM with EDX). The beam width of the electron beam was $\sim 70\text{ nm}$ at an acceleration voltage of 20 kV .

8.3 Results and discussion

The effect of e-beam scanning is shown in Fig. 8-2(a)-(c). From comparison of the SEM images before and after e-beam scanning, carbon contamination was observed after e-beam scanning (dark line in the middle of the bridge, Fig. 8-2(b)). The AFM image of the sample after the e-beam scanning shows that the sample was not physically damaged by the e-beam but the existence of carbon contamination was confirmed (spikes on the sample). The carbon contamination is unavoidable unless the chamber is perfectly vacuumed. We believe the carbon contamination does not affect the transport properties of the manganite (acts as insulating powders on top of the sample).

The temperature dependences of the resistance (R vs. T) are shown in Fig. 8-3(b) for different states of the sample. The as-grown sample shows insulating behaviour at low temperature caused by a deficiency of oxygen in the LPCMO system. In order to have a system with more optimum oxygen distribution [105], the sample was annealed in the air at 750°C for 3 hours. Then, conventional R vs. T behaviour is achieved with a metal-to-insulator phase transition at ~ 128 K. Note that this sample did not show percolation induced resistance jumps, a general sign of spatial confinement, after the post-annealing process. The observation that this sample shows 'wide' LPCMO film-like behaviour indicates the effective size of the electronic phase separation could be in the sub-micrometer range (smaller than $2 \mu\text{m}$).

Now, in an attempt to produce artificial domain separation within the system, an electron beam was scanned across the bridge, as schematically shown in Fig. 8-3(a). For the scanning, the acceleration voltage of the electron beam was fixed at 20 kV with beam width of ~ 70 nm. Interestingly, after the electron beam scanning, a noticeable change in the transport was detected in the temperature dependence of the resistance profile. As shown in Fig. 8-3(b), a small shift of the T_{MIT} (from 128 K to 124 K) and percolative resistance jumps are detected after the e-beam scanning. This effect could be caused by a disturbance of the metallic domain configuration due to the e-beam. When the e-beam scans across the LPCMO microbridge, the electrons could cause dislocation of oxygen. Recall that the Mn - O - Mn bond angle is critical for the conductance of manganite, e.g., by the double exchange interaction where the hopping amplitude is proportional to the bond angle, i.e., $t_{ij} \propto \cos(\theta_{ij}/2)$ (see Chapter 2). Therefore, the dislocation (wider bond angle) of O causes a 'bad' metallic region in the system at temperatures below the T_{MIT} . However, this 'bad' metallic behaviour seems to occur only within the temperature range where small resistance jumps are occurring (this will be discussed later in this chapter). Outside of the temperature range where resistance jumps occur, the temperature dependent transport shows similar behaviour as before e-beam scanning.

The most notable feature in this e-beam scanned sample is that the system exhibits TMR-like transport behaviour within the temperature range in which percolative resistance jumps exist. Fig. 8-4(a) shows the isothermal resistance change during the sweeping of the

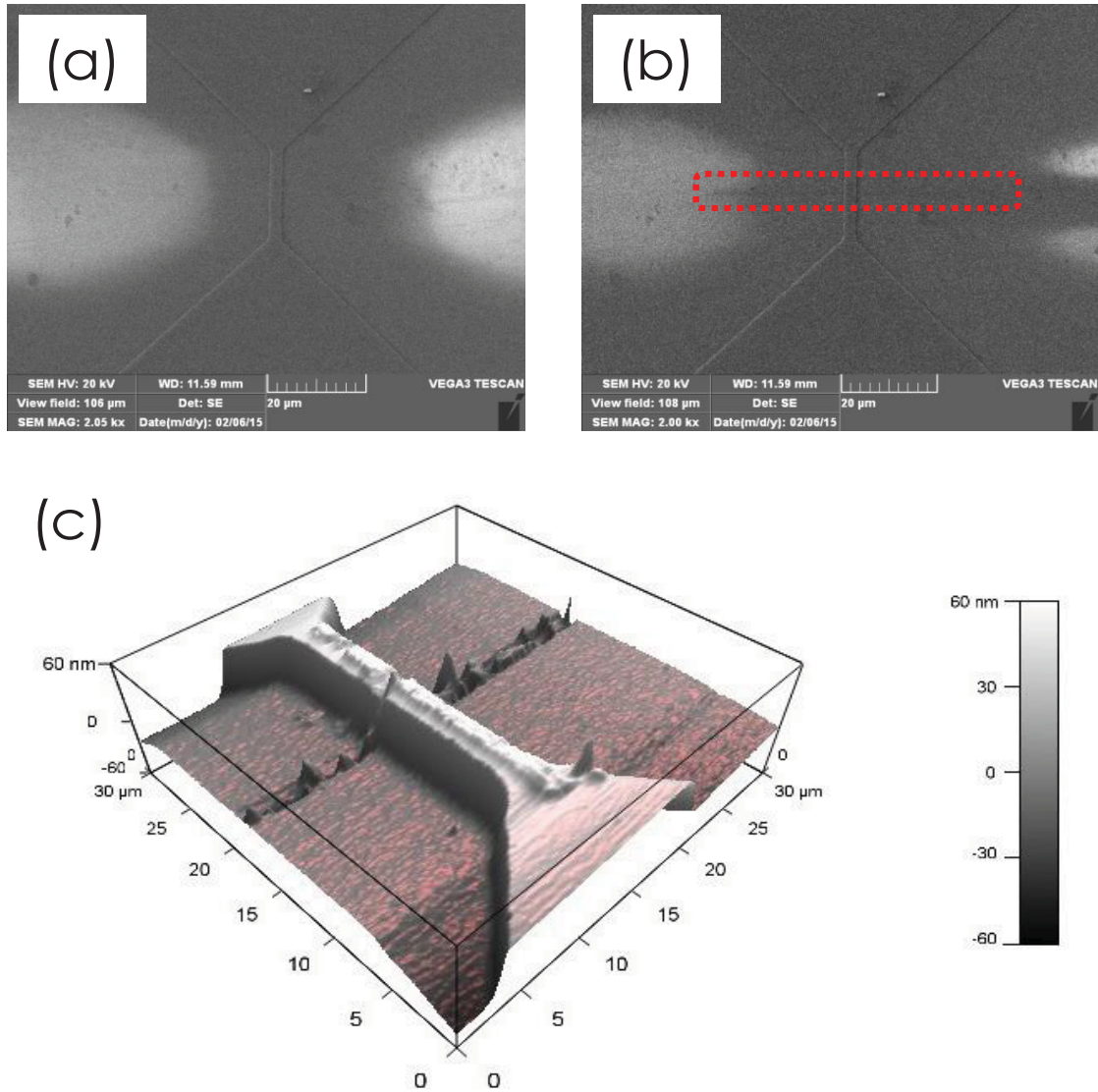


Figure 8.2: (a) SEM image of the sample before scanning the electron beam. (b) SEM image of the sample after e-beam scanning; dark colored line (in the red rectangle) is induced by carbon deposit during the e-beam scanning. Note that white dots in SEM images are due to charging effect in the insulating substrate. (c) AFM image of the sample after e-beam scanning.

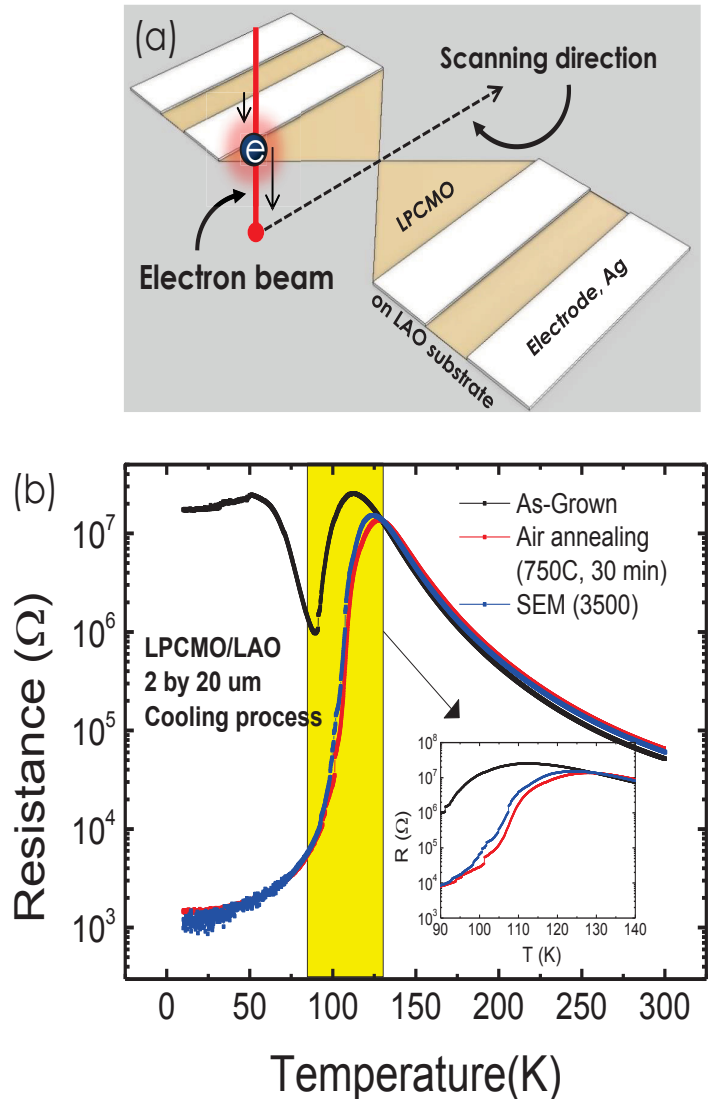


Figure 8.3: (a) A schematic illustration of e-beam scanning across the microbridge sample. (b) The temperature dependence of the resistance in a spatially confined LPCMO/LAO sample in the as-grown state, post-annealed state, and e-beam scanned state.

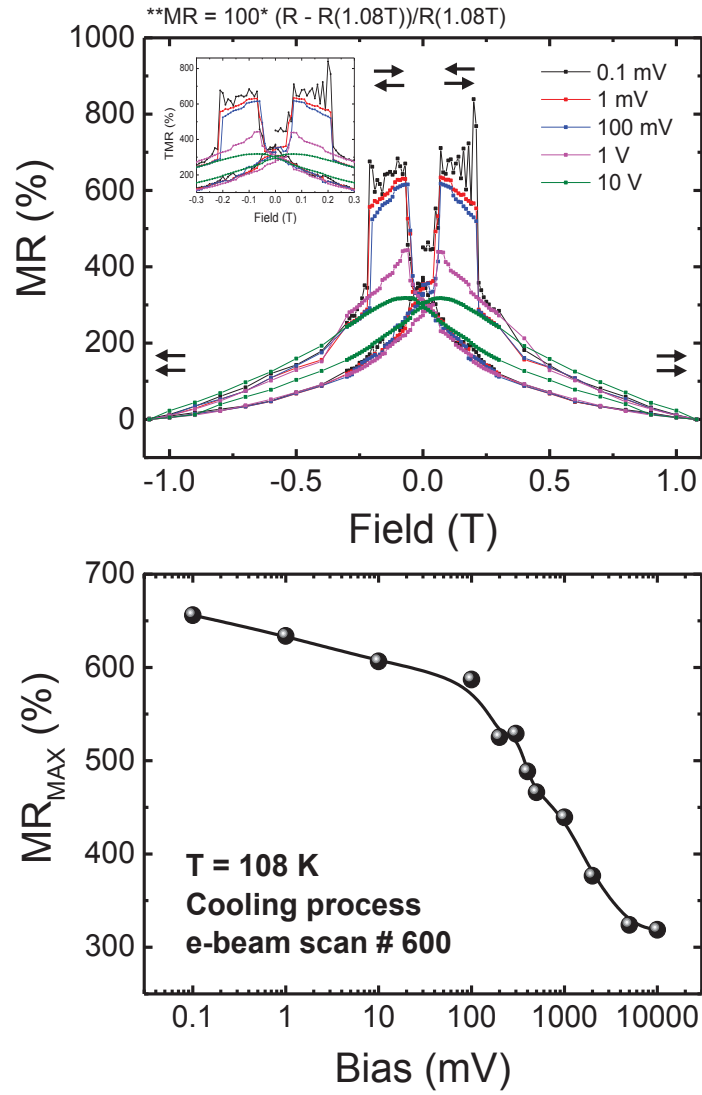


Figure 8.4: (a) The bias voltage dependence of the resistance vs. external magnetic field at 108 K in 600 e-beam scanned LPCMO/LAO microbridge. The arrows indicate the relative magnetization orientation in adjacent metallic domains. (b) Maximum MR magnitude vs. bias voltage curve.

magnetic field (MR vs. H) at various bias voltages (also see Fig. 8-1(b) for the comparison). The measurement was performed after 600 scans of the e-beam. One can clearly see the evidence of the tunneling magnetoresistance (TMR) effect from the shape of R vs H profile while no TMR-like behaviour is observed before e-beam scanning. In order to confirm the reproducibility of the TMR-like behaviour, the measurement was performed 5 times with thermal reset (heated to 300 K then cooled to a set temperature (108 K) at zero field) to reset the phase distribution within the sample. The TMR-like behaviour was repeatable in every measurement at low bias voltages (< 0.5 V). The arrows in Fig. 8-4(a) indicate the possible configuration of adjacent metallic domains' relative magnetization orientation. From the bias dependence of the MR, a significant drop of the MR magnitude is found at ≥ 300 mV. Above this bias, the TMR-like behaviour disappears and the data behave as in normal manganite films (Fig. 8-4(b)). At this high bias voltage, the tunneling probability of the electrons through the insulating layer increases and hence the TMR value decreases.

Now, we would like to discuss why TMR-like behaviour is observable in an e-beam scanned LPCMO microbridge. In an electronic phase separated (EPS) LPCMO system, metallic domains are randomly seeding within the insulating phase background at temperatures near the metal-to-insulator phase transition temperature (Fig. 8-5(a)). As the temperature of the system decreases the metallic domains grow in volume and percolate between neighbouring domains (Fig. 8-5(b-d)). Hence the resistance drops at temperatures below the T_{MIT} . In a spatially confined system, the percolation event is observable as a sharp jump since the system can be occupied by limited numbers of phase domains. In our sample ($2 \mu\text{m}$ width), this signature was not observed before the sample was exposed to the e-beam scanning. However when the e-beam was scanned across the sample, as described above, the scanning can produce a "damaged" region that hampers the growth of metallic domains. As a result, this process can form FMM - I (or bad FMM) - FMM arrangement where TMR behaviour is expected depending on the relative orientations of magnetization of each metallic domain (assuming that each FM domain has slightly different coercivity field; Fig. 8-5(e-i)). In this sample, the easy axis of magnetization can be formed along the e-beam path due to domain-wall pinning at the exposed region. [93] Since the magnetic field is applied along the e-beam path (insulating barrier, IB), i.e., $H \parallel IB$, the resistance versus field $R(H)$, can be in a low or high resistance state depending on whether the magnetization directions in adjacent FMM domains are parallel or antiparallel. This is explained in Fig. 8-5(g-i). Furthermore, additional magnetoresistance (after magnetization alignment where sharp drop of the resistance is shown) can be observed in the LPCMO system due to further growth of FMM domains upon the application of an external magnetic field. As the temperature cools this 'bad metal' region eventually collapses and percolate with neighbouring metallic domains which can be observed in R vs T profiles (at low temperature; Fig. 8-5(f)). This phenomenological explanation is illustrated in Fig. 8-5(a to f). Note that the shapes of the phase domains are illustrated according to direct images of LPCMO systems. [8, 10]

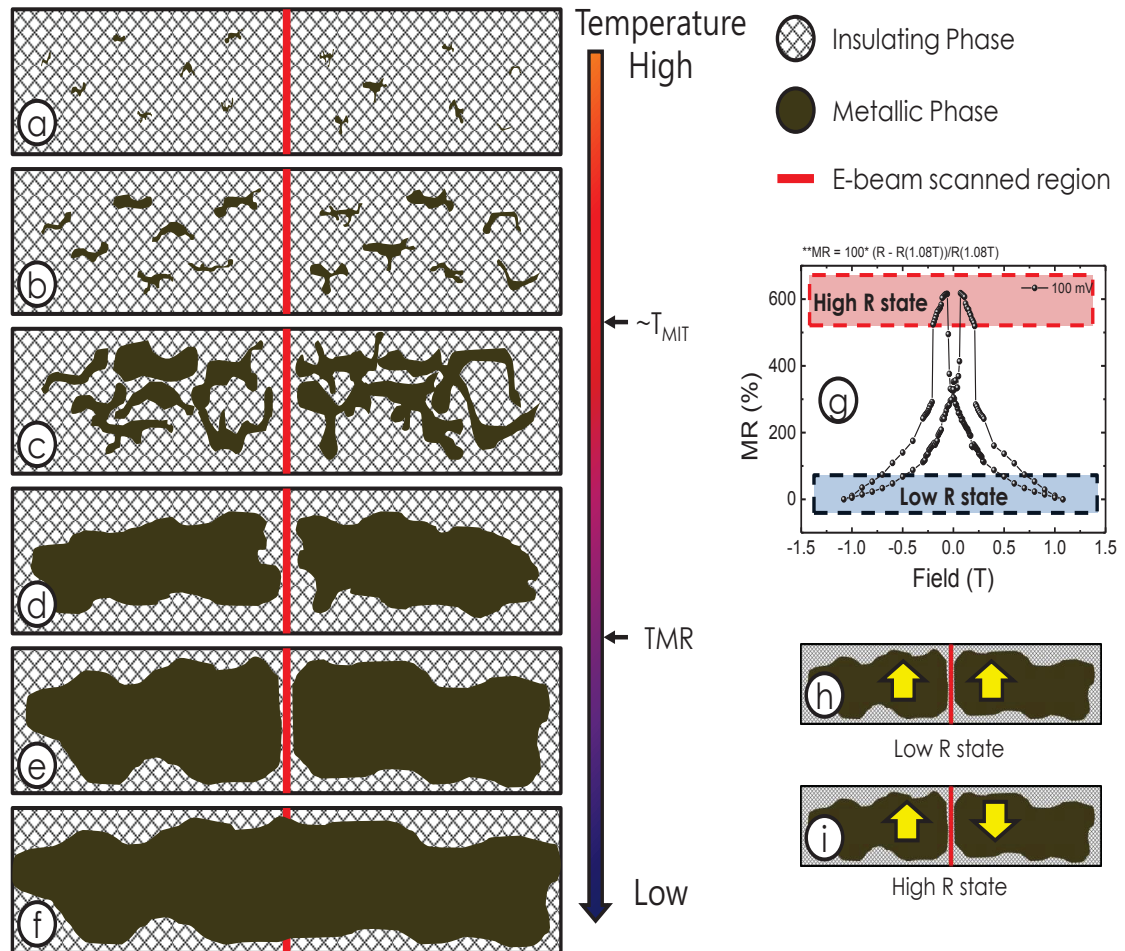


Figure 8.5: Phenomenological model of e-beam induced TMR-like behaviour in a spatially confined EPS LPCMO/LAO thin film. (a-f) Temperature dependence of phase domain configuration in e-beam induced microbridge. (g) TMR behaviour and the relative magnetization configuration of metallic phase domains at (h) low R level and (i) high R level, respectively. Note that the arrows in (h) and (i) indicate the orientation of the magnetization in the metallic domains

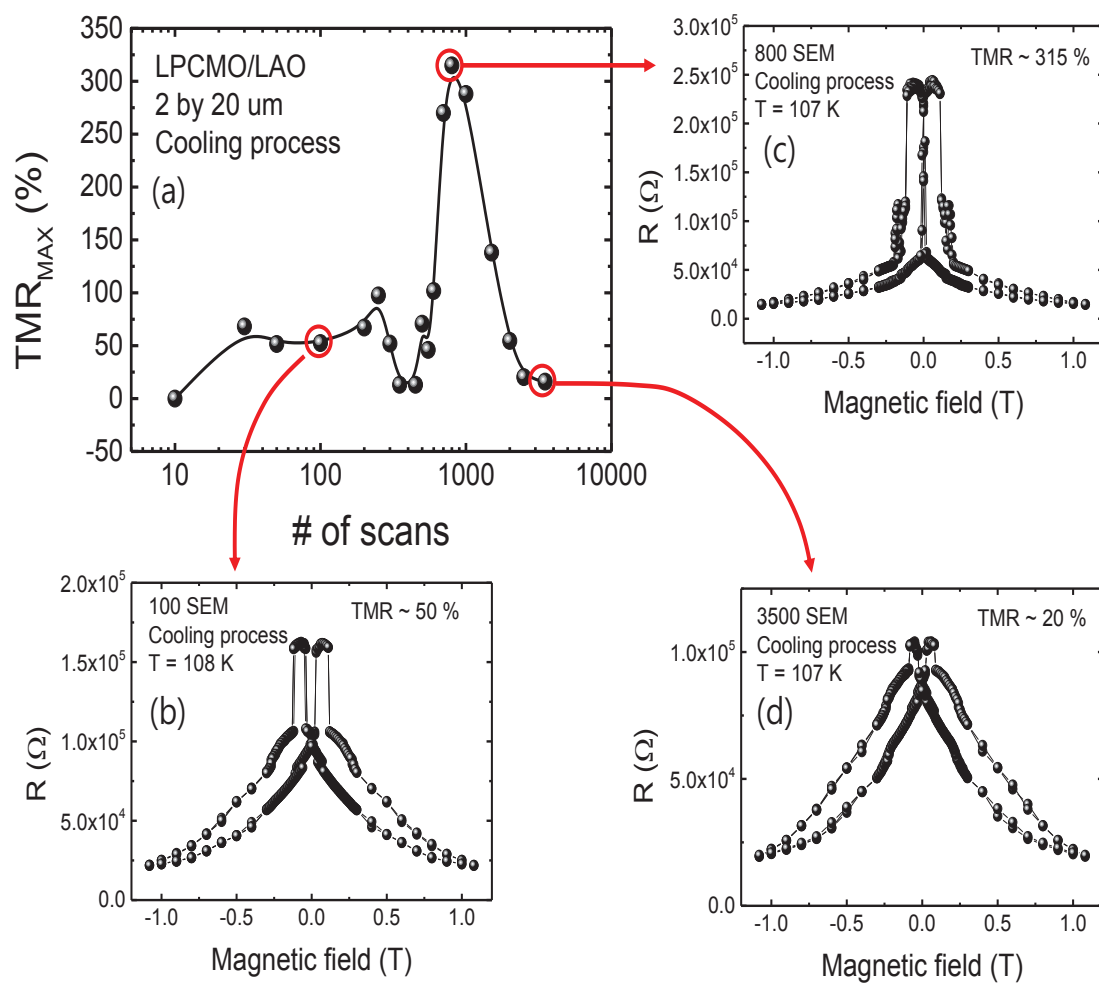


Figure 8.6: (a) E-beam scan number vs. maximum TMR curve; a peak was observed at scan number 800. R vs. H curve (b) at scan number 100, (c) at scan number 800, and (d) at scan number 3,500, respectively.

In order to further understand the role of the e-beam scanning, we attempted to investigate the maximum TMR magnitude as a function of the number of e-beam scans. Here, the maximum TMR magnitude is calculated by $TMR = [R(\max) - R(0T)]/R(0T)$, where $R(\max)$ and $R(0T)$ are the resistance values at maximum and at $H = 0$ T during field sweeping, respectively. For the experiment, the scanning rate was fixed at $\sim 0.6/s$. As the number of scans increases, the TMR_{MAX} magnitude stays somewhat constant, then increases sharply (Fig. 8-6(b)) and peaks at ~ 800 scans with $\sim 300\%$ of TMR (Fig. 8-6(c)). The TMR_{MAX} is small when the number of scans reaches a few thousand.

Initially increasing the number of scans could produce a progressively more damaged region in the sample that further inhibits the formation of the metallic region within the system. The damaged region (i.e., bad FMM) acts as a potential barrier between the metallic domains. Upon increasing the number of e-beam scans, the height of the potential barrier increases until it reaches an optimum value which corresponds to the highest TMR magnitude ($\sim 300\%$ at 800 scans, Fig. 8-6(a) and (c)). Further increasing the number of scans continues to increase the barrier height (more insulating) until it is too high to be tunneled through. As a result, one observes the decrease in the TMR magnitude above ~ 1000 scans (see Fig. 8-6(a) and (d)). Experimentally, the potential barrier (bad metallic region) produced by the e-beam scanning does not seem to noticeably disturb the R vs. T profile (no clear change is observed above 200 scans).

There is some variation in the e-beam induced behaviour among different samples. This variation could be due to the inhomogeneous initial state of the phase separated system, i.e., each sample may have a different distribution of oxygen content which leads to a different domain distribution between samples. This problem might be solvable by precise control of the post annealing process. Nevertheless, the e-beam induced TMR behaviour was in fact observed in several different samples (with different magnitudes at different temperatures). Also we would like to note that this TMR-like behaviour was observed only with the LPCMO films on $LaAlO_3$ (LAO) substrates which creates compressive strain between the substrate and film. We believe that the compressive strain may help to develop the domain walls within the electron beam exposed region.

8.4 Conclusion

In conclusion, we could artificially generate a FM - I - FM domain structure by e-beam scanning within a spatially confined system. When the e-beam is scanned across the LPCMO bridge, the system has shown TMR-like behaviour which is evidence for the existence of a FM - I - FM configuration within the bridge that enables tunneling between the FM regions. We believe e-beam scanning in a manganite could tilt the angle between the Mn - O - Mn bond which may induce a 'bad' metallic region that acts as a potential insulating barrier. By increasing the number of e-beam scans, a maximum of $\sim 300\%$ TMR is observed. This magnitude is reasonably high compared to the TMR magnitude from multi-layered man-

ganites (few % to hundreds %). However, when the number of e-beam scans is increased above ~ 1000 a decrease of the magnitude of the TMR is observed. This could be caused by the progressive increase of the barrier height as the number of e-beam scans increases. These findings may help us to better engineer phase domains in EPS systems which are strong candidates for future generation magnetic sensor applications.

Chapter 9

Summary, Conclusions and Directions for Future Works

In this thesis, we have presented novel magneto-transport properties in spatially confined $\text{La}_{0.3}\text{Pr}_{0.4}\text{Ca}_{0.3}\text{MnO}_3$ (LPCMO) thin films. Chapter 9.1 to 9.5 summarizes the major results from Chapter 4 to 8. In Chapter 9.6, I discuss directions for future works.

9.1 Re-entrant low-field magneto-resistance in LPCMO film due to spatial confinement

From investigations of the temperature and external magnetic field dependence of the resistance in a spatially confined LPCMO $2\ \mu\text{m}$ width micro-bridge, we find that the sudden jumps that are produced by the percolation of metallic domains within the confined region produce additional features in its magnetoresistance. Two peaks are seen in the temperature dependence of the magnetoresistance as well as the temperature dependence of the area of the hysteresis loops that exist in an isothermal magnetic field scan of the resistance in $2\ \mu\text{m}$ bridge. One of the peaks is close to the metal-insulator transition temperature, as expected for a standard manganite film, while the additional peak occurs at lower temperatures where co-existing metallic and insulating domains have sizes comparable to the spatially confined region. The magnetoresistance of the latter peak is considerably less sensitive to magnetic field than the former. Furthermore, its value at 0.2 T is enhanced by about 100 % compared to that of the $25\ \mu\text{m}$ bridge at the same temperature and field. These results imply that the LF-CMR devices are feasible by using the spatial confinement phenomena.

9.2 Field dependent resistive evolution in spatially confined LPCMO thin films

For understanding of the long-time resistive metastability in spatially confined thin films of $\text{La}_{0.3}\text{Pr}_{0.4}\text{Ca}_{0.3}\text{MnO}_3$, we have systematically investigated the temperature and magnetic

field dependence of resistive time relaxation behaviour. It is found that the sharp resistance jumps during time relaxation measurements occur in the temperature range where the sizes of the competing electronic phase domains are comparable to the lateral dimension(s) of the LPCMO film, such as in the $2\ \mu\text{m} \times 2\ \mu\text{m}$ microbridge.

These resistance jumps could be tuned by the magnetic field: (1) at low (or zero) magnetic fields, FMM domains can disjoin as the FMM volume decreases. This can disconnect a percolation path(s) within the confined part of the sample, creating the up jumps of the resistance superimposed upon an overall increase of the R vs. time. (2) At high magnetic fields, there is an overall growth of the volume of the FMM domains with time. This can create a percolation path(s) within the microbridge, resulting in downward jumps of the resistance superimposed upon an overall decrease of the R vs. time. (3) At a certain magnetic field (~ 0.4 T in our sample), the long-time resistance relaxation as well as the sharp jumps are suppressed because the average FMM and insulating volumes are time-independent. By contrast to the behaviour described above for the $2\ \mu\text{m}$ wide microbridge, the $25\ \mu\text{m}$ wide bridge shows only relatively weak resistance jumps within the field range studied. This sample is approaching the non-confined limit (behaves as a wide sample) at all temperatures and magnetic fields, where many percolating paths contribute to the behaviour of the resistance. We believe such information is useful for improving the scientific understanding of the metastability of a spatially confined manganite system over a broad range of external magnetic field and temperature, and may also have ramifications for single domain phase engineering for applications.

9.3 Low field colossal anisotropic magnetoresistance in spatially confined electronically phase separated LPCMO microbridges

The anisotropic magnetoresistance (AMR), i.e., the values of the resistance that depend on the direction of the magnetic field with respect to either the current direction or the crystal axes, is an important property for various applications, such as sensors of magnetic field directions. For the applications, it is known that the data rate of those devices is proportional to the square of the magnitude of the MR or AMR. For this reason, having a high value of the AMR improves the detectors' sensitivity and the corresponding read times, etc. By manipulating the geometries of LPCMO thin films, we could create colossal low field (~ 0.2 T) in-plane anisotropic magnetoresistance (C-AMR) greater than 16,000 %. This magnitude is a record-breaking value of the AMR which is several orders of magnitude greater than quantities previously reported in any material (e.g., $\sim 5\%$ to $\sim 20\%$ in ferromagnetic 3d alloys and $\sim 40\%$ and $\sim 200\%$ in normal wide manganite films). We believe this enormously large magnitude of AMR (C-AMR) could be caused by the domains which are trapped/pinned in certain directions; the ones that follow the domain growth preferred direction and the other ones that are perpendicular to the domain growth preferred

direction. This study may be propaedeutic to a way of enhancing the anisotropic magnetotransport properties in manganite systems. Our discovery of such colossal AMR will improve the scientific understanding of the electrical properties of these unique systems, and can also provide important clues on engineering next generation AMR-based devices for technology.

9.4 Current dependence of colossal anisotropic magnetoresistance in LPCMO microbridges

The discovery of C-AMR behaviour in spatially confined $\text{La}_{0.3}\text{Pr}_{0.4}\text{Ca}_{0.3}\text{MnO}_3$ thin films inspired us to seek methods of manipulating the C-AMR magnitude. Using the knowledge that applying an electric current to an EPS manganite system can change the activity of the domains, one may expect that the current can significantly modify the C-AMR within a spatially confined LPCMO microbridge. We found that by using the bias d.c. current to change the percolation within spatially confined LPCMO thin films, the magnitude of the colossal in-plane anisotropic magnetoresistance could be dramatically modified. As an example, the low field anisotropic magnetoresistance value was changed from $\sim 900\%$ to over $\sim 24,000\%$ as the current is decreased from $1\ \mu\text{A}$ to $10\ \text{nA}$. From the results of the C-AMR on the bias current dependence, it appears that when a higher current is applied to our sample within the temperature region where the percolation induced resistance jumps occur, the system prefers to be in a more metallic configuration. These results indicate that the d.c. bias current can be a useful method for adjusting the C-AMR in spatially confined LPCMO systems over a wide range of values.

9.5 Electron beam induced TMR-like behaviour in spatially confined LPCMO-LAO thin films

By considering the fact that the manipulation of the electronic phase domains within the confined LPCMO system can cause significant changes in electric transport properties, it is desirable to develop a novel device such as magnetic tunnel junctions by engineering the phase domains in this system. As a demonstration of feasibility, we have used an electron beam to engineer the properties of electronic phase domains within a spatially confined LPCMO system. We could artificially generate a FM - I - FM domain structure by e-beam scanning within the spatially confined system and generate tunneling magnetoresistance (TMR) behaviour with a magnitude of $\sim 300\%$. This finding may lead to a new method of manipulating phase domains in EPS systems which are strong candidates for future generation magnetic sensor applications.

9.6 Directions for future works

The experimental works presented in this thesis have been focused on the percolation induced magneto-transport properties in spatially confined $\text{La}_{0.3}\text{Pr}_{0.4}\text{Ca}_{0.3}\text{MnO}_3$ thin films. Although interesting features such as double peak MR, C-AMR, and e-beam induced TMR have been found in this system, more works remain. In the following sections, the author would like to introduce directions for future works regarding not only further understanding of the system's nature but also the engineering of phase domains within micrometer-scale EPS manganites.

9.6.1 Reproducibility of spatial confinement induced transport properties

During the study of micrometer-scale EPS LPCMO thin films, reproducibility of the results in spatially confined thin films was one of the main issues. The following feature may be important for the un-controllable nature of spatial confinement: Oxygen distribution within the system could cause significant changes in transport properties in the spatially confined systems (see Chapter 6). As the double exchange model explains, the electron hopping in manganite occurs through the oxygen atoms between manganese atoms (see Chapter 2). A non-uniform distribution of oxygen, therefore, would create an inhomogeneous hopping environment that may cause 'bad' metallic portions within the sample. In wide (or normal) thin films of LPCMO (lateral width above 20 micrometers), this inhomogeneity would not noticeably affect the system's transport properties since many conduction paths can be created within the films. However, since the spatially confined system contains small numbers of conduction paths, the overall effect due to the disturbance (caused by non-uniform distribution of oxygen) in a single conduction path can cause a significant effect in the transport properties. Hence controlling the oxygen-distribution in a confined sample can be used to manipulate the confinement phenomenon (resistance jumps) in these samples. As a possible way of achieving this goal, post-annealing in Ar or air flowing condition can be attempted. The microbridges can show insulating or normal film-like behaviour that depends on the oxygen distribution of the sample. When the bridge part of the sample contains a low level of oxygen, insulating behaviour is expected while a high level of oxygen content would cause normal film-like behaviour. For insulating microbridges, post annealing in air can add the oxygen into the system, hence metallic phase transition is expected. For normal film-like microbridges, post annealing in Ar gas can deprive oxygen from the sample and create disturbances in the metallic phase. We have partially started this project and the results seem promising for engineering the magnitude of percolation jumps via a gentle post annealing process. Fig. 9-1(a) and (b) show the results of post annealing effect in air and Ar, respectively. In future studies, precise measurement and control of oxygen-distribution would be required.

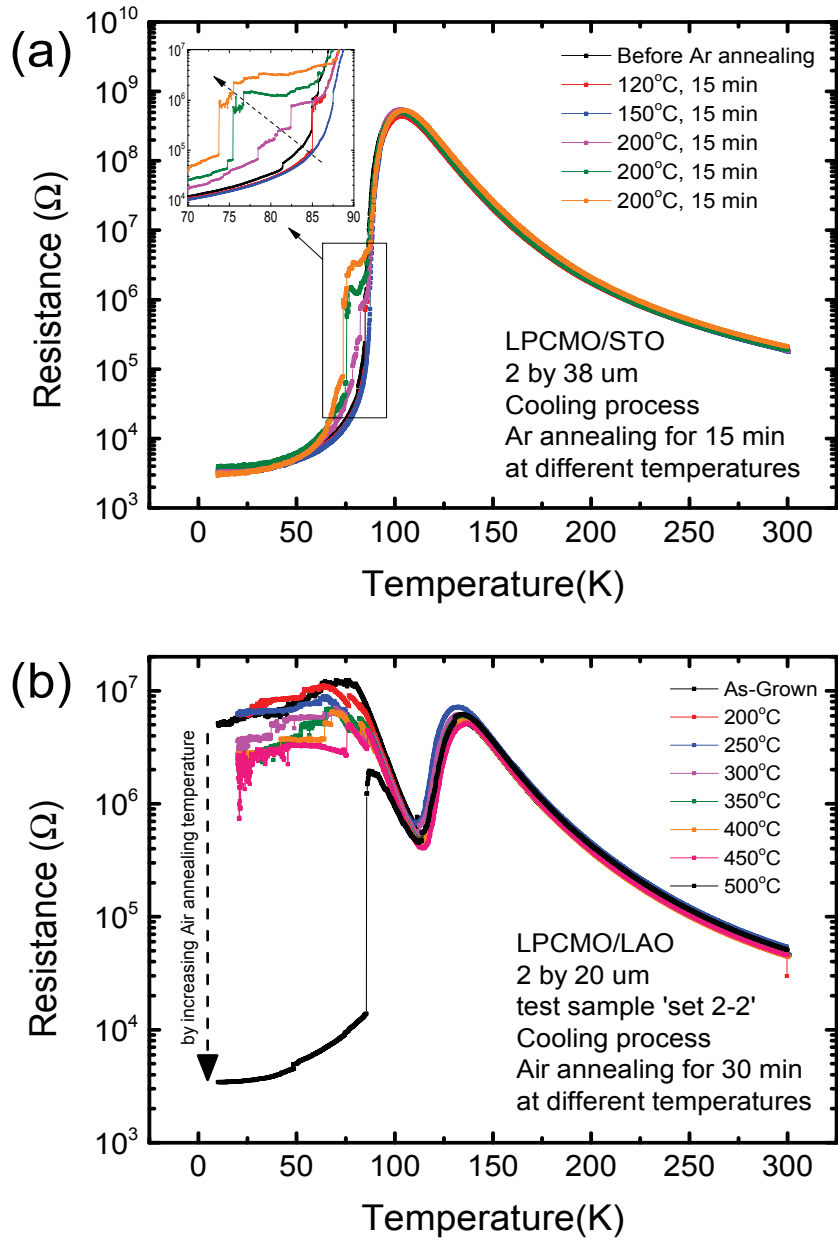


Figure 9.1: Post annealing effect in spatially confined LPCMO films in (a) Ar gas flowing condition: annealing for 15 min at different temperatures and (b) air flowing condition: annealing for 30 min at different temperatures

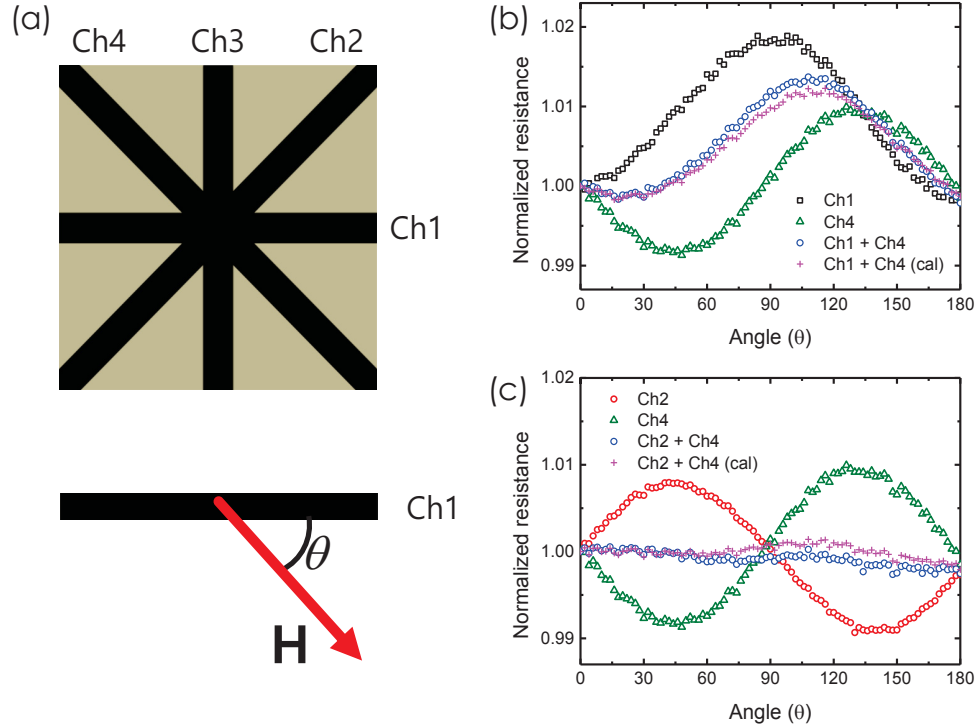


Figure 9.2: The study of AMR manipulation by combination of bridges with different angles (a) A schematic diagram of the sample (LPCMO thin film on STO substrate). (b) AMR result obtained from the combination of Ch1 and Ch4 and (c) combination of Ch2 and Ch4, respectively. Note that (cal)s in (b) and (c) denote the values calculated using data from Ch1 and Ch4 for (b) (and Ch2 and Ch4 for (c)), e.g., $\text{Ch1} + \text{Ch4} (\text{cal}) = 1/2(\text{Ch1}) + 1/2(\text{Ch4})$.

9.6.2 Geometrical engineering of spatial confinement for AMR manipulation (anisotropic strain induced effects)

The discovery of colossal anisotropic magnetoresistance in spatially confined LPCMO thin films is an important finding in this thesis. It shows that a novel method of achieving large magnitude of AMR is to manipulate the geometry of the sample. In normal wide films, the spin-orbit coupling has been accepted as a main mechanism for their AMR behaviour. The conventional AMR is proportional to $\cos^2 \theta$ or $\sin^2 \theta$ where θ is the angle between the magnetization and current direction. Therefore, one can manipulate the peaks of the AMR behaviour by choosing the right combination of bridges with different angles. For example, two bridges that are perpendicular to each other will show no AMR. By studying a cross junction pattern, we could experimentally manipulate the AMR values, as exemplified in Fig. 9-2.

Therefore, in principle, many shapes of AMR response can be achieved by manipulating the combinations of the bridges with different angles. Furthermore, when the system's lateral dimension is reduced to micrometer range, resistance jumps can be seen in

micrometer-scale phase separated systems such as LPCMO thin films. From our results (shown in Chapters 6 and 7), it is suggested that the anisotropic nature of metallic domain growth in confined LPCMO thin films could lead to the C-AMR behaviour. In this percolative environment, the system will not follow the conventional $\cos^2 \theta$ or $\sin^2 \theta$ relation due to the existence of resistance jumps. In these spatially confined samples, manipulating the orientation of the metallic domain growth can be used for engineering the C-AMR. For example, a NGO substrate with (101) crystalline orientation creates anisotropic strain between the film and the substrate which cause anisotropic phase domain growth in the LPCMO system. Therefore, by choosing appropriate geometries of spatially confined thin films on this anisotropic strained substrate, dramatic changes in the C-AMR is expected.

9.6.3 Further understanding of electron beam scanning effect on electronic phase separated manganites

Our discovery of tunneling magneto-resistance (TMR) behaviour in electron-beam scanned microbridges have opened a door to developing a new type of magnetic tunnel junction (MTJ) devices by engineering the local phase domains in a manganite. Although we have observed promising results in a few samples, the exact nature of the phenomenon remains unclear. For further understanding of this system, direct imaging techniques such as magnetic force microscopy (MFM) and surface magneto-optics kerr effect (SMOKE) microscopy are desirable to 'see' the structure of the electronic phase domains. Note that due to its fast phase-transition dynamics, we would prefer an optical method (SMOKE) to get 'real-time' response of the phase domains within the confined EPS systems. Furthermore, by considering the fact that the e-beam induces regions with 'bad' metallic behaviour, one might be able to use the e-beam to pattern the conduction path or even create multiple tunnel junctions within a wide sample without physically, e.g., chemically, removing the undesirable regions.

Bibliography

- [1] E. Dagotto, *Science* **309**, 257 (2005).
- [2] E. Dagotto, T. Hotta, and A. Moreo, *Physics reports* **344**, 1 (2001).
- [3] A. Machida, Y. Moritomo, E. Nishibori, M. Takata, M. Sakata, K. Ohoyama, S. Mori, N. Yamamoto, and A. Nakamura, *Phys. Rev. B.* **62**, 3883 (2000).
- [4] A. P. Ramirez, *J. Phys.: Condens. Matter* **9**, 8171 (1997).
- [5] A. J. Millis, *Nature* **392**, 147 (1998).
- [6] K. H. Ahn, T. Lookman, and A. R. Bishop, *Nature* **428**, 401 (2004).
- [7] M. Zheng, X. Y. Li, M. Yang, Q. X. Zhu, Y. Wang, X. M. Li, X. Shi, H. Li, X. Shi, H. L. W. Chan, X. G. Li, H. S. Luo, and R. K. Zheng, *Appl. Phys. Lett.* **103**, 263507 (2013).
- [8] M. Uehara, S. Mori, C. H. Chen, and S.-W. Cheong, *Nature* **399**, 560 (1999).
- [9] Y. Murakami, H. Kasai, J. J. Kim, S. Mamishin, D. Shindo, S. Mori, and A. Tonomura, *Nature Nanotech.* **5**, 37 (2010).
- [10] L. Zhang, C. Israel, A. Biswas, R. L. Greene, A. de Lozanne, *Science* **298**, 805 (2002).
- [11] G. Singh-Bhalla, A. Biswas, and A. F. Hebard, *Phys. Rev. B.* **80**, 144410 (2009).
- [12] H. Zhai, J. X. Ma, D. T. Gillaspie, X. G. Zhang, T. Z. Ward, E. W. Plummer, and J. Shen, *Phys. Rev. Lett.* **97**, 167201 (2006).
- [13] T. Wu and J. F. Mitchell, *Phys. Rev. B.* **74**, 214423 (2006).
- [14] T. Z. Ward, Z. Gai, H. W. Gio, L. F. Yin, and J. Shen, *Phys. Rev. B* **83**, 123123 (2011).
- [15] T. R. McGuire, R. I. Potter, *IEEE Trans. Mag.* **MAG-11**, 1018 (1975).
- [16] J. Chen, W. Wei, K. Zhang, K. Du, Y. Zhu, H. Liu, L. Yin, and J. Shen, *Appl. Phys. Lett.* **104**, 242405 (2014).

- [17] M. Egilmez, M. M Saber, A. I. Mansour, R.-C. Ma, K. H. Chow, and J. Jung, Appl. Phys. Lett. **93**, 182505 (2008).
- [18] M. Egilmez, K. H. Chow, and J. Jung, Mod. Phys. Lett. B. **25**, 697 (2011).
- [19] V. Kiryukhin, B. G. Kim, V. Podzorov, S.-W. Cheong, T. Y. Koo, I. Moon, and Y. H. Jeong, Phys. Rev. B. **63**, 024420 (2000).
- [20] Y. Tokura, Rep. Prog. Phys. **69**, 797 (2006).
- [21] G. H. Jonker and J. H. van Stan, Physica **16**, 337 (1950).
- [22] C. Zener, Phys. Rev. **81**, 440 (1951).
- [23] A. Gössling, M. W. Haverkort, M. Benomar, H. Wu, D. Senff, T. Möller, M. Braden, J. A. Mydosh, and M. Grüninger, Phys. Rev. B **77**, 035109 (2008).
- [24] K. Rościszewski, and A. M. Oleś, Acta. Phys. Pol. A **115**, 107 (2009).
- [25] E. Dagotto, *Nanoscale Phase Separation and Colossal Magnetoresistance*, 1st ed. (Springer, 2002).
- [26] S. Blundell, *Magnetism in Condensed Matter*, 1st ed. (Oxford University Press, 2001).
- [27] Y. Tokura, and Y. Tomioka, J. Magn. Magn. Mat. **200**, 1 (1999).
- [28] P. W. Anderson and H. Hasegawa, Phys. Rev. **100**, 67 (1955).
- [29] Y. Tokura, *Colossal magneto-resistive oxides*, 1st ed. (Gordon and Breach, 2001).
- [30] A. J. Millis, P. B. Littlewood, and B. I. Shraiman, Phys. Rev. Lett. **74**, 5144 (1995).
- [31] M. J. Calderón, and L. Brey, Phys. Rev. B **58**, 3286 (1998).
- [32] M. J. Calderón, J. A. Vergés, and L. Brey, Phys. Rev. B **59**, 4170 (1999).
- [33] J. B. Goodenough, Phys. Rev. **100**, 564 (1955).
- [34] V. Podzorov, M. E. Gershenson, M. Uehara, and S-W. Cheong, Phys. Rev. B. **64**, 115113 (2001).
- [35] R. von Helmolt, J. Wecker, B. Holzapfel, L. Schultz, and K. Samwer, Phys. Rev. Lett. **71**, 2331 (1993).
- [36] S. Jin, T. H. Tiefel, M. McCormark, R. A. Fastnacht, R. Ramesh, and L. H. Chen, Science **264**, 413 (1994).
- [37] P. G. Radaelli, R. M. Ibberson, D. N. Argyriou, H. Casalta, K. H. Andersen, S.-W. Cheong, and J. F. Mitchell, Phys. Rev. B. **63** 172419 (2001).

- [38] Y. Yanagisawa, H. Tanaka, T. Kawai, and L. Pellegrino, *Appl. Phys. Lett.* **89** 253121 (2006).
- [39] P. Levy, F. Parisi, M. Quintero, L. Granja, J. Curiale, J. Sacanell, G. Leyva, G. Polla, R. S. Freitas, and L. Ghivelder, *Phys. Rev. B.* **65** 140401 (2002).
- [40] H. Y. Hwang, S-W. Cheong, P. G. Radaelli, M. Marezio, and B. Batlogg, *Phys. Rev. Lett.* **75**, 914 (1995).
- [41] T. Dhakal, J. Tosado, and A. Biswas, *Phys. Rev. B.* **75**, 092404 (2007).
- [42] T. Z. Ward, S. Liang, K. Fuchigami, L. F. Yin, E. Dagotto, E. W. Plummer, and J. Shen, *Phys. Rev. Lett.* **100**, 247204 (2008).
- [43] J. Wei, and D. Natelson, *Nanoscale* **3**, 3509 (2011).
- [44] P. Schiffer, A. P. Ramirez, W. Bao and S.-W. Cheong, *Phys. Rev. Lett.* **75**, 3336 (1995).
- [45] H. S. Alagoz, J. Jeon, S. T. Mahmud, M. M. Saber, B. Prasad, M. Egilmez, K. H. Chow, and J. Jung, *Appl. Phys. Lett.* **103**, 232402 (2013).
- [46] M. H. Phan, M. B. Morales, N. S. Bingham, H. Srikanth, C. L. Zhang, and S. W. Cheong, *Phys. Rev. B* **81**, 094413 (2010).
- [47] H. S. Alagoz, J. Jeon, R. Boos, R. H. Ahangharnejhad, K. H. Chow, and J. Jung, *Appl. Phys. Lett.* **105**, 162409 (2014).
- [48] H. Guo, J. H. Noh, S. Dong, P. D. Rack, Z. Gai, X. Xu, E. Dagotto, J. Shen, and T. Z. Ward, *Nano lett.* **13**, 3749 (2013).
- [49] T. Nakajima, T. Tsuchiya, Y. Ueda, and T. Manabe, *J. Phys. Soc. Jpn.* **79**, 014712 (2010).
- [50] M. Quintero, F. Parisi, G. Leyva, and L. Ghivelder, *J. Phys.:Condens. Matter* **20**, 345204 (2008).
- [51] L. Ghivelder and F. Parisi, *Phys. Rev. B* **71**, 184425 (2005).
- [52] P. A. Sharma, S. B. Kim, T. Y. Koo, G. Guha, and S-W. Cheong, *Phys. Rev. B* **71**, 224416 (2005).
- [53] S. R. Bakaul, B. F. Miao, W. Lin, W. Hu, A. David. H. F. Ding, and T. Wu, *Appl. Phys. Lett.* **101**, 012408 (2012).
- [54] V. Moshnyaga, A. Belenchuk, S. Hühn, C. Kalkert, M. Jungbauer, O. I. Lebedev, S. Merten, K.-Y. Choi, P. Lemmens, B. Damaschke, and K. Samwer, *Phys. Rev. B* **89**, 024420 (2014).

- [55] T. Z. Ward, X. J. Zhang, L. F. Yin, X. Q. Zhang, Ming Liu, P. C. Snijders, S. Jesse, E. W. Plummer, Z. H. Cheng, E. Dagotto, and J. Shen, *Phys. Rev. Lett.* **102**, 087291 (2009).
- [56] N. S. Bingham, P. Lampen, M. H. Phan, T. D. Hoang, H. D. Chinh, C. L. Zhang, S. W. Cheong, and H. Srikanth, *Phys. Rev. B* **86**, 064420 (2012).
- [57] N. A. Babushkina, L. M. Belova, D. I. Khomskii, K. I. Kugel, O. Yu. Gorbenko, and A. R. Kaul, *Phys. Rev. B* **59**, 6994 (1999).
- [58] H. J. Lee, K. H. Kim, M. W. Kim, and T. W. Noh, B. G. Kim, T. Y. Koo, S.-W. Cheong, Y. J. Wang, and X. Wei, *Phys. Rev. B* **65**, 115118 (2002).
- [59] M. C. Dekker, A. D. Rata, K. Boldyreva, S. Oswald, L. Schultz, and K. Dörr, *Phys. Rev. B*, **80**, 144402 (2009).
- [60] Y. Q. Zhang, H. Meng, X. W. Wang, J. J. Liu, J. Du, and Z. D. Zhang, *Appl. Phys. Lett.* **99**, 252502 (2011).
- [61] C. H. Tsang, R. E. Fontana, T. Lin, D. E. Heim, B. A. Gurney, and M. L. Williams, *IBM J. RES. DEVELOP.* **42**, 103 (1998).
- [62] H. Neal Bertram, *IEEE Trans. Magn.* **31**, 257 (1995).
- [63] M. Egilmez, R. Ma, K. H. Chow, and J. Jung, *J. Appl. Phys.* **105**, 07D706 (2009).
- [64] T. R. McGuire, R. I. Potter, *IEEE Trans. Mag.* **MAG-11**, 1018 (1975).
- [65] J. Chen, W. Wei, K. Zhang, K. Du, Y. Zhu, H. Liu, L. Yin, and J. Shen, *Appl. Phys. Lett.* **104**, 242405 (2014).
- [66] M. Ziese, *Phys. Rev. B.* **62**, 1044 (2000).
- [67] R. Li, H. Wang, X. Wang, X. Z. Yu, Y. Matsui, Z. Cheng, B. Shen, E. W. Plummer, and J. Zhang, *PNAS* **106**, 14224 (2009).
- [68] M. Egilmez, M. Abdelhadi, Z. Salman, K. H. Chow, and J. Jung, *Appl. Phys. Lett.* **95**, 112505 (2009).
- [69] W. Ning, Z. Qu, Y. Zou, L. Ling, L. Zhang, C. Xi, H. Du, R. Li, and Y. Zhang, *Appl. Phys. Lett.* **98**, 212503 (2011).
- [70] J. D. Fuhr, M. Granada, L. B. Steren, and B. Alascio, *J. Phys.:Condens. Matter* **22**, 146001 (2010).
- [71] M. Bibes, V. Laukhin, S. Valencia, B. Martínez, J. Fontcuberta, O. Yu Gorbenko, A. R. Kaul, and J. L. Martínez, *J. Phys.:Condens. Matter* **17**, 2733 (2005).

- [72] H. Li, L. Li, H. Liang, L. Cheng, X. Zhai, and C. Zeng, *Appl. Phys. Lett.* **104**, 082414 (2014).
- [73] J. O'Donnell, M. Onellion, and M. S. Rzchowski, *Phys. Rev. B.* **55**, 5873 (1997).
- [74] T. Z. Ward, J. D. Budai, Z. Gai, J. Z. Tischler, Y. Lifeng, and J. Shen, *Nat. Phys.* **5**, 885 (2009).
- [75] S. Singh, M. R. Fitzsimmons, H. Jeen, and A. Biswas *Appl. Phys. Lett.* **104**, 201602 (2014).
- [76] H. S. Alagoz, M. Khan, M. M. Saber, S. T. Mahmud, K. H. Chow, and J. Jung, *Appl. Phys. Lett.* **102**, 242406 (2013).
- [77] H. Unoki and T. Sakudo, *J. Phys. Soc. Jpn.* **23**, 546 (1967); M. Egilmez, M. M. Saber, I. Fan, K. H. Chow, and J. Jung, *Phys. Rev. B.* **78**, 172405 (2008).
- [78] D. Pesquera, V. Skumryev, F. Sánchez, G. Herranz, and J. Fontcuberta, *Phys. Rev. B.* **84**, 184412 (2011).
- [79] R. Loetzsch, I. Uschmann, and E. Förster, *Appl. Phys. A.* **106**, 563 (2012).
- [80] C. Yu, M. L. Scullin, M. Huijben, R. Ramesh, and A. Majumdar, *Appl. Phys. Lett.* **92**, 092118 (2008).
- [81] A. Kalabukhov, R. Gunnarsson, J. Börjesson, E. Olsson, T. Claeson, and D. Winkler, *Phys. Rev. B.* **75**, 121404(R) (2007).
- [82] N. Takubo, and K. Miyano, *Phys. Rev. B* **76**, 184445 (2007).
- [83] A. K. Debnath, and J. G. Lin, *Phys. Rev. B* **67**, 064412 (2003).
- [84] J. Gao, S. Q. Shen, T. K. Li, and J. R. Sun, *Appl. Phys. Lett.* **82**, 4732 (2003).
- [85] A. Asamitsu, Y. Tomioka, H. Kuwahara, and Y. Tokura, *Nature* **388**, 50 (1997).
- [86] W. Wei, Y. Zhu, Y. Bai, H. Liu, K. Du, K. Zhang, Y. Kou, J. Shao, W. Wang, D. Hou, S. Dong, L. Yin, and J. Shen, *Phys. Rev. B* **93**, 035111 (2016).
- [87] J. Gao, and F. X. Hu, *Appl. Phys. Lett.* **86**, 092504 (2005).
- [88] F. X. Hu, and J. Gao, *Phys. Rev. B* **69**, 212413 (2004).
- [89] B. Dieny, *J. Magn. Magn. Mater.* **136**, 335 (1994).
- [90] B. Dieny, V. S. Speriosu, S. S. P. Parkin, B. A. Gurney, d. R. Wilhoit, and D. Mauri, *Phys. Rev. B.* **43**, 1297 (1991).
- [91] M. Egilmez, R. Ma, K. H. Chow, and J. Jung, *J. Appl. Phys.* **105**, 07D706 (2009).

- [92] J. S. Moodera, J. Nassar, and G. Mathon, *Annu. Rev. Mater. Sci.* **29**, 381 (1999).
- [93] J. B. Philipp, C. Hfener, S. Thienhaus, J. Klein, L. Alff, and R. Gross, *Phys. Rev. B.* **62**, R9248 (2000).
- [94] J. H. Park, E. Vescovo, H. J. Kim, C. Kwon, R. Ramesh, and T. Venkatesan, *Nature (London)* **392**, 794 (1998)
- [95] Y. Lu, X. W. Li, G. Q. Gong Xiao, A. Gupta, P. Lecoeur, J. Z. Sun, Y. Y. Wang, and V. P. Dravid, *Phys. Rev. B.* **54**, 8357 (1996).
- [96] J. Z. Sun, W. J. Gallagher, P. R. Duncombe, L. Krusin-Elbaum, R. A. Altman, A. Gupta, Y. Lu, G. Q. Gong, and Gang Xiao, *Appl. Phys. Lett.* **69**, 3266 (1996)
- [97] N. D. Mathur, G. Burnell, S. P. Isaac, T. J. Jackson, B. S. Teo, J. L. MacManus-Driscoll, L. F. Cohen, J. E. Evetts, and M. G. Blamire, *Nature* **387**, 266 (1997).
- [98] K. Steenbeck, T. Eick, K. Kirsch, H. G. Schmidt, and E. Steinbei, *Appl. Phys. Lett.* **73**, 2506 (1998).
- [99] C. Kwon, Q. X. Jia, Y. Fan, M. F. Hundley, D. W. Reagor, J. Y. Coulter, and D. E. Peterson, *Appl. Phys. Lett.* **72**, 486 (1998).
- [100] Y. Ishii, H. Yamada, H. Sato, H. Akoh, Y. Ogawa, M. Kawasaki, and Y. Tokura, *Appl. Phys. Lett.* **89**, 042509 (2006).
- [101] Y. Ogimoto, M. Izumi, A. Sawa, T. Manako, H. Sato, H. Akoh, M. Kawasaki, and Y. Tokura, *Jpn. J. Appl. Phys.* **42**, L369 (2003).
- [102] G. Singh-Bhalla, S. Selcuk, T. Dhakal, A. Biswas, and A. F. Hebard, *Phys. Rev. Lett.* **102**, 077205 (2009).
- [103] H. S. Alagoz, J. Jeon, S. Keating, K. H. Chow, and J. Jung, *J. Appl. Phys.* **119**, 143905 (2016).
- [104] W. Prellier, P. Lecoeur, and B. Mercey, *J. Phys.:Condens. Matter* **13**, R915 (2001).
- [105] A. A. Bosak, O. Yu. Gorbenko, A. R. Kaul, I. E. Graboy, C. Dubourdieu, J. P. Senateur, H. W. Zandbergen, *J. Magn. Mater.* **211**, 61 (2000).